Impurity Transport Studies on MAST

A thesis submitted to the department of physics

of the University of Strathclyde

for the degree of Doctor of Philosophy

Stuart Henderson

July 2014

Supervisors:

Dr. M. G. O'Mullane
Department of Physics SUPA, University of Strathclyde, Glasgow

Prof. H. P. Summers
Department of Physics SUPA, University of Strathclyde, Glasgow

Dr. L. Garzotti
EURATOM/CCFE Fusion Association, Culham Science Centre, Abingdon

©

This thesis is the result of the authors original research. It has been composed by the author and has not been previously submitted for examination which has led to the award of a degree.

The copyright of this thesis belongs to the author under the terms of the United Kingdom Copyright Acts as qualified by University of Strathclyde Regulation 3.50. Due acknowledgement must always be made of the use of any material contained in, or derived from, this thesis.

Signature Date

Abstract

Impurity transport is a subject of fundamental importance in plasma physics in general and in tokamak physics in particular. The behaviour of the various impurity species and the evolution of their concentration determines, among other things, the fuel dilution and the fusion reaction rate, the plasma radiation pattern and the local energy balance, the plasma effective charge and resistivity and the neutral beam particle and power deposition profile. It is therefore important to develop both a sound experimental base and reliable models to interpret the experimental results and to predict the transport properties of impurities.

Time-dependent helium and methane gas puff experiments have been performed on the Mega Ampere Spherical Tokamak (MAST) during a two point plasma current, I_p, scan in L-mode and a confinement scan at constant I_p. For the I_p scan, a dimensionless safety factor, q, scan was attempted by using a constant toroidal magnetic field and by moderating the beam power to match the plasma temperature. The temperature and magnetic field was also kept constant during the confinement scan to probe the effects of the electron density gradient.

An evaluation of the He II ($n = 4 \rightarrow 3$) and C VI ($n = 8 \rightarrow 7$) spectral lines, induced by active charge exchange emission and measured using the RGB 2D camera on MAST, indicate that carbon experiences moderately higher rates of diffusion and inward convection than helium in the L-mode high I_p plasma. Lowering I_p in L-mode caused a moderate increase in the helium diffusion and convection coefficients near the plasma edge. Neoclassical simulations were carried out which indicate anomalous rates of helium and carbon diffusion and inward convection in the outer regions of both L-mode plasmas.

Similar rates of helium diffusion are found in the H-mode plasma, however these rates are consistent with neoclassical predictions. The anomalous inward pinch found for helium in the L-mode plasmas is also not apparent in H-mode. An outward flux of helium and carbon is found at mid-radius in H-mode, corresponding the region of positive electron density gradient.

Linear gyrokinetic simulations of one flux surface in L-mode using the GS2 and GKW codes were performed which show that equilibrium flow shear is sufficient to stabilise ion temperature gradient (ITG) modes, consistent with BES observations, and suggest that collisionless trapped electron modes (TEMs) may dominate the anomalous helium particle transport. A quasilinear estimate of the dimensionless

peaking factor associated with TEMs is in good agreement with experiment. Collisionless TEMs are more stable in H-mode because the electron density gradient is flatter. The steepness of this gradient is therefore pivotal in determining the inward neoclassical particle pinch and the particle flux associated with TEM turbulence.

Contents

List of Figures

List of Tables

Acknowledgements

There are many people I would like to thank, but first I will take this opportunity to thank both the EPSRC and UKAEA Culham for funding this Ph.D, and UKAEA Culham for allowing access to the facilities at CCFE.

I thank my supervisors Martin O'Mullane, Hugh Summers and Luca Garzotti for their patience, guidance and encouragement during my Ph.D. My understanding of ADAS (and coding in general) has been helped greatly by Martin. I am very grateful to Hugh for his vast knowledge of atomic physics and for the patience he has had with me during my undergraduate degree projects and Ph.D (especially whilst reading my thesis). I thank Luca for expanding my knowledge on impurity transport and tokamak theory in general and, most of all, for his advice and guidance from day one of my Ph.D. In addition, his help with planning my experiments on MAST and writing my first journal publication was greatly appreciated.

There are many people from the MAST team that I would like to thank. In particular, I thank Ash Patel for his countless hours of assistance in developing the codes used to analyse the raw RGB data and Martin Valovič for his advice on plasma transport and confinement theory. The neoclassical and gyrokinetic analysis in this thesis was the result of a great effort and collaboration with a number of people from CCFE. I would like to thank Colin Roach, David Dickinson and Francis Casson for their help with the gyrokinetic studies. Colin, for his help in improving my understanding of gyrokinetic analysis; David, for his patience and assistance in teaching me to use the GS2 code; and Francis, for helping me progress the work with GKW. My appreciation is also directed towards Sarah Newton for her time spent improving my understanding of neoclassical transport theory.

On a personal note, living in Oxfordshire has been enjoyable and made easy by all of my housemates, in particular Graeme Scott and Javier Fernández. Lads, it's been emotional. I would like to thank Chris Strain for the times he travelled down from Scotland to visit, making Didcot feel more like home. My friends in Oxfordshire and CCFE have made my time working here immensely enjoyable. Thank you Richard Lake, Matthew Leyland, Nick Walkden, Tan Williams and Hayleigh Barnett – it would not have been the same without all of you. I have also been lucky enough to work abroad with the Gas Discharge Physics Lab group at KAIST during my Ph.D and I would like to thank Joohwan Hong for helping me navigate through Daejeon and for introducing me to traditional Korean cuisine and beverages.

My deepest thanks go to all of the Elmore (and extended) family, all of my own family and to Sarah Elmore. All of their support during the latter stages of my Ph.D has been invaluable. Susan and David Elmore cooked many amazing dinners for me, perhaps one of the most enjoyable being the Lasagne made after arriving back from my week eating Korean food. It was a personal highlight seeing my nephew Lachlan in America during the APS conference and spending time with my niece Emily in Bristol. Thank you Mum for making sure I never forgot what the important things in life are and Dad for your continual support throughout my undergraduate and postgraduate years. Sarah, your love and unwavering support as each (self-imposed) completion date for my thesis came and went will never be forgotten. Also, I promise to shave more.

Stuart Henderson
July 2014

Chapter 1

Introduction

The international energy outlook report for the year 2013 predicts that the total world energy consumption in the year 2040 is expected to increase by 56%, largely due to the increase in energy demand from developing nations. With over three quarters of the world's energy currently being supplied from a rapidly declining reserve of fossil fuels that produce harmful greenhouse gases, it is imperative new sources of energy with carbon free emission be developed and perfected to sustain this increasing world energy demand. Renewable electricity has advanced considerably, however wind, solar and wave power plants may suffer from intermittent generation due to their reliance on fluctuating environmental conditions, while the high cost and structural integrity of man-made water dams are a concern for hydro power plants. Nuclear fission currently contributes a significant amount to the world's energy needs, but faces serious political safety and radioactive waste concerns.

Thermonuclear fusion involves using extremely high temperatures to fuse together different hydrogen isotopes with consequential release of energy. This method of power generation can potentially offer a cleaner, inherently safe and almost limitless supply of nuclear energy. The highest Maxwell averaged fusion cross-section is between deuterium (D) and tritium (T) for temperatures < 1 MeV and is therefore the most commonly planned fuel species in thermonuclear fusion experiments [1]. The D-T reaction generates a 3.5 MeV alpha particle and a 14.1 MeV fast neutron as shown in equation 1.1.

$$ {}^{2}_{1}\mathrm{D} + {}^{3}_{1}\mathrm{T} \quad \rightarrow \quad {}^{4}_{2}\mathrm{He} + {}^{1}_{0}\mathrm{n} + 17.6 \text{ MeV} \tag{1.1} $$

The energy in the form of kinetic energy of the products must be captured. There is an almost limitless supply of deuterium available from the world's current reserves. However tritium is unstable but can be 'bred' by nuclear reaction of the neutrons with lithium. There have so far been very few experiments with D-T fuelling. Most experiments normally operate with D plasmas.

The alpha particles, being charged, can be contained in the reaction region. A fusion power plant is said to 'ignite' when the contained alpha particle energy is

sufficient to sustain the nuclear reactions. The sustainability criterion, or Lawson Criterion [1], for the D-T reaction can be expressed in terms of the fusion triple product as

$$nT\tau_E \geq 10^{21} \quad [\mathrm{m}^{-3}\mathrm{keV\ s}] \tag{1.2}$$

where n is the fuel density, T is the temperature and τ_E is the global energy confinement time. There are two main approaches to fulfilling Lawson's criterion. One method, called inertial confinement fusion (ICF), uses high powered lasers to compress and heat a relatively small, high density frozen fuel pellet for a short period of time until fusion occurs [2]. The other method, known as magnetic confinement fusion (MCF), uses a combination of magnetic fields to confine the fusion fuel in the form of a hot plasma for a sufficient period of time for fusion to occur [1].

MCF systems generally confine the plasma in a toroidal chamber and can operate with a number of different magnetic coil configurations. The most common configurations are the tokamak, described in the next section, and the stellarator, which achieves a steady state plasma using a complex helical coil configuration (see for example Geiger et al. [3]). Current tokamaks can achieve temperatures of the order of 10 keV and densities of the order of 10^{20} m^{-3} therefore, from equation 1.2, the main fuel ions must be confined for a time of the order of seconds.

1.1 Tokamaks

The tokamak system is currently regarded as the most promising route to a feasible fusion power plant and is the most developed of MCF systems. An illustration of the key components of a tokamak are shown in figure 1.1. The plasma is created within a vacuum chamber and confined away from the vessel walls in a torus shape using a combination of different magnetic fields. The words 'toroidal' and 'poloidal' mean the long and short way around the torus respectively, and the low field side (LFS) and high field side (HFS) correspond to the outer and inner parts of a poloidal section of the plasma respectively.

Plasma has a high capacity for cooperative action to escape from confining magnetic fields. In the tokamak design, toroidal field (TF) coils surrounding the vessel produce a toroidal magnetic field, B_T, that is inversely proportional to the major radius of the plasma, R. Two charge dependent vertical particle drifts are associated with the spatially varying field, called the grad-B and curvature drifts. The vertical electric field from these drifts produce a radial $\mathbf{E} \times \mathbf{B}$ drift directed towards the vessel walls. This $\mathbf{E} \times \mathbf{B}$ drift can potentially cause a rapid decrease in plasma confinement. To counteract the vertical charge separation, a central solenoid is wound around the centre column to induce a toroidal plasma current, I_p, and therefore a poloidal magnetic field, B_P. B_T and B_P add vectorially to give a helical magnetic field that connects the top and bottom of the plasma and which neutralises the charge separation in the plasma. External poloidal field (PF) coils

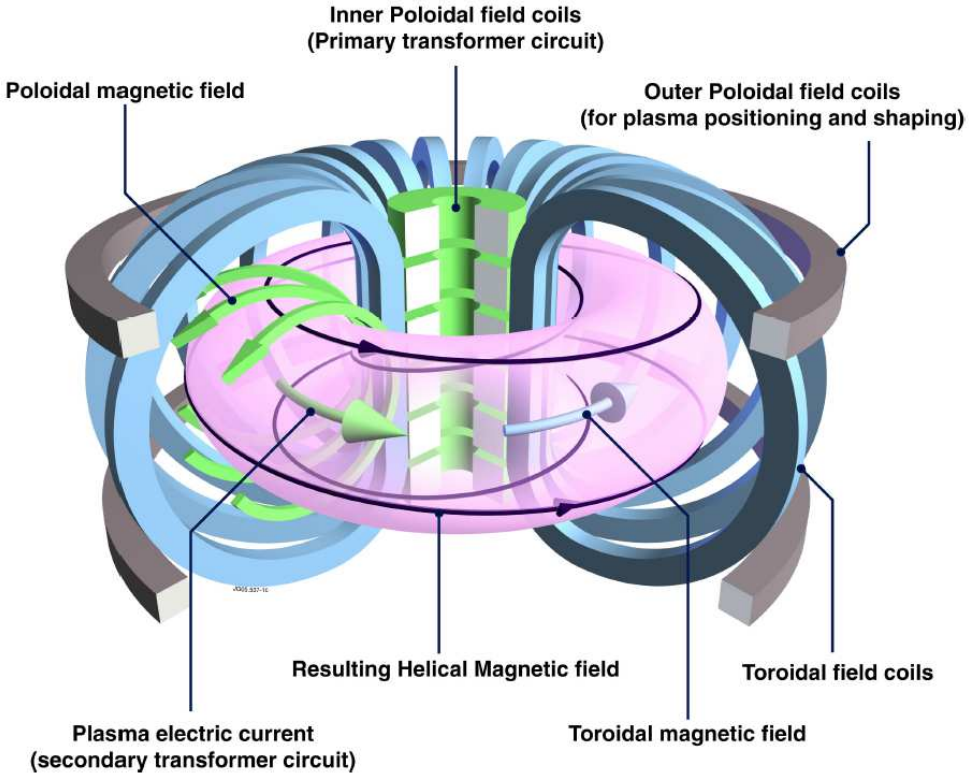

Figure 1.1: Schematic representation of a Tokamak, courtesy of the JET image database.

are also needed to stabilise the plasma in the vertical and horizontal directions and modify the shape of the plasma.

I_p also heats the plasma due to the plasma's finite resistivity, η. This form of heating is known as ohmic heating. As is well known, η decreases as the temperature increases and therefore limits the ohmic heating to temperatures of a few keV. Auxiliary heating methods are used to increase the plasma temperature up to the $10-100$ keV range required for thermonuclear burn. One of the most common forms of auxiliary heating methods, and of most relevance to this thesis, is produced using neutral beam injectors (NBI). Highly energetic ($60-100$ keV) neutral hydrogen atoms from the NBIs penetrate into the plasma core where they ionise and transfer energy to the plasma by collision processes. Neutral beams have an additional diagnostic capability. The charge transfer reaction from the neutral beam hydrogen atom to a plasma ion causes spectral line emission from the recombined ion. This latter point is discussed later in section 1.3.2.

The force balance between the magnetic field, plasma current and pressure gradients, can be defined to first order as

$$\mathbf{j} \times \mathbf{B} = \nabla p \tag{1.3}$$

where $\mathbf{j}$ is the current density and p is the pressure. Taking the scaler product

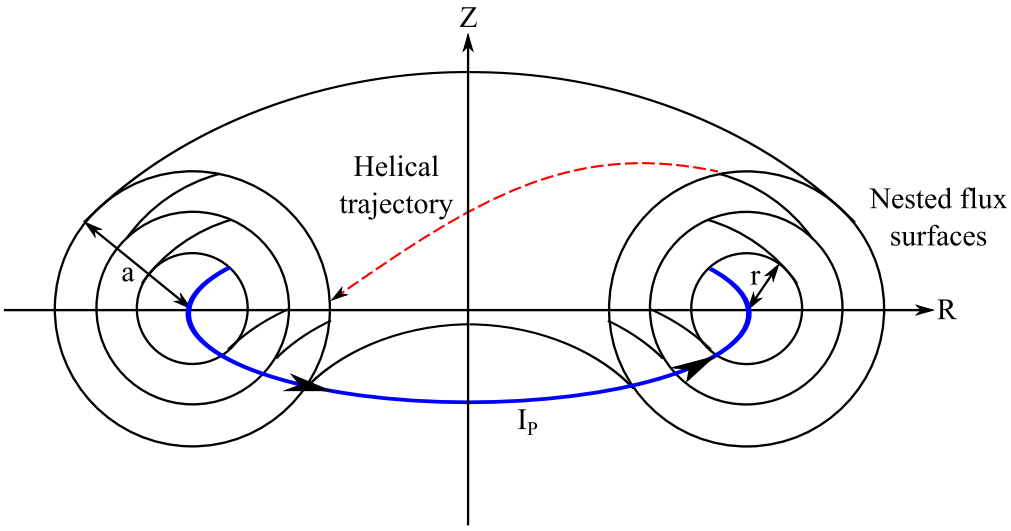

Figure 1.2: Major (R) and minor (a) radii, the toroidal plasma current (I_p) and the nested flux surfaces in a tokamak plasma.

of equation 1.3 with **j** and **B** proves that there is no current or magnetic field respectively in the direction of the pressure gradient (the radial direction). This creates a magnetic equilibrium consisting of an infinite set of toroidally symmetric nested flux surfaces each with constant magnetic field, current and pressure as shown in figure 1.2. Each flux surface can be characterised according to the magnetic winding number,

$$q = \frac{m}{n} = \frac{aB_T}{RB_P} \tag{1.4}$$

which denotes the ratio of toroidal revolutions (m) a closed field line makes to poloidal revolutions (n); a and R are the minor and major radii respectively (see figure 1.2). Rational surfaces with low q values (such as 1, 3/2 or 2) can lead to a plasma instability, therefore q is usually referred to as the safety factor. To avoid large scale plasma instabilities, q must be kept above unity everywhere, and above two near the plasma edge [1].

For the plasma to remain confined, the magnetic field pressure must exceed the plasma pressure. The ratio of these two pressures is called beta, β, and is quoted (usually as a percentage) using the expression [4]

$$\beta = \frac{2\mu_0 < nkT >}{B_T^2} \tag{1.5}$$

where $p =< nkT >$, k is the Boltzmann constant and μ_0 is the permittivity of free space. Ideally, tokamaks should operate at high β because the fusion reaction rate varies directly with p. One can also consider β to be inversely proportional to cost because the main running expenditure of a fusion reactor arises from the magnetic field generation. However the maximum beta is limited by magnetohydrodynamic (MHD) instabilities such as the 'kink' mode, which occurs when the plasma is carrying excess I_p [1]. The kink mode describes the situation where a toroidal flux

surface deviates from its circular trajectory and folds in on itself causing a rapid loss of confinement. A definition of the β limit will be given in section 1.2.

The global energy confinement time of the plasma is defined as [1]

$$\tau_E = \frac{\int \frac{3}{2} n(T_i + T_e) d^3x}{P} \tag{1.6}$$

where P is the total power input and T_e and T_i are the electron and ion temperature. Unfortunately, a frequently observed feature of tokamaks is that τ_E is shorter than predicted values based solely on Coulomb collisions in a toroidal geometry (neo-classical theory). The confinement behaviour is put into four categories: Ohmically heated plasmas and additionally heated plasmas in L (for low), H (for high) and VH (for very high) confinement modes [1]. In low density ohmic plasmas, τ_E increases linearly with density up to some critical value. Beyond this critical value τ_E remains constant with density. L-mode is characterised by a decrease in τ_E with increasing auxiliary heating and features low temperatures and temperature gradients near the plasma edge. H-mode plasmas are characterised by an improved confinement time in the plasma edge and a doubling of the overall confinement time compared to L-mode. The density profile in H-mode plasmas features a flat region in the core and a very steep region in the plasma edge called the density pedestal. VH-mode plasmas cover a variety of plasmas which produce an enhanced confinement in the plasma core with respect to the H-mode plasmas.

The two tokamak configurations of interest for this thesis are the conventional tokamak (CT) and the spherical tokamak (ST). The CT and the ST differ in aspect ratio, $A \equiv R/a$, as shown in figure 1.3. CTs operate with a value of $A > 2.5$ and are the most common tokamak design whereas STs are more compact and allow for a value of $A \sim 1$. ITER, a CT currently under construction in France, will be approximately twice the size of the largest tokamak to date (the JET machine in the UK) and aims to demonstrate the physics and engineering technology of a tokamak on the scale of a power station. Following ITER, it is hoped that a demonstration electricity-producing DEMO power plant will be constructed in the year 2030 [5]. Before DEMO, other aspects of a fusion reactor remain to be developed, such as vessel wall and blanket components which convert the neutron power to electrical power. These tests should be carried out in an affordable Component Test Facility (CTF), that can deliver reactor-level neutral and heat fluxes, albeit without producing net fusion power. A prime candidate for a CTF in current planning is the ST due their compact size and affordability [5].

1.2 Spherical Tokamaks

The first concept of an ST was put forward in 1986 by Peng and Strickler [6] to extend the concept of a CT into the limit of minimal A. One of the main motivations for reducing A was to increase the β limit of the plasma. Work by Sykes et al. [7]

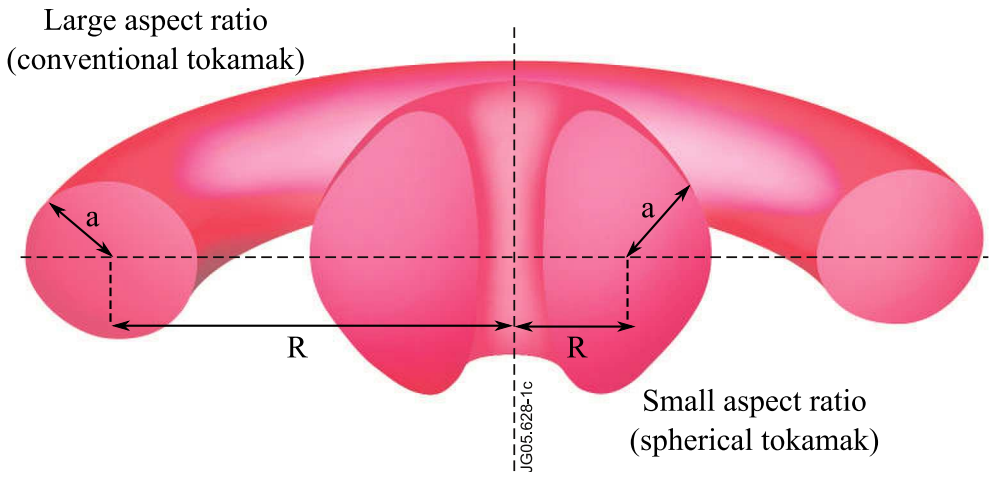

Figure 1.3: A conventional tokamak of high aspect ratio compared to a spherical tokamak of low aspect ratio, courtesy of the JET image database.

and Troyon et al. [8] showed that the β limit can be written as $\beta_T \leq \beta_N I_N$ where β_T is the toroidal β, $\beta_N = 3.5$ is the Troyon coefficient (assuming β_T is a percentage) and I_N is the normalised current $I_N = I_p/aB_T$. I_N is also inversely proportional to A and the safety factor at 95 % of the plasma minor radius, q_{95}, therefore STs are potentially more efficient than CTs because their smaller A value allows for a higher β limit.

Another advantage of STs is that the plasma is inherently more stable than CT plasmas. The natural ST plasma shape, that is of high elongation and triangularity, helps the plasma to remain stable against the magnetohydrodynamic (MHD) modes and thus achieve a larger β limit. Elongation of the plasma occurs naturally at low A as a consequence of force balance between the internal plasma currents flowing in opposite directions on either side of the centre column which interact more strongly at low A [9]. The interaction between the two opposite currents creates a vertical force which competes with the natural circular flux surfaces induced by the magnetic field from the centre column. With high vertical elongation of the plasma, the poloidal circumference increases meaning that the particles take longer to complete a poloidal revolution which in turn increases q_{95}. As the interaction between the currents on each side of the centre column decreases outwards, the elongation also reduces outwards leading to a triangular, D-shaped plasma. The outward-pointed triangularity of the plasma also acts to increase q_{95}.

STs experience a large variation of B_T across the plasma radius compared to CTs meaning that the ratio of B_T and B_P on the HFS is greater than the LFS, resulting in a longer confinement of the particles on the HFS compared to the LFS as shown in figure 1.4. The region of plasma on the HFS, called the good curvature region, experiences increased stability since the centrifugal force acts against the pressure gradient to stabilise it. Conversely, the region of plasma on the LFS, called the bad curvature region, experiences an outward force due to both the centrifugal

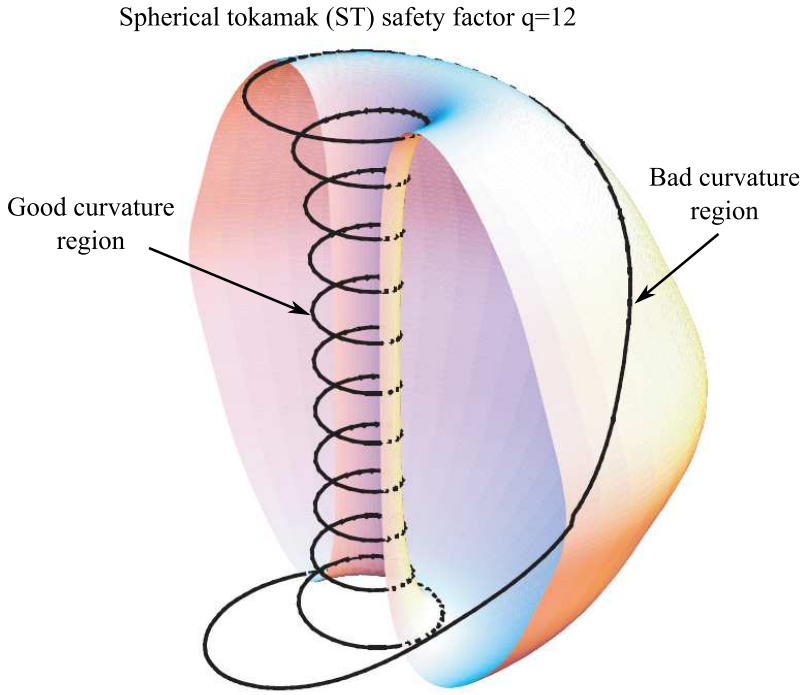

Figure 1.4: Schematic representation of a single field line for a spherical tokamak with safety factor $q = 12$.

force and the pressure gradient. The increased time the particles spend in the good curvature region was found to improve the stability of certain MHD modes [10]. A strong stabilising factor of turbulent modes can also originate from the large $\mathbf{E} \times \mathbf{B}$ flow shear often found in neutral beam heated ST plasmas [11, 12], and from the strong β gradient generally achieved in ST plasmas due to the large central β [13].

The first ST designed in the UK, called START [14], achieved a record β_T value of ~ 40 % [15]. After the success of START, two larger scale STs were commissioned: the National Spherical Tokamak eXperiment (NSTX) [16, 17] based at Princeton Plasma Physics Laboratory USA, and the Mega Amp Spherical Tokamak (MAST) [18], based at Culham, UK. The MAST experimental programme makes use of a set of unusually high-resolution and wide-viewing diagnostics making MAST ideal for an impurity transport study. The experimental program on MAST has now finished and research has turned to the upgrade, MAST-U [19].

1.3 The Impact of Impurities

Any ion present in the plasma not contributing to the fusion burn is called an impurity. The impurities can be grouped into intrinsic and extrinsic categories, and subcategories of light and heavy, or low and high nuclear charge, z_0. Light impurities here are those with $z_0 < 10$. The intrinsic category includes impurities that have migrated into the plasma following erosion of the plasma facing components (PFCs) through sputtering and chemical erosion processes; also a DT plasma has

an intrinsic source of helium from thermalised alpha particles created in the plasma core. Extrinsic impurities are purposefully injected into the plasma either to study the subsequent impurity evolution or to alter the radiation pattern of the plasma. One can also make the distinction between recycling and non-recycling impurities depending on the capacity of the plasma wall to retain and/or re-release them. Recycling impurities include the naturally gaseous elements − the intrinsic helium or extrinsic neon or argon for example.

A substantial presence of impurities in the plasma results in fuel dilution[1], which can quench the burn process. More specifically, ignition requires $\rho = \tau^*_{He}/\tau_E \leq \rho_{crit}$, where τ^*_{He} is the effective thermalised helium confinement time. Simulations carried out by Reiter et al. [20] suggest that $\rho_{crit} \sim 15$ for a pure D-T plasma. Furthermore, as the concentration of other plasma impurities increase, the value of ρ_{crit} decreases and the ignition constraint in equation 1.2 increases [20].

Impurities also act to cool the plasma. Near the plasma edge, there is a significant temperature gradient where a mixture of neutral and partially ionised impurities exist. Typically low z_0 impurities are fully ionised in the hot plasma core, where as high z_0 impurities are usually partially ionised. Partially ionised impurities radiate energy through line and continuum emission, while the fully ionised impurities only radiate through continuum emission. Both a decrease in the core plasma temperature due to radiation losses and an increase in the average charge of the plasma cause an increase of plasma resistivity[2]. On the other hand, a controlled amount of impurities radiating energy in the plasma edge can help reduce the heat load on the PFCs and increase the stability of the plasma edge.

1.3.1 Impurity Sources

The thin layer of plasma between the vessel walls and the last closed flux surface (LCFS) of the plasma, called the scrape-off-layer (SOL), transports the plasma exhaust onto solid material target surfaces in both divertor or limiter configurations. These target materials must have high heat load capacity. The limiter configuration consists of a toroidally or poloidally symmetric ring of solid material which protrudes from the vessel wall and shields against any plasma interaction. In a divertor configuration, the plasma exhaust is directed onto toroidally symmetric tiles positioned either at the top or bottom (or both) of the vessel. Ideally, the only plasma contact is with the limiters or divertor targets, but in practice, this is not always achieved as unconfined neutral particles can strike all PFCs.

The divertor configuration, illustrated in figure 1.5, is widely accepted as the preferred exhaust solution for future tokamaks and will be used in ITER. The inventory of impurities in the plasma, other than atmospheric and alpha particles,

[1] Fuel dilution describes the ratio n_{DT}/n_e where n_{DT} is the deuterium/tritium density and n_e is the electron density.

[2] The plasma resistivity is not only an important parameter when evaluating the limit of ohmic heating, but also when considering the transport of particles due to collisions.

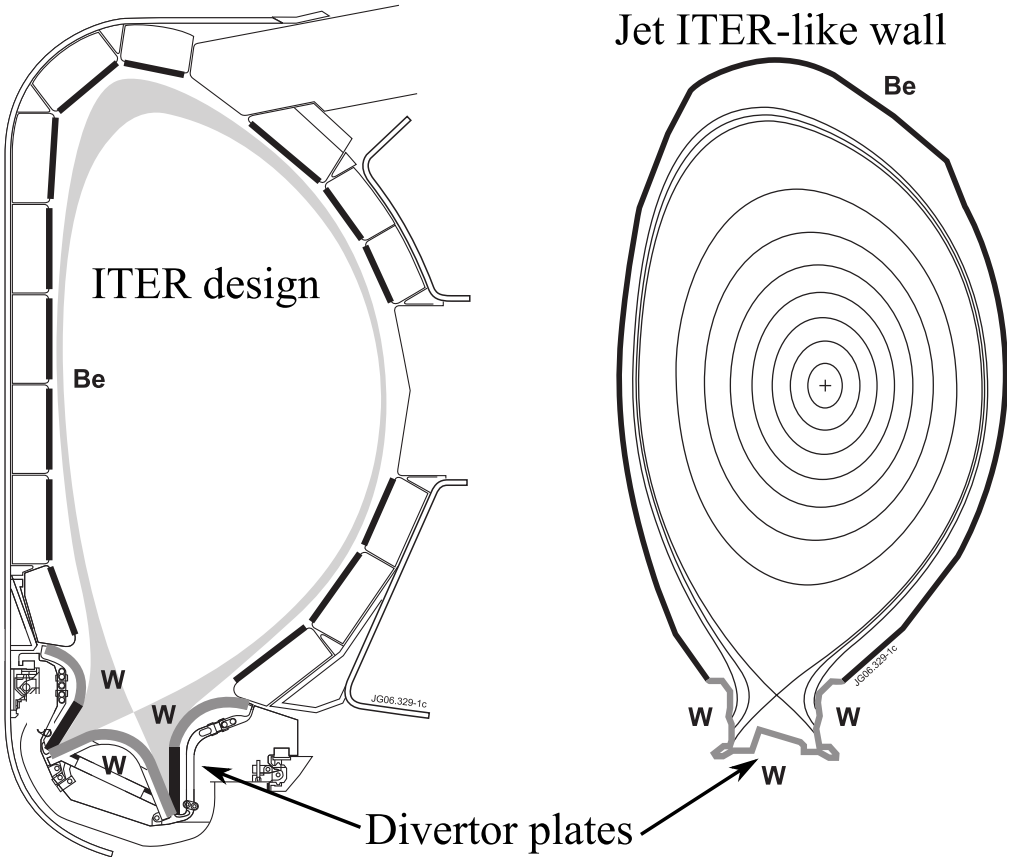

Figure 1.5: Schematic representation (not drawn to scale) of a poloidal cross section from the ITER wall design (left) and the ITER-like wall installed on JET (right), courtesy of the JET image database.

depend on the material choice of the PFCs. The most common material choice for the divertor plates in present tokamaks is carbon, in the form of graphite or carbon fibre composites (CFC). CFC tiles can withstand a much larger power loading than most other materials available, however they suffer from chemical erosion; this is a serious problem when tritiated hydrocarbons form leading to tritium fuel retention [21]. In ITER, the divertor tiles are likely to be made of tungsten to avoid the potential tritium retention found with CFCs, while beryllium will be used in the main chamber [22]. The ITER set up is illustrated in figure 1.5. JET currently has an ITER-like wall installed designed to test these wall materials. Its configuration is also illustrated in figure 1.5.

A number of measures are taken to minimise the impurity content in the vessel chamber. Vacuum pumping of the vessel removes the majority of free molecules in the vessel, but not the trapped molecules absorbed in the vessel surfaces. To aid the vacuum pump, the vessel can be baked at $\sim$200°C for around 200 hours to evaporate the loosely bound molecules from the vessel surfaces. A technique called gettering involves evaporating a thin layer of metal onto the wall that is chemically reactive (known as a getter), such as titanium, to trap particles such as oxygen and carbon. Boronisation is a similar procedure that deposits a thin film of boron

onto the wall surface to bind the high z_0 impurities already present on the wall. Boron is also an effective getter for oxygen. The effectiveness of these two processes quickly deteriorates and are therefore repeated every $50 - 100$ pulses. The other technique used to condition the vessel is glow discharge cleaning (GDC). Energetic ions (often He) bombard the vessel surfaces and remove loosely bound fuel and impurity particles which are then pumped from the machine. GDCs are performed between plasma pulses for a short period of time (< 10 minutes), and can also be performed following the vessel bake for ~ 30 minutes.

The ion effective charge, Z_{eff}, gives a local measure of the impurity concentration in the plasma, averaged over all impurities. The definition of Z_{eff} is given in equation 1.7, where the sum is over all ions of element i and charge state z with $n_{i,z}$ denoting the density.

$$Z_{eff} = \sum_{i,z} \frac{n_{i,z} z_i^2}{n_e} \tag{1.7}$$

For ITER, it is generally agreed that Z_{eff} must be ≤ 2. It is clear that a large inventory of low and high z_0 intrinsic impurities, such as helium, carbon, beryllium and tungsten, and also atmospheric particles such as oxygen and nitrogen, all contribute to the Z_{eff} in a tokamak plasma core and must therefore be carefully monitored. This thesis focuses on He^{2+} and C^{6+} density measurements.

1.3.2 Charge Exchange Spectroscopy

Spectroscopic measurements of impurity spectral line emission can be used to deduce the impurity ion density, from the total intensity of the line, and the impurity temperature and velocity, from the Doppler broadening and wavelength shift of the line; it is the former that is of interest here. NBI hydrogen atoms travelling along the beam path provide a local source of active charge exchange (ACX) emission from the fully ionised low z_0 impurities in the plasma core. The ACX process is summarised in equations 1.8 and 1.9, where A^z denotes the fully ionised impurity and $D_b^0(i)$ is hydrogen beam donor with a single electron in state i which is usually the ground state but can be in excited states, n is the principal quantum number and l is the angular momentum state of the recombined receiver ion.

$$A^z + D_b^0(i) \rightarrow A^{z-1}(nl) + D_b^+ \tag{1.8}$$

$$A^{z-1}(n'l') \rightarrow A^{z-1}(n''l'') + h\tilde{\nu} \tag{1.9}$$

Equation 1.9 represents the process which is the basis for charge exchange spectroscopy (CXS). The electron in the excited state of the receiver atom radiatively decays emitting a photon of energy $h\tilde{\nu}$ which is equal to the energy difference between the levels $n'l'$ and $n''l''$. There is also passive emission in the vicinity of the ACX spectrum induced by thermal charge exchange between thermal neutral hydrogen plasma atoms and He^{2+} and C^{6+} ions (often referred to as passive charge exchange

PCX) or collisional excitation of the hydrogen-like He^{+} and C^{5+} ions located in the colder plasma edge [23].

A filtered 2D camera system called RGB [24, 25] was available on MAST to measure two n-shell transitions, specifically the HeII ($n : 4-3$) and CVI ($n : 8-7$) at $\lambda = 468.5$ nm and $\lambda = 529.1$ nm. Most CXS diagnostics, using a 1D array of discreet viewing chords attached to a spectrometer, separate the passive and active components by measuring a toroidally symmetric region of plasma with no active emission. For a diagnostic such as RGB, the 2D pixel capability can be exploited by selecting pixel regions of the image immediately above and below the beam volume to measure the passive signal. The ACX component of the measured emissivity can be used to infer the He^{2+} and C^{6+} densities locally along the beam path using the expression

$$n_{i,z} = \frac{4\pi\epsilon_{i,z-1}^{(n\to n')}}{q_{eff}^{(n\to n')}\int_S n_b ds} \tag{1.10}$$

S is the intersection path length of the line-of-sight and the beam, n_b is the hydrogen beam density, $\epsilon_{i,z-1}^{(n\to n')}$ is the ACX line radiance for the transition $n - n'$ (in ph/s/m^2/sr) and $q_{eff}^{(n\to n')}$ is the effective CX emission coefficient. n_b is modelled using a code designed during this thesis and $q_{eff}^{(n\to n')}$ is interpolated from the Atomic Data and Analysis Structure (ADAS) [26]. The temporal and spatial evolution of the radial impurity ion distribution inferred from CXS directly reflects the impurity transport.

1.3.3 Impurity Transport

The ultimate goal of impurity transport theory is to understand, control and predict the impurity flux across a wide variety of tokamak plasma conditions. The standard ansatz describing the radial impurity flux (perpendicular to the magnetic surfaces) uses a summation of diffusive and convective parts given by

$$\Gamma_{i,z} = -D_i\frac{\partial n_{i,z}}{\partial r} + n_{i,z}v_i \tag{1.11}$$

where r is the minor radius and D_i and v_i are the diffusion and convection transport coefficients respectively. Following a transient event like an impurity gas puff (where $\Gamma_{i,z} \neq 0$), the transport coefficients may be determined using two techniques. The first technique reproduces the spatial and temporal evolution of $n_{i,z}$ using a radial transport code that solves the continuity equation,

$$\frac{\partial n_{i,z}}{\partial t} = -\frac{1}{r}\frac{\partial}{\partial r}(r\Gamma_{i,z}) + S_{i,z} \tag{1.12}$$

with a given set of boundary conditions. $S_{i,z}$ is the source and sink of particles controlled by atomic processes responsible for ionisation and recombination. The second technique fits a linear function to equation 1.11 at each point in space with

the gradient and offset of the fit representing D_i and v_i respectively.

A characteristic feature of CT plasmas is that the transport coefficients measured near the plasma edge are usually anomalously higher than those predicted for Coulomb collisions in a cylindrical plasma geometry (classical theory) or a toroidal plasma geometry (neoclassical theory). A large amount of work has gone into classical and neoclassical transport theory in the past and has been well documented [27]. The anomalous transport is caused by highly non-linear turbulence processes, with numerous turbulence drivers and suppression mechanisms. Although the theory for turbulence driven transport is not as complete as neoclassical, the understanding of the physical transport mechanisms has accelerated lately due to the advance in gyrokinetic computer modelling [28–31]. The extrapolation of previous transport studies on CTs (for example [32–34]) to STs is not straightforward, because the ST configuration is generally thought to achieve higher stability of the various plasma instabilities [10–13]. Data obtained from STs will not only improve the transport models but also broaden the international database on the aspect ratio by around a factor of two.

The analysis presented in this thesis focuses on evaluating the transport coefficients during a two point I_p scan and a plasma confinement mode scan, specifically L-mode and H-mode. The results generally indicate that the helium and carbon transport is neoclassical in H-mode and in the L-mode plasma core, whereas anomalous transport is the dominant mechanism in the outer radii of L-mode plasmas. Three codes are used to predict the transport: NCLASS [35] for neoclassical transport and the gyrokinetic codes GS2 [36, 37] and GKW [38] to give estimates for the level of anomalous transport. The analysis performed with these codes has allowed an explanation to be proposed of the differences between various plasma scenarios and to identify the main drives of neoclassical and anomalous transport.

1.4 Thesis Outline

The structure of this thesis is the following: Chapter 2 includes a review of the MAST vessel and diagnostics; specific focus will be given to the RGB diagnostic used to measure the CX emission, and the neutral beam system. The atomic physics models implemented in the ADAS codes, which are used to determine the effective CX emission coefficients, and the neutral beam stopping coefficient will be described in chapter 3. Chapter 4 provides all the experimental measurements, such as the CX emissivity measurements and the background plasma profiles, and describes the model used to determine the neutral beam and the impurity density. Transport coefficients are derived in chapter 5 and compared to results from other machines. These results are then discussed in light of the neoclassical and linear gyrokinetic simulations in chapter 6. Lastly, an overview and review of certain aspects of the work carried out for this thesis will be summarised in chapter 7.

Chapter 2

MAST and Diagnostics

2.1 Introduction

STs provide a new regime for the study of impurity transport processes in magnetised plasmas; one which must be understood to predict the performance of future devices. In CTs, impurity transport has been studied since the very early days of tokamak research. However, in STs this subject has been explored to a lesser extent because the ST is a configuration developed in more recent times with respect to the CT and also because other topics have been given higher priority so far. MAST and NSTX, two of the world's leading STs, provide an ideal opportunity to study the transport properties of impurities in high temperature, low aspect ratio and highly elongated plasmas. Experiments have been performed on NSTX aimed at the characterisation of the transport properties of neon, lithium and carbon in H-mode [39, 40] and neon in L-mode [41]. Some work has also been done in the past on MAST on the behaviour of tin [42] and carbon [43]. During the last two MAST experimental campaigns, further experiments have been performed to expand the experimental measurements of light impurity transport and to improve the quality of the measurement of the evolution of the impurity concentration. NSTX and MAST are two complementary machines with similar design specifications, and therefore the present transport analysis is compared with the transport studies performed on NSTX to seek consistent features of impurity transport. The present analysis is also compared with transport experiments performed on Alcator C-Mod [30] (hereafter called C-Mod) to analyse some of the differences between ST and CT impurity transport.

The 2D filtered camera system on MAST, called RGB [24, 25], views the full plasma cross section with VGA sensor resolutions and frame rates of up to 210 Hz. RGB has the capability to simultaneously measure two spectral lines in the visible induced by charge transfer between the injected hydrogen beam atoms and the fully ionised helium and carbon ions in the plasma. These measurements will be used in the present work to infer radial profiles of the He^{2+} and C^{6+} plasma concentration which will be used (in chapters 4 and 5) for the transport analysis.

Transport studies on MAST are supported by simulation codes which require, as input, a description of the bulk plasma parameters. MAST is equipped with a comprehensive set of diagnostics, in particular with respect to profile diagnostics for the electron temperature and density, the ion density and toroidal velocity, and the safety factor, measuring typically every 5 ms with about 1 cm spatial resolution.

This chapter focuses on details of the MAST vessel and the supplementary diagnostics required to constrain the transport models. An overview of the neutral beam design is also given to provide the necessary inputs to the hydrogen beam density model described later (in chapters 3 and 4). A summary of the intrinsic (helium and carbon) and injected impurity gas (helium and methane) influx into the plasma is presented to provide realistic boundary conditions for the impurity transport model detailed later (in chapter 5).

2.2 MAST

MAST is a stainless steel vacuum tank which is cylindrically shaped with a diameter of $d = 4.0$ m, and height of $h = 4.4$ m. A cross section of the MAST vacuum vessel is shown in figure 2.1. A vertical column, covered with an outer layer of armoured tiles, runs down the centre of the vessel. To allow for a low plasma aspect ratio, the diameter of the centre column is limited to $d = 0.4$ m. In the middle of the centre column, a solenoid is wound around a centre rod incorporating 24 water cooled copper conductors which generate the TF, as indicated by the P1 and T7 symbols respectively in figure 2.1. On the magnetic axis, the TF can vary between $B_T = 0.35 - 0.55$ T. The TF is highly anisotropic across the plasma diameter and ranges from 2 T on the HFS to 0.25 T on the LFS as $B_T \propto 1/R$. The solenoid is designed to produce a 1 V flux swing every $\sim$10 minutes lasting approximately a second; this sets an upper limit on the plasma pulse length, although in practice various MHD events will terminate the plasma before the solenoid flux runs out. To fuel the plasma, deuterium gas is puffed from the HFS, LFS, bottom and top of the vessel into the plasma edge. For a tokamak such as MAST, the gas generally penetrates deep enough into the plasma to fuel the core. The plasma density throughout the pulse is controlled either by using a feedback system, or by presetting the fuelling times prior to the plasma pulse.

The I_p induced by the central solenoid produces the primary PF. A total of 5 pairs of PF coils are positioned inside the vessel as shown by the P2 – P6 labels in figure 2.1. Each of these PF coils are encapsulated in a 3-mm thick stainless steel shroud, providing an intrinsic source of iron in the plasma. The P4 and P5 coil pairs provide a vertical field to guard against any abrupt radial displacements, while the P6 coil pairs generate a radial field to provide vertical position control. Typically on MAST, the initial plasma is produced without using the central solenoid by a novel technique called 'merging compression' which was first pioneered on START [14].

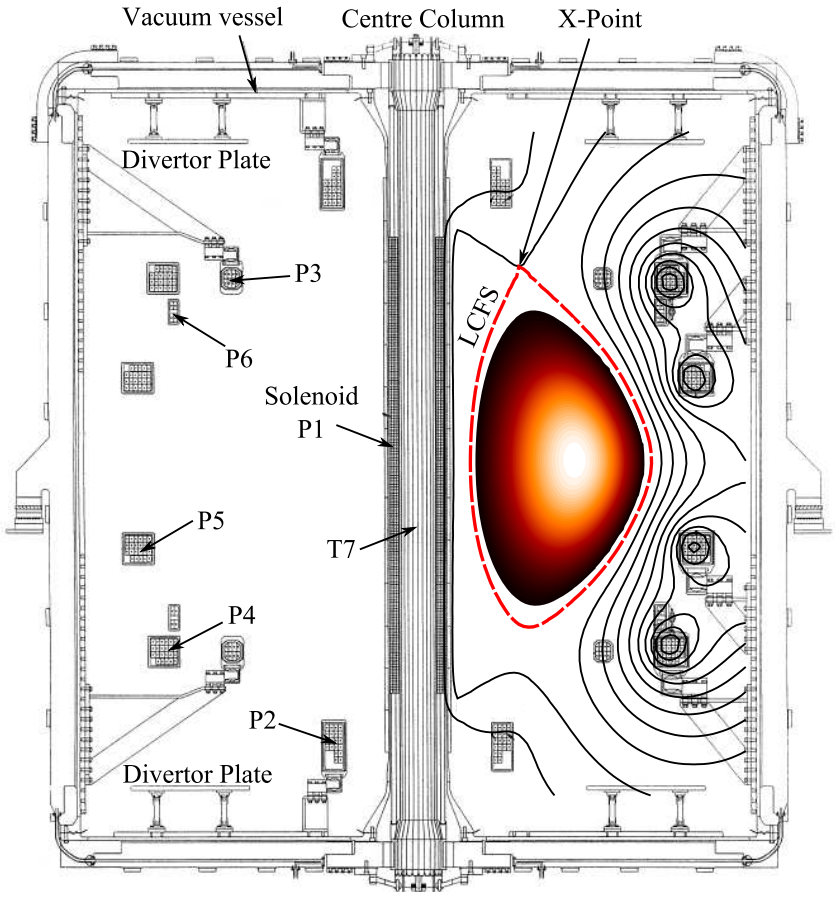

Figure 2.1: Cross-section of MAST vacuum vessel with the internal coils and components labelled on the left, and an example plasma equilibrium on the right.

In this case, the current in the P3 coils is ramped to the maximum value, and then rapidly reduced to zero to create the electric field. Two geometrically opposite plasma rings are created around the P3 coil pairs and then merged together near the vessel equator using the P4 and P5 coil pairs. This method of plasma generation can typically produce an I_p of up to 500 kA. The flux swing of the solenoid is then sufficient to ramp I_p up to 1.0 MA, but more typically to around $600 - 900$ kA. The volt-seconds remaining after the ramp up sustains a period of constant I_p, known as the current flat-top, for ~ 500 ms.

The lower and upper divertor coils, labelled P2 in figure 2.1, create a current in the same direction as I_p causing a null in the PF, called the 'X-point', which is illustrated on the RHS of figure 2.1. Generally the magnetic flux surface associated with the X-point is called the last closed flux surface (LCFS), shown by the red dashed line in figure 2.1. Outside the LCFS to the vessel wall, the field lines are open and transport the plasma exhaust ions down to the divertor plates. MAST can operate using either one X-point, called a single null divertor (SND) configuration, or with two X-points at the top and bottom of the vessel, called a double-null divertor (DND) configuration. The experiments in this thesis use a DND configuration during each plasma scenario.

A summary of achieved MAST parameters is given in the first column of table 2.1. The second and third columns show the achieved NSTX and C-Mod [44] parameters to aid comparison of the present analysis with previous transport experiments performed on each of these tokamaks. There is little difference in plasma shape and temperature between MAST and NSTX parameters. C-Mod is a conventional aspect ratio tokamak and operates with a higher magnetic field than MAST.

2.2.1 Neutral Beam Injection

MAST is initially heated from the ohmic heating induced by the resistance to the toroidal plasma current caused by electron-ion collisions. At low temperatures, ohmic heating is quite powerful but is less effective at high temperatures because the resistivity varies with the plasma temperature as $T_e^{-3/2}$. On MAST, the ohmic heating typically generates a power in the range $0.5-1.0$ MW and raises the plasma temperature to $\sim$0.5 keV. Auxiliary heating from neutral beam injectors (NBI) on MAST is provided by two (JET style) positive ion neutral injectors (PINI) [45, 46], named by their geographical position as the south (SS) and south-west (SW) beams (see figure 2.12). In total, the two PINIs can inject up to 3.8 MW of heating power into the plasma for ~ 5 s with typical accelerator voltages in the range of $U_b = 65-75$ kV. The energetic beam atoms, which are typically deuterium, penetrate into the plasma core where they ionise and thermalise with the plasma through collisions, raising the plasma temperature up to a few keVs.

The deuterium beam atoms also provide a local source of electron donation to the plasma ions along the beam path. Specifically, the work in this thesis models the density of He^{2+} and C^{6+} ions along the beam path using the spectral line emission

Table 2.1: Achieved Specifications of MAST, NSTX, and Alcator C-Mod

	MAST	NSTX	C-Mod
Plasma Current (MA)	1.45	1.50	2.02
Major Radius (m)	0.85	0.85	0.68
Minor Radius (m)	0.65	0.67	0.22
Aspect Ratio	1.31	1.27	3.91
Elongation	2.6	2.5	1.75
Triangularity	0.5	0.8	0.55
Core Toroidal Field (T)	0.52	0.45	8.11
Pulse Length (s)	0.7	0.55	5.0
NBI Power (MW)	3.8	5.0	–
Core Electron Temperature (keV)	2.5	2.5	2.5
Core Electron Density (10^{19} m^{-3})	5	10	60
Plasma Volume (m^3)	10.0	12.5	1.0

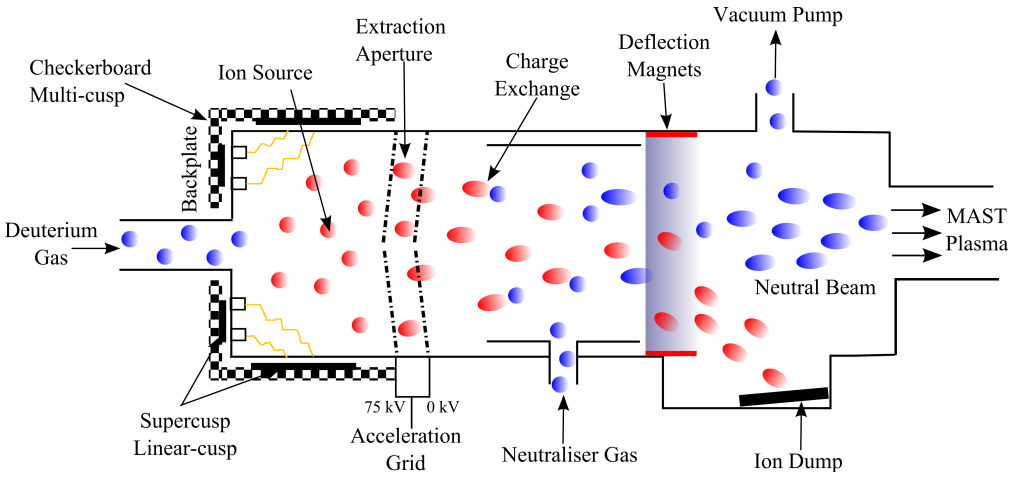

Figure 2.2: Cross section of a Positive Ion Neutral Injector (PINI) box. Blue circles represent neutral gas, red circles represent ions, and elongated circles represent energetic particles.

induced by charge exchange between the beam atoms and the impurity ions. The impurity density model requires a model of the hydrogen beam density. The beam density model requires inputs of the geometry of the PINI internal components, the divergence of the beam, the linear beam density per metre entering the plasma, the mixture ratio of the molecular and monatomic atoms and finally the energy of the beam. To understand and provide these inputs, the rest of this subsection gives a summary of the PINI design. Chapter 3 discusses the attenuation of the hydrogen beam atoms in plasma due to atomic ionisation processes and chapter 4 details the beam density model in full.

A schematic drawing of the PINI module is illustrated in figure 2.2. The three primary components of the PINI module are the ionisation source, the acceleration extraction aperture and the neutralisation chamber. The magnetic configuration of the ionisation source determines the mixture ratios of the molecular ions and, to an extent, the divergence of the beamlets, the extraction aperture focuses the beam and the efficiency of the neutralising chamber reduces the beam current entering the plasma.

Ionisation Source

Brown [47] and Godden [48] provide a thorough review of the ionisation source. The input gas is normally deuterium for MAST experiments, so the reaction chamber includes the atomic and molecular species D, D_2 and D_3, in their various permitted states, and their associated ions. These neutral species are promptly ionised by the cathode-anode system within the ionisation source chamber. Partial confinement of the ionised gas is achieved using a multicusp magnet configuration surrounding the

chamber, where magnets of opposite polarity are placed together in each row and column of the walls in a configuration called the checkerboard. Collisions involving the primary energetic electrons emitted from the heated filament cathode ionise the molecular atoms whilst the thermal secondary electrons dissociate the molecular ions. The D_2^+ and D_3^+ ions lose atoms in the neutralisation chamber becoming D^0 atoms with kinetic energies in proportions a half and third respectively to the initial accelerating voltage and therefore travel a smaller distance into the plasma before ionising than the D^0 atoms with kinetic energies $E_k = eU_b$.

To increase the monatomic ion yield, another configuration called the supercusp is often used which places two equal polarity linear cusp magnets over the central region of the backplate and along the base of the source walls, as shown in figure 2.2. A long-range magnetic field is created by the supercusp configuration which is strong enough to confine the primary electrons to the region close to the filament cathodes, but weak enough to allow the ions and thermal electrons to drift towards the extraction aperture resulting in a higher monatomic ion yield. One disadvantage of the supercusp configuration is that the long range filter field degrades the uniformity of the plasma. As a result, the beam inherits a higher divergence thus decreasing the overall power delivered to the plasma.

Up until the latest M9 experimental campaign on MAST, both the SS and SW PINIs used the supercusp configuration. Spectroscopic measurements from beam into gas experiments on MAST revealed a fractional injection rate of 88:9:3 (% $E_k : E_k/2 : E_k/3$) at beam energies of 60 keV and a divergence angle (defined as the $1/e$ width of the beam) of 0.5°. For the M9 experimental campaign, the SW PINI was converted to the checkerboard configuration with a measured fractional injection rate of 70:23:7 at 60 keV. The analysis in this thesis focuses on the CX emission induced by the supercusp SS PINI beam; although the neutral beam model can model the beam atoms from either PINI.

Extraction Aperture

The extraction aperture consists of 262 beamlet holes within a grid area of 45x18 cm^2. This grid is constructed in two halves tilted towards each other producing a vertical focus (VF) length of 14 m. Each beamlet hole is also tilted to the beamlet normal producing a horizontal focus (HF) length of 6 m. The location of the beamlet holes is shown in figure 2.3a. The axes are in beam coordinates (x_b, y_b, z_b). To convert to machine coordinates, the coordinates are rotated around z_b by an angle of 64.84° and 4.84° for the SW and SS PINIs respectively. The beam propagates along the equator of MAST (i.e $z_b = Z = 0$).

A voltage is then applied across the aperture to accelerate the ion beam. A typical trace of beam current, I_b, and voltage, U_b, for the SS and SW PINIs is shown in figure 2.3b. Beam voltage can be verified experimentally by the Doppler shift of the beam emission in the plasma and has been found to be accurate within

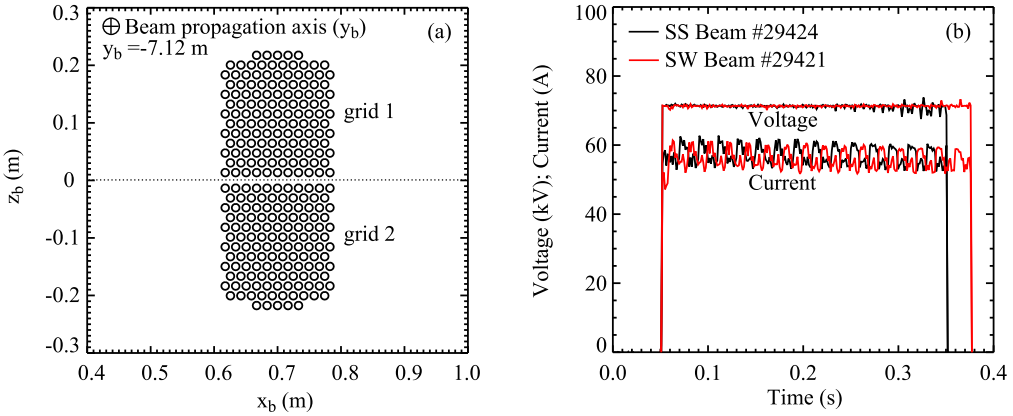

Figure 2.3: (a) The layout of the PINI extraction aperture beamlet holes. The x and z axes represent the plane perpendicular to the beam axis. (b) Time traces of the beam voltage and current for the SS and SW beams during two different MAST pulses.

± 3 kV. A scatter of 5 A is also visible in the current during beam operation. The linear beam density per metre entering the plasma, n_L^F, of each species fraction, F, is determined using,

$$n_L^{\mathrm{F}} = \frac{I_b^{\mathrm{F}} \epsilon_N}{v_b^{\mathrm{F}} e} \quad [\mathrm{m}^{-1}] \tag{2.1}$$

where e the electronic charge and v_b is the speed of each beam fraction defined as

$$v_b^{\mathrm{F}} = \sqrt{\frac{2eU_b}{m}} = 4.38 \cdot 10^5 \sqrt{E_b} \quad [\mathrm{ms}^{-1}] \tag{2.2}$$

where $E_b = eU_b/m$ is the energy of the beam per mass in keV/amu. ϵ_N is the neutralisation efficiency parameter, which is discussed next.

Neutralisation Chamber

The energetic ions then travel through a neutralisation chamber where a significant proportion will undergo CX reactions with a neutraliser gas. Calculating the efficiency of the neutralisation chamber relies on the knowledge of atomic rate coefficients and a knowledge of the internal heating in the chamber. While ϵ_N has been extensively studied in previous works [49–51], this thesis will use the widely accepted value on MAST of $\epsilon_N \sim 0.54$. An electromagnet is put in place to deflect the residual fast ions into a cooled ion dump that can withstand heavy ion bombardment. To ensure the purity of the neutral beam, thermal neutrals are removed using vacuum pumps.

The significant parameters listed above are summarised in table 2.2.

Table 2.2: PINI design specifications required for the beam model

	VF (m)	HF (m)	ϵ_N (%)	$E_k : E_k/2 : E_k/3$ (%)	Beamlets	1/e (°)
SS PINI	6	14	54	88:9:3	262	0.5

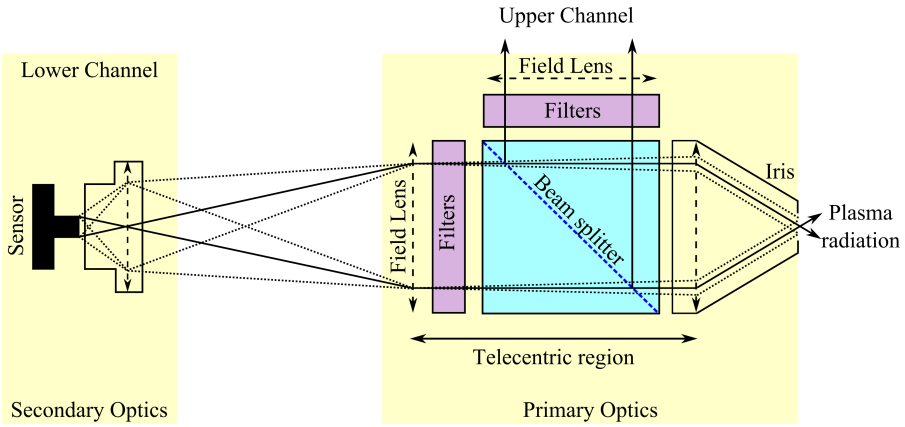

Figure 2.4: Schematic diagram of the RGB diagnostic showing the main optical components.

2.3 The RGB Diagnostic

Being able to image the plasma in the visible in two dimensions offers many advantages over typical single chord or a 1D array of discreet viewing chords attached to a spectrometer. For example, with a 2D system, reflections are easier to handle by avoiding the problem regions and an accurate spatial calibration of the diagnostic can be determined by comparing known objects in the field of view with a forward model based on the spatial calibration. An imaging diagnostic of this sort on MAST, called RGB [24, 25], views the full plasma cross section of MAST with VGA sensor resolution (640x480 pixel) and frame rates of up to 210 Hz, simultaneously measuring six pre-selected spectral band-passes in the visible through a single iris. The selected spectral regions are two Bremsstrahlung emissions, D_α beam and non-beam emission and the He II ($n = 4 \rightarrow 3$) and C VI ($n = 8 \rightarrow 7$) spectral line radiance. The latter two measurements are the primary measurements used for the transport analysis.

The optical layout of RGB is shown in figure 2.4. The design is based on a previous design by Patel et al [24,52]. The primary optics of the diagnostic includes a collection lens with a field stop, a beam splitter cube, two sets of stacked interference filters and two field lenses. In this part of the diagnostic, the plasma light is split into two channels by the beam splitter cube; for convenience these channels are called the upper and lower channels. The field stop, or iris, regulates the spectral throughput while the size of the optics determines the field of view (FOV). A FOV of 51° is specified, which is sufficient to measure the horizontal extent of the plasma (see figure 2.12). Furthermore, RGB has been installed $\sim$ 20 cm above the vessel equator to access radiation emanating from both the SS and SW beam volumes. The large focal length of the collection lens telecentrically images the plasma onto two primary image planes. Performing image operations in the telecentric region, where the chief rays are parallel to the optical axis, preserves the integrity of the image. The stacked filters, located in the telecentric region, consist of three unique interference filters combined with a set of tailored blocking filters. The interference filter stack

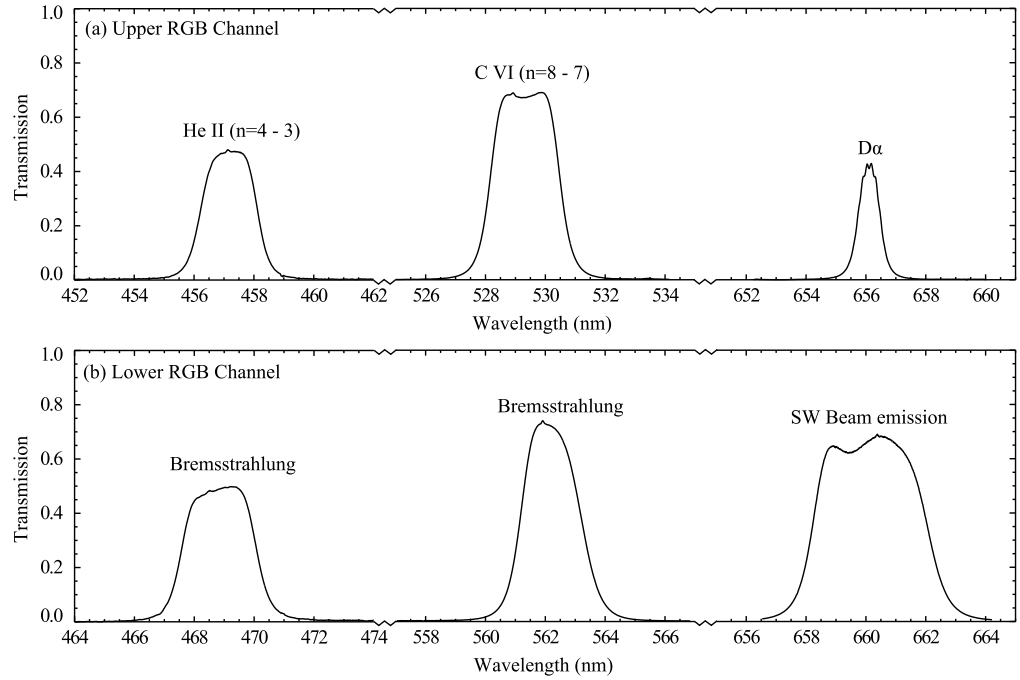

Figure 2.5: Measured stacked filter transmission fraction behaviour under a broad band source for the RGB upper (a) and lower (b) channels.

achieves the spectral fine-tuning of the system band-pass. The transmission of the upper and lower interference filter stack, measured following illumination from a broadband light source, is shown in figures 2.5a and 2.5b. A summary of the six pre-selected spectral band-passes are given in table 2.3.

The secondary optics section, shown for the lower channel in figure 2.4, includes a CCD camera system. The upper channel secondary optics are not shown in figure 2.4 as it is identical to the lower channel. The field lens in the primary optics converges the filtered light cone to within the aperture of the CCD camera and reduces the overall length of the diagnostic (to ~ 0.5 m). Both CCD cameras are equipped with a Bayer filter mosaic colour array as shown in figure 2.6a. The quantum efficiency of

Table 2.3: RGB spectral band-pass details and physics deliverables.

	Centre Wavelength (nm)	Effective Bandwidth (nm)	Emission
Upper			
Red	656.11	0.91	D_α
Green	529.51	2.56	C VI ($n = 8 \rightarrow 7$)
Blue	468.86	2.77	He II ($n = 4 \rightarrow 3$)
Lower			
Red	660.00	3.92	Beam Emission
Green	561.90	2.21	Bremsstrahlung
Blue	457.23	2.13	Bremsstrahlung

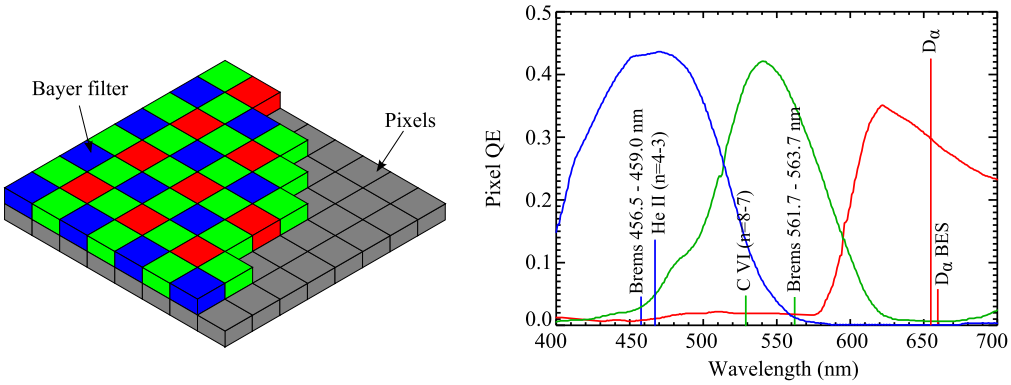

(a) (b)

Figure 2.6: (a) An illustration of the Bayor filter pixel array and (b) the quantum efficiency of each colour pixel.

each Bayor colour filter, as well as the monochrome response, is shown in figure 2.6b. The six pre-selected spectral band-passes are selected to broadly coincide with the high-end of the painted pixel. Grouping each of the separate colour matrix pixels together produces three different colour images for the upper and lower channels. The charges accumulated in both CCDs within the RGB diagnostic are digitised to a 12-bit resolution (12-bit DN/s).

A Bentham integrating sphere produces a broadband light source which uniformly fills the entire spectral band-pass filter, thus providing a spectral band-pass calibration. The spectral radiance of the integrating sphere is in units $W/m^2/nm/sr$ and is set by controlling the electric current of the halogen bulbs within the lamp. This calibration therefore produces a conversion factor from the measured 12-bit DN/s to $W/m^2/nm/sr$. To convert from Watts to photons per second, the output is divided by hc/λ_0, where λ_0 is the centre wavelength of the spectral line or the centre wavelength of the spectral band-pass for broadband emission (see table 2.3). The band-pass calibration was carried out before the undertaking of this thesis work and was therefore obtained from private communication. To infer the impurity density from the measurements, the output of RGB must be in units of $ph/s/m^2/sr$, therefore the nm^{-1} dependence from the band-pass calibration must be removed. This is done by multiplying the measurement by the effective band-width, $\Delta\lambda_f$, defined as

$$\Delta\lambda_f = \frac{1}{f(\lambda_0)} \int f(\lambda) d\lambda \tag{2.3}$$

where $f(\lambda)$ represents the filter functions shown in figure 2.5.

This expression in equation 2.3 accounts for any attenuation of a spectral line due to the filter response. This is an important point to note for the Doppler shifted beam emission measurement. Due to the change in viewing angle across the beam line, the beam emission emits at a range of wavelengths. For viewing angles that are close to perpendicular to the beam, the spectral line emits at wavelengths close to the edge of the spectral band-pass and are therefore attenuated corresponding to

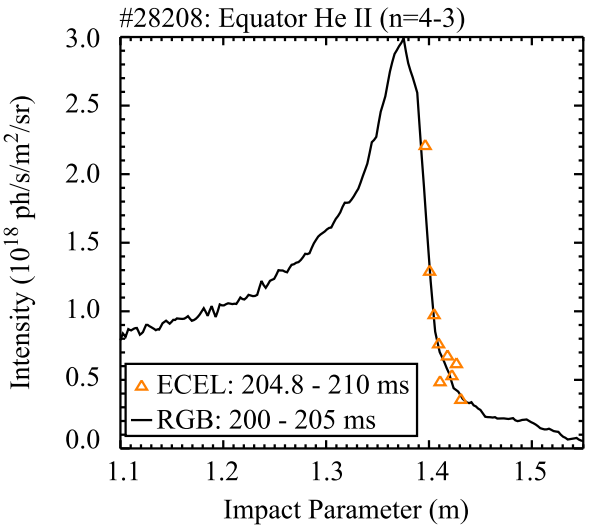

Figure 2.7: A cross diagnostic comparison of the He II ($n = 4 \rightarrow 3$) spectral line radiance measured by the RGB and ECELESTE [53] diagnostics.

the filter transmission curve. This is discussed in more detail in section 4.4.2, where the beam emission measured by RGB is compared to a model.

An example of the cross calibration results for the chord integrated He II ($n = 4 \rightarrow 3$) spectral line radiance measured by RGB and the edge Doppler spectroscopy diagnostic, called ECELESTE [53], is shown in figure 2.7. Good agreement is found between the two measurements in space and magnitude providing confidence in the spatial and absolute calibration of the diagnostic.

2.4 Impurity Sources

One of the methods used to model the impurity transport coefficients (see chapter 5) requires, as input, the source rate of neutral impurity atoms entering the LCFS. The impurity influx may arise from intrinsic or injected impurities. When the plasma comes into contact with plasma facing components (PFC), sputtering and chemical evaporation creates a source of impurities [54]. For sputtering, atoms are ejected from the PFCs if the elastic energy transfer from colliding ions exceeds the surface binding energy. The PFCs on MAST are mainly made of carbon fibre composites (CFC). For deuterium collisions, energies > 100 eV are sufficient to produce a high sputtering yield of carbon [55]. Carbon PFCs also can undergo chemical reactions with incident deuterium ions leading to the formation of volatile hydrocarbons which may be released from the PFC surface or sputtered at much lower threshold energies. Chemical erosion dominates at temperatures < 100 eV.

The divertor on MAST is of the open configuration [56] so the recycled particles from the divertor are free to migrate around the core plasma. MAST can allow for a larger volume of recycled gas to surround the plasma than most CTs due to the large plasma-wall separation. In particular for MAST, during the plasma current

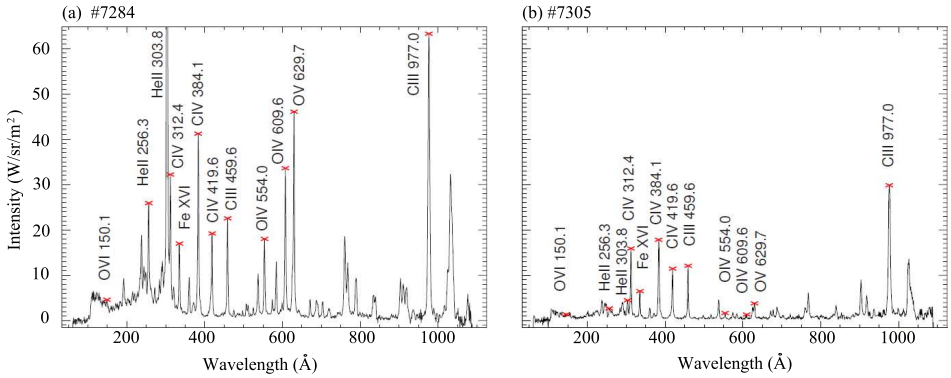

Figure 2.8: SPRED spectrum showing the most frequently observed impurity lines on MAST before (a) and after (b) boronisation. Image Credit: Lehane et al. [59]

ramp-up, there is also intense contact between the plasma and the centre column. However, it is difficult to estimate a sputtering and chemical erosion source rate as knowledge of the ion bombardment energy deposited on each PFC, as well as the surface temperature and lattice structure of the PFC, must be known. Furthermore, there is little control of the timing of the intrinsic source rate. The impurity source rate from a gas puff is easier to calibrate and can be triggered during periods of time when the plasma is quiescent. Previous experiments on other tokamaks, such as NSTX [39,41], DIII-D [57] and JET [58], have proven the suitability of a transport experiment based on an impurity gas puff source.

Boronisation is carried out approximately every 500 shots to control the intrinsic impurity concentrations. This is demonstrated by the two spectra shown in figures 2.8a and 2.8b, which were measured on MAST before and after boronisation using the SPRED (survey, poor resolution, extended domain) VUV spectrometer [60]. Before boronisation, a number of spectral lines are observed from oxygen, helium, carbon, and iron. After boronisation, the oxygen, helium and iron spectral lines are almost entirely reduced, while the carbon spectral line is less than the intensity measured before boronisation. Residual helium is present in MAST due to some of it remaining loosely bound to the vessel walls after each helium glow discharge cleaning, which is performed between each plasma pulse to provide a form of main density control. Unfortunately it was not possible to perform the experiments on MAST directly after boronisation due to machine restrictions. Typical helium and carbon concentrations measured during the present analysis were of the order of 1 % and 0.1 % (see figure 4.10).

2.4.1 Gas Influx

A sufficient amount of impurity gas must be injected to perturb the intrinsic impurity density. However injecting too large a quantity may alter the plasma properties. A piezo-electric valve located on the inboard side above the lower divertor is used in the present analysis to puff helium and methane (CH_4) gas into the vessel. The

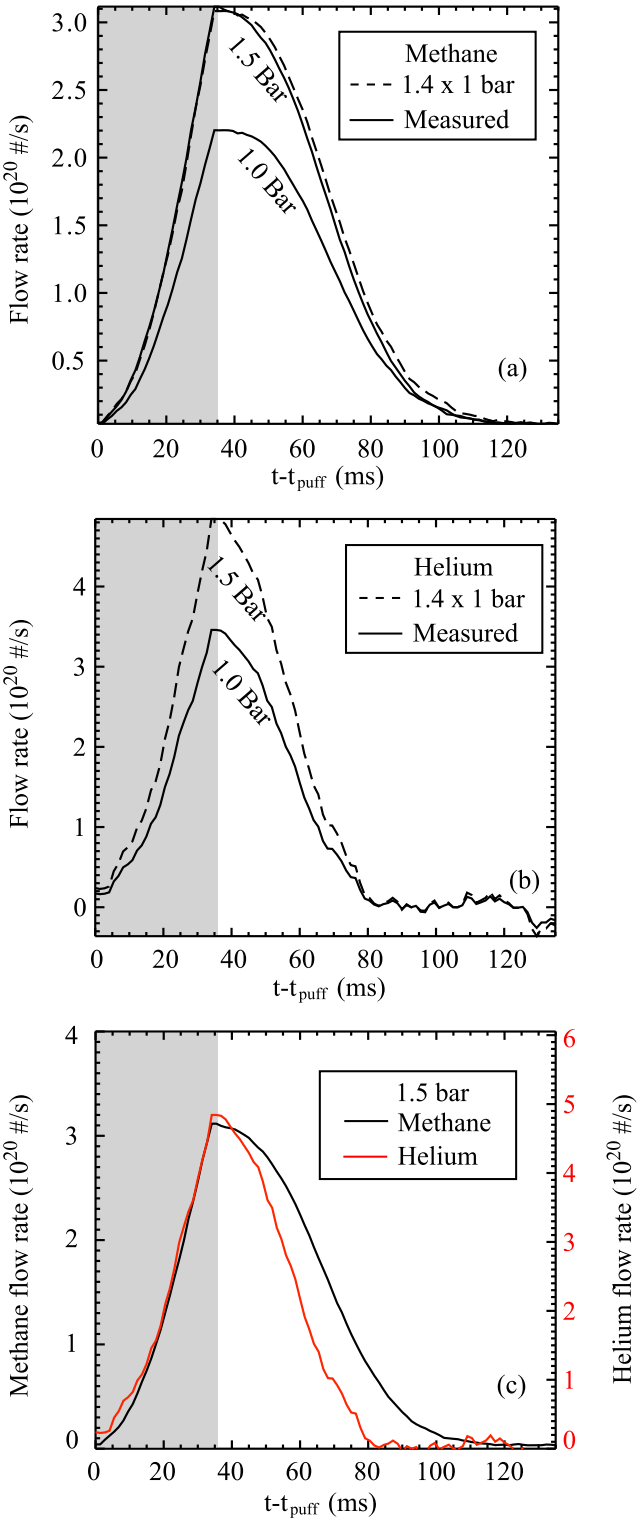

Figure 2.9: The gas flow rate (particles/s) of methane (a) and helium (b) at a plenum pressure of 1 and 1.5 bar respectively. The solid and dashed lines represent measurement and prediction respectively. (c) helium and methane gas flow rates at 1.5 bar compared together.

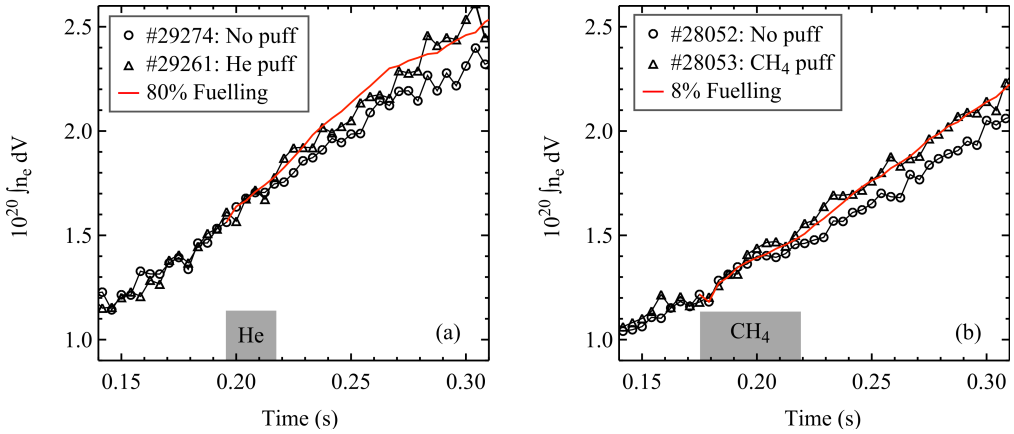

Figure 2.10: The plasma volume integrated electron density for a plasma with and without a helium (a) and methane (b) gas puff to illustrate the fuelling efficiency.

valve is connected to an impurity plenum held at a constant pressure of 1.5 bar, which is sufficient to puff trace amounts of impurity gas into the machine vessel on relatively short timescales. The flow rate of the impurity gas into the vessel after a voltage was applied to the piezo-electric valve was measured using the screened Bayard-Alpert ionization gauge. Direct pressure readings vary as $P \propto 1/R_g$ where R_g is the relative sensitivity factor, which is dependent on the gas. The standard gas used by industry for gauge calibration is nitrogen, that is $R_N = 1$. Relative sensitivity factors for methane and helium are quoted as 1.4 and 0.18 respectively. The full calibration of the pressure has been performed on MAST for deuterium gas, therefore the correction factor is calculated as $R_{CH_4,He}/R_{D_2}$ where $R_{D_2} = 0.35$.

During the calibration, the ionisation gauge returned the total number of particles (in D_2/m^3) as a function of time. Taking the derivative of these curves in time and multiplying by the vessel volume (~ 55 m^3) provides the flow rate of impurity atoms entering the vessel. Calibrations of the valve were carried out for helium at 1 bar, and methane at 1 bar and 1.5 bar. Flow rate profiles for methane and helium based on a 35 ms gas puff are shown in figure 2.9a and 2.9b respectively. It is seen from figure 2.9a that the 1.5 bar calibration of methane can be estimated by multiplying the 1 bar flow rate by a factor of ~ 1.4. Importantly, the temporal shape of the flow rate curve is the same at 1.5 bar compared to the 1.0 bar case. This multiplication factor is used to estimate the helium 1.5 bar flow rate. However the gas flow rate does not specifically describe the flow rate of neutral atoms into the plasma. The true flow rate is also dependent on the fuelling efficiency, which is discussed next.

2.4.2 Fuelling Efficiency

Cold, undirected neutral particles outside of the plasma do not easily penetrate into the plasma as they are ionised in the scrape off layer (SOL) and promptly directed towards the divertor. The fuelling efficiency, ϵ_F, is generally quantified by

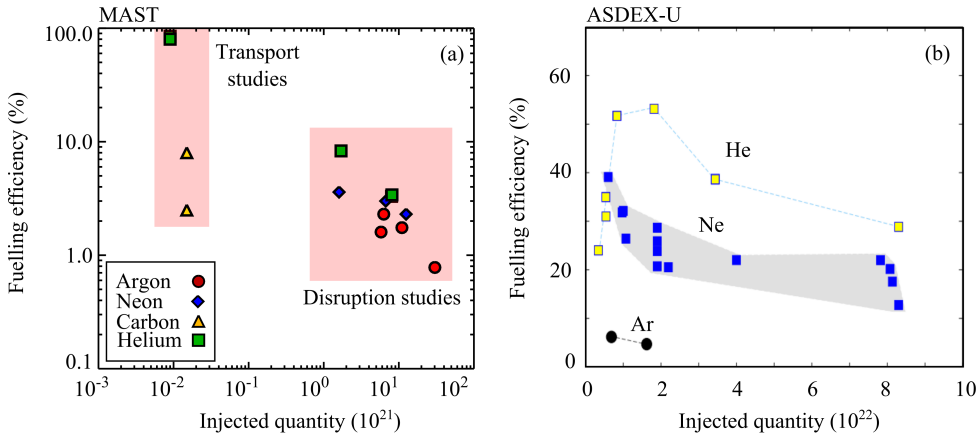

Figure 2.11: The fuelling rate of different impurities is shown as a function of the injected quantity. For the transport studies, two different points are shown for carbon and helium which represent results from the n_e and $n_{i,z}$ rise. Results from two previous studies from MAST [61] and ASDEX-U [62] have been used to produce the right hand side (disruption studies) of (a) and the full plot in (b).

comparing the measured rise in density with the expected rise in density from the gas flow rate calibration. One can either analyse the n_e rise measured by Thomson scattering (see next section), or the modelled $n_{i,z}$ rise inferred from charge exchange. Both techniques have been carried out in in the present analysis. This section will evaluate ϵ_F using the n_e measurements, whereas chapter 4 compares the rise of the impurity profile with the modelled rise from the gas injection.

It is noted here that the n_e rise is difficult to measure in this case, because the purpose of a tracer impurity injection is too minimise the n_e perturbation. Nevertheless an attempt at estimating ϵ_F is made as shown in figure 2.10a and 2.10b for helium and carbon respectively. The electron densities have been integrated over the plasma volume and the modelled injected electron concentrations are calculated from 2xHe and 10xCH_4 for a 24 ms helium puff and a 34 ms methane puff. For helium, a value of $\epsilon_F \sim 85\%$ produces the best match between the modelled and experimental n_e rise. The rise in n_e for the methane injection is larger than for the helium injection because there are 10 electrons associated with every methane molecule. A value of $\epsilon_F \sim 8\%$ has been determined for methane, however this does not distinguish whether the electrons have entered attached to hydrogen or carbon.

In an attempt to calibrate these results of ϵ_F against other work, figure 2.11 shows how these values of ϵ_F compare to two disruption studies that were carried out on MAST [61] and ASDEX-U [62]. Figure 2.11a shows the results from MAST, including both the results from this thesis (n_e and $n_{i,z}$ rise) and from the disruption studies [61], while figure 2.11b shows the results from the disruption studies on ASDEX-U [62]. One of the main conclusions from these graphs is that fuelling efficiency is dependent on the mass of the injected gas. Light impurities tend to produce higher fuelling efficiencies than heavier impurities. It was noted in the disruption study on MAST that this dependence could be due to the decrease

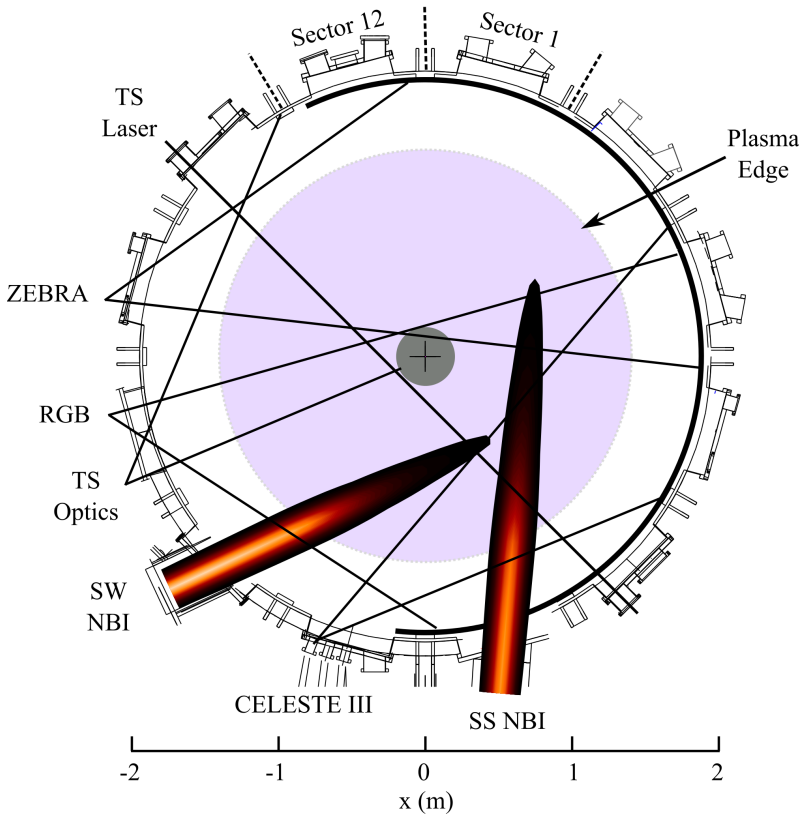

Figure 2.12: A schematic plan view of the MAST vessel showing the location and field of view of diagnostics used in the present analysis. Modelled SS and SW neutral beam density contours are shown for reference.

in propagation speed as mass increases, meaning that the particles take longer to reach the plasma edge [61]. There are two possible reasons why the helium fuelling efficiency is higher for the transport experiments compared to the disruption studies. Firstly, it is expected that as the fuelling rate increases, the gas fills the space between the vessel and plasma where there is minimal contact with the plasma instead of interacting with the plasma [61]. Secondly, it was unclear in the disruption studies whether the plasma was safely extinguished before the gas had a sufficient amount of time to reach the plasma edge.

These results are primarily useful to quantify the impurity source rate into the plasma. As a further result, it was also deduced that gas puffs of $\leq$ 30 ms were sufficient to perturb the impurity profile whilst maintaining a relatively unperturbed background plasma equilibrium.

2.5 Supplementary Diagnostics

The plasma volume in MAST is typically $\sim$ 10 m^3, while the vessel volume is $\sim$ 55 m^3. This large ratio of vessel-plasma volume allows for an exceptional level of diagnostic access compared to other tokamaks around the world. When studying the transport of impurities, it is essential to obtain the background plasma parameters

so as to constrain the transport models. These measurements include the electron temperature, T_e, the electron density, n_e, the ion temperature, T_i, the ion toroidal velocity, v_ϕ, the magnetic pitch angle, γ_p, the D_α radiation, the safety factor, q, the effective plasma charge, Z_{eff}, and the fluctuation frequency of the density to describe the background turbulence. An overview of the diagnostic layout on MAST is illustrated in the schematic of figure 2.12. A brief description of each diagnostic measurement used in the analysis of the impurity transport is now given.

Electron Temperature and Density

Measurements of T_e and n_e are carried out routinely on MAST by analysing the scattering of laser light from the electrons. From a classical view point, this can be described by considering an electromagnetic wave causing an electron to accelerate due to the electric field associated with the wave. The electron emits electromagnetic radiation in all directions as it is accelerated, which corresponds to the scattered wave. This classical description is valid provided that the photon energy is less than the electron energy. The diagnostics used to measure the photon scattering in tokamak plasmas tend to be limited to measurements of visible or longer wavelengths, where the laser light has much less energy than the electrons. In this regime, the scattering process is called Thomson Scattering (TS).

The velocity distribution of the electrons cause a Doppler broadening of the scattered light. If the electrons have a non-relativistic Maxwellian velocity distribution (i.e. Gaussian), then the full width half maximum (FWHM) of the scattered light is related to the electron temperature by (see equation 6.4.8 in Ref. [63])

$$\begin{aligned} \lambda_{FWHM} &= 4\lambda_0\sqrt{\frac{\ln 2kT_e}{m_e c^2}} \\ &= 1.45\cdot 10^{-1}\lambda_0\sqrt{T_e} \quad \text{[nm]} \end{aligned} \tag{2.4}$$

where λ_0 is the wavelength of the laser light in nm, T_e is in keV and the area of the scattered spectrum provides the electron density. For $T_e > 200$ eV, the relativistic effects mean that a Gaussian model centred on λ_0 is no longer valid. In this case the observed blue-shift and width can be modelled using the analytical Selden equation [64]. For $T_e \geq 5$ keV, higher order relativistic effects become significant and the analytical Naito equation must be used [65].

The common components of a TS system include one, or multiple, lasers and a collection lens which splits the scattered spectrum into wavelength channels using a spectrometer.The original Nd:YAG TS system on MAST [66] was upgraded in 2008 to provide 130 core spatial points at a sampling rate of 240 Hz using eight 30 Hz Nd:YAG lasers [67]. Radial profiles of T_e and n_e given in this thesis are from this new Nd:YAG TS system.

Ion Temperature and Velocity

Doppler broadening of spectral line emission from partially ionised impurities is used to determine T_i. The diagnostic on MAST, named CELESTE-III, is designed specifically to analyse the visible C VI ($n = 8 \rightarrow 7$) charge exchange emission (more details of charge exchange are given in chapter 3) with a typical sampling rate of 100 Hz [68]. A high throughput spectrometer is coupled to 64 active toroidal channels viewing the beam volume producing a spatial resolution of ~ 1 cm over the radial range of $0.8 - 1.4$ m. Passive emission due to the high thermal neutral density in the vessel is subtracted from the active signal induced by the neutral beam using 64 toroidal channels viewing a toroidally symmetric region of the plasma with no active charge exchange signal. CELESTE-III can also be used to measure the v_ϕ of the C^{5+} ions by measuring the Doppler shift of the emission. The properties of the carbon ions are assumed to be equal to those of the plasma ions because the energy transfer between the species occurs on a faster time scale than the energy confinement.

Effective Charge

The radiation produced by an electron that is accelerated in the electric field of a charged particle is called bremsstrahlung. Assuming the free electrons have a Maxwellian velocity distribution, the bremsstrahlung power per unit volume per meter from a single ion species is given by [69]

$$\frac{\Delta P}{\Delta \lambda} = \frac{64\pi}{3c^2}\left(\frac{e^2}{4\pi\epsilon_0}\right)^3\left(\frac{\pi}{6m_e^3}\right)^{1/2}\frac{n_e n_{i,z} z_i^2 < g^{III} >}{(kT_e)^{1/2}\lambda^2}\exp\left(-\frac{hc}{kT_e\lambda}\right) \tag{2.5}$$

where $< g^{III} >$ is the Maxwell averaged free-free Gaunt factor [70], $n_{i,z}$ is the density of ion i with charge z, m_e is the electron mass, λ is the wavelength of the radiation, c is the speed of light, ϵ_0 is the vacuum permittivity, k is the Boltzmann constant and e is the electronic charge. To calculate the continuum emission from all plasma impurities, it is necessary to sum equation 2.5 over all ion species giving

$$\epsilon_{br} = \frac{\Delta P}{\Delta \lambda} = \frac{1.89 \cdot 10^{-35} n_e \sum_{i,z} n_{i,z} z_i^2 < g^{III} >}{T_e^{1/2}\lambda^2}\exp\left(-\frac{1240}{T_e\lambda}\right)\ [\mathrm{W/m^3/nm}] \tag{2.6}$$

where n_e and $n_{i,z}$ are in m^{-3}, T_e is in eV and λ in nm. Recall (from equation 1.7) that the effective charge is defined as

$$Z_{eff} = \sum_{i,z}\frac{n_{i,z} z_i^2}{n_e} \tag{2.7}$$

where the sum is over all ions of element i and charge z in the plasma. From equations 2.6 and 2.7, an expression for Z_{eff} can be written as

$$Z_{eff} = \frac{\epsilon_{br} T_e^{1/2} \lambda^2}{1.89 \cdot 10^{-35} n_e^2 << g^{III} >> \exp(-1240/T_e\lambda)} \tag{2.8}$$

where $<< g^{III} >>$ is averaged over all ions.

When measuring the bremsstrahlung radiation, it is important to avoid measuring line radiation. A 2D camera on MAST, called ZEBRA [52], measures the line-integrated emissivity over the entire plasma cross-section using a filter centred on 521.3 nm with a spectral band-pass of $\sim$ 1 nm, which is thought to be free of any line radiation. Measuring in the visible spectral region is advantageous since there is a wide range of diagnostic instruments available. One disadvantage of this diagnostic is the fact that the bremsstrahlung spectral intensity falls off exponentially at wavelengths longer than those associated with the T_e ($\sim$ 1 nm). It is also unclear the extent to which molecular emission contributes to the signal near the plasma edge.

Density Fluctuations

Turbulent fluctuations are thought to induce a cross-field impurity flux greater than predictions based solely on collisions. A goal of turbulence simulations is often to determine the correlation length, or eddy size, of the dominant turbulent modes. The fluctuations are typically in the frequency range of the order of 10^6 Hz and can be observed in the D_α emission of the injected neutral beam atoms. On MAST, a 2D diagnostic, called the BES [71] diagnostic, was positioned to measure turbulent electron density fluctuations near the plasma edge with a radial and poloidal resolution of $\sim$ 2 cm [72]. These measurements are used to confirm the lack of ion scale turbulence found from gyrokinetic simulations in chapter 6.

Safety Factor and Plasma Shape

The theoretical models used in chapter 6, describing the stability of the plasma, require a profile of the safety factor and a parametrisation of the plasma shape. On MAST, the equilibrium reconstruction code called EFIT++ [73,74] solves the elliptic second-order, non-linear partial differential Grad-Shafranov equation describing the force balance in the plasma. It is given by

$$\Delta^* \psi = -\mu_0 R^2 \frac{dp}{d\psi} - \frac{dF^2}{d\psi} \tag{2.9}$$

where p is the pressure, ψ is the poloidal magnetic flux, $F(\psi) = RB_T$ is a function related to the total poloidal current, and $\Delta^* \psi = R^2 \nabla \cdot (R^{-2} \nabla \psi)$ denotes the elliptic operator. TS profiles are mapped to ψ and used as a pressure constraint. A

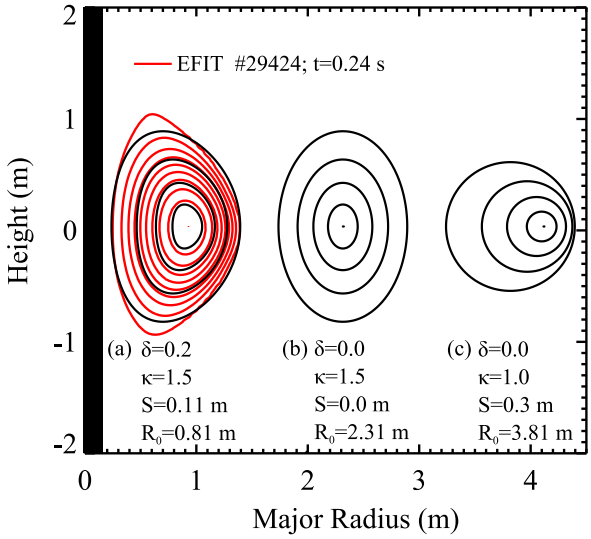

Figure 2.13: A poloidal cross-section of the magnetic flux geometry using the Miller equations (in black) and using the EFIT++ code (in red) for the #29424 discharge on MAST at $t = 0.24$ s. The Miller flux surfaces shown in (a) are chosen to best represent the EFIT++ magnetic reconstruction, while (b) and (c) demonstrate the effect of each Miller parameter.

constraint on the plasma current profile and the safety factor q is obtained from experimental measurements of the magnetic pitch angle, which is related to B_P, as

$$\gamma_P = \tan^{-1}\left(\frac{B_p}{B_T}\right) = \tan^{-1}\left(\frac{a}{Rq}\right) \tag{2.10}$$

The pitch angle is inferred from measurements of the motional Stark effect (MSE) diagnostic on MAST [75]. This works on the principle that the (Doppler shifted) D_α multiplet from neutral beams is split into degenerate Stark states. Each of these transitions are either polarised parallel or perpendicular to the electric field, denoted by π and σ components respectively. The orientation of the polarisation direction with maximum emission is measured which reveals the pitch angle of the magnetic field. The poloidal current in the field coils is measured using a solenoid that is wound around the field coil with both ends returning to the same point in space (Rogowski coils). The boundary conditions of ψ are constrained from experimental measurements of D_α emission from the plasma edge obtained from an optical linear camera, called LinCam [76], which measures the plasma D_α emission using a narrow spectral band-pass. An example of the flux surfaces obtained during a discharge on MAST using EFIT++ using the constraints given above is shown in figure 2.13.

The gyrokinetic codes use a simplified model of the poloidal cross sectional shape of the plasma, which can be defined following the equations used by Miller et al. [77] (known as Miller parameters). These equations are specified in 2.11 and 2.12 where θ is the poloidal angle, r is the minor radius, κ is the elongation, δ is the triangularity,

and S is the magnetic axis shift, known as the Shafranov shift [77].

$$R = R_0 + S + \frac{Sr^2}{a} + r\cos(\theta + \sin^{-1}\delta\sin\theta) \quad (2.11)$$

$$Z = Z_0 + \kappa r\sin\theta \quad (2.12)$$

Figures 2.13a–c demonstrates the effect of changing each Miller parameter. It should be noted that a cylindrical coordinate system can be reproduced with $\kappa = 1$, $\delta = 0.0$ and $S = 0$. Typical plasmas on MAST have Miller geometry values of $\kappa \leq 2.5$ and $\delta \leq 0.5$. An example of a magnetic equilibrium solved explicitly using EFIT++ is also shown in figure 2.13a to provide comparison with the Miller geometry.

2.6 Summary

MAST can produce plasma with a maximum plasma current flat-top of ~ 1.3 MA for ~ 0.5 s. Plasmas are typically elongated ($\kappa \leq 2.5$) and triangular ($\delta \leq 0.5$) with an aspect ratio of $R/a = 0.85/0.65 = 1.3$. Carbon and helium are intrinsic, the latter introduced from the helium glow discharge cleaning and the former from the plasma facing components. Two neutral beams on MAST, called by their geometrical position (SS and SW), are capable of injecting 3.8 MWs into the plasma. Design specifications of the neutral beams are required for the beam density model described in chapter 4 and they are as follows: the SS PINI uses the supercusp magnetic configuration producing a beam fractional injection rate of 88:9:3 (% $E_k : E_k/2 : E_k/3$), with a typical voltage and current of 70 kV and 60 A. There are 262 beamlets on the PINI grid directed to a horizontal and vertical focal point 14 m and 6 m respectively, each with a divergence of 0.5 °.The neutralisation efficiency of the PINI is 0.54.

The primary diagnostic used to measure the impurity emission is called the RGB diagnostic. RGB measures six different narrow spectral band-passes simultaneously through a single iris. These spectral band-passes record the plasma and Doppler shifted beam D_α spectral lines, bremsstrahlung emission in the blue and green regions of the spectrum and the He II ($n = 4 \rightarrow 3$) and C VI ($n = 8 \rightarrow 7$) spectral lines induced by charge exchange between the hydrogen beam atoms and the He^{2+} and C^{6+} ions. The spatially and absolutely calibrated (ph/s/m^2/sr) helium and carbon lines are used later to infer He^{2+} and C^{6+} density profiles, which are used for the transport analysis. Helium and methane gas puffs are used to inject controlled amounts helium and carbon into the plasma. The flow-rate of each gas from the gas nozzle has been measured using the fast ion gauge on MAST. Plasma fuelling estimates from the electron density rise during a gas puff experiment suggest a fuelling efficiency of ~ 80 % for helium, and ~ 10 % for methane. Puffs of ≤ 30 ms are thought to be sufficient to perturb the impurity profiles whilst not significantly changing the bulk plasma properties.

A number of plasma parameters are required to constrain the theoretical transport models used later (in chapter 6) which include: T_e, n_e, T_i, v_ϕ, Z_{eff}, q and the Miller parameters. The technique of Doppler broadening is used to measure T_e (from the TS diagnostic) and T_i (from the CELESTE-III diagnostic). n_e is inferred from the amplitude of the scattered spectrum measured by the TS diagnostic. The toroidal speed of the carbon ions are determined by the Doppler shift of the line emission. Bremsstrahlung emission measured by ZEBRA is used to calculate Z_{eff}, however these measurements are less reliable near the plasma edge. The magnetic equilibrium is solved using the EFIT++ code, with constraints provided by the pitch angle (MSE diagnostic), the plasma pressure (TS), and a visible interpretation of the LCFS provided by the D_α emission (from LinCam). An accurate solution of the magnetic equilibrium provides the q profile and is used to fit the Miller parameters.

Chapter 3

Charge Exchange Spectroscopy and Atomic Physics

3.1 Introduction

From the perspective of atomic processes, tokamak plasmas are characterised as 'electron excited' because there is no external radiation field and the plasma itself is largely transparent to its own radiation[1]. That is thermal atoms and ions in the plasma are primarily excited by collisions with free electrons which are generally close to Maxwellian with an electron temperature, T_e, at each point in the plasma. With T_e ranging from a few eV in the edge to core values of several keV, line emission occurs from many ionisation stages over a wide spectral range. In this respect the tokamak is like the solar corona plasma, and is often treated in the solar 'coronal approximation'. The coronal approximation is a zero density approximation balancing collisional excitation/ionisation with radiative decay/recombination. The electron density in the modern tokamak is of order 10^4 higher than the solar corona, so the coronal approximation has to be replaced by the more sophisticated collisional-radiative (CR) model which deals with finite density plasma. Furthermore modern tokamak plasmas have regions that are significantly different in behaviour from the coronal case, which are central to this thesis. At the edge of the plasma there is a significant concentration of neutral hydrogen and this allows a charge transfer reaction from the hydrogen donor to an impurity ion receiver which modifies the local state of excitation and spectral emission called passive charge exchange (PCX) spectroscopy. Also in neutral hydrogen beams, the beam hydrogen atoms act as donors to impurity ion receivers in highly ionised states in the core of the plasma, also modifying the local ionisation state and allowing spectral line emission called active charge exchange spectroscopy (ACX).

In the present analysis of CX based emission, the distribution of receiver impurity ions in the plasma matters, and these are determined by the balance between

[1]There is some self absorption of hydrogen Lyman resonance lines in current machines. In ITER this may extend to a limited set of resonance lines of low ionisation stages of light elements

effective recombination and ionisation, influenced also by the transport of the impurity ions across the plasma. CR theory, based on atomic plasma relaxation time constants, determines the handling of the effective coefficients for establishing the ionisation state and emission in the plasma with transport. This thesis uses an elaborated version of CR theory as the underlying basis of the ionisation stage modelling, called generalised collisional-radiative (GCR) theory which takes account of metastable lifetimes. The CR modelling required for impurity ions as PCX and ACX receivers, beam atoms and their emission, and passive thermal plasma emission are different and are addressed in the following sections.

3.1.1 ADAS

The models and effective rate coefficients used for the analysis in this thesis are stored within the Atomic Data Analysis Structure (ADAS) [26]. ADAS incorporates a suite of computer codes, written in FORTRAN and IDL^{TM}programming languages, designed to model the radiating properties of ions and atoms in plasmas. These codes can be accessed through a set of subroutines that may be incorporated into a user's personal code. Data in ADAS are stored in standard formats, with the various collections given the format names of the form ADF*xx*, with the *xx* indicating the data type. Values in the data set are generally specified on a grid of energies, temperatures and densities. On supplying a set of grid points appropriate to a specific user's calculation, the ADAS extraction routines provide an asymptotic extrapolation of the values stored in the data set. In total, there are more than fifty data types in the ADAS database, however this thesis uses only the specific data types listed in table 3.1: ADF21 and ADF22 data sets provide the beam stopping and emission coefficients described in section 3.4, ADF12 data set provides the effective CX emission coefficients, ADF01 data set is used to provide the n-shell capture cross sections illustrated in figure 3.2, ADF07 and ADF04 data sets provide the electron impact ionisation and excitation rate coefficients used to estimate the ratio of plume to ACX emission and ADF11 provides the various collisional-radiative coefficients required for establishing the ionisation state of impurities.

Table 3.1: ADAS data types used in the present analysis

Data type	Description
ADF01	Bundle-n and bundle-nl charge exchange cross-sections
ADF04	Resolved specific ion fundamental data collections
ADF07	Direct resolved electron impact ionisation data collections
ADF11	Effective ionisation, recombination and CX rate coefficients
ADF12	Effective CX emission coefficients
ADF21	Beam stopping coefficients
ADF22	Effective beam emission coefficient

3.2 Impurity Ionisation Balance

The primary chord-integrated measurements made in this thesis are of the He II ($n = 4 \rightarrow 3$) and C VI ($n = 8 \rightarrow 7$) spectrum lines at $\lambda = 468.5$ nm and $\lambda = 529.1$ nm, which are significantly enhanced by ACX. Modelling of the impurity density is based on the ACX component of these measurements, which is localised to the region along the beam path or its immediate vicinity where the primary beam donors or secondary (halo) donors are present. T_e is sufficiently hot that only He^{2+} and C^{6+} ions exist over virtually all of this path. The passive emission contributing to the spectral line emission is localised at the edge of the plasma with contributions from electron impact excitation and from charge transfer from thermal neutral hydrogen in the edge region. Thus it depends on the fractional abundance of He^{+}, C^{5+} and O^{5+} ions[2] for the electron impact component, whereas the PCX component requires the fully ionised impurities and thermal neutral hydrogen populations to overlap in the same region of plasma.

The fractional abundance of each ion charge state is determined by a balance of effective ionisation and recombination rates (the CR rate coefficients) for each ionisation stage in combination with transport. The CR coefficients are obtained by solution of statistical balance equations containing all relevant collisional, radiative and recombination processes that populate and depopulate the atomic levels [78]. CR theory assumes that excited state populations with short relaxation times (ordinary excited states) are in statistical equilibrium with the instantaneous values of the long-lived ground state populations. This assumption can be validated by comparing the approximate expressions for the metastable, τ_m, and ordinary, τ_o, relaxation times shown in equations 3.1 and 3.2 against the ionisation, τ_{ion}, and recombination, τ_{rec}, timescales given in equations 3.3 and 3.4 [79].

$$\tau_m \sim 10/z^8 \text{ [s]} \tag{3.1}$$

$$\tau_o \sim 10^{-8}/z^4 \text{ [s]} \tag{3.2}$$

$$\tau_{rec} \sim [10^{11} - 10^{13}](1/(z+1)^2)(T_e/I_H)^{1/2}(1/n_e) \quad \text{[s]} \tag{3.3}$$

$$\tau_{ion} \sim [10^{5} - 10^{7}](z+1)^4(I_H/T_e)^{1/2}e^{\chi/T_e}(1/n_e) \quad \text{[s]} \tag{3.4}$$

T_e is in eV, n_e is cm^{-3}, I_H is the ionisation energy of a hydrogen atom (13.6 eV) and χ is the ionisation potential in eV. Note that atomic convention uses centimetres, however the other chapters in this thesis will use metres. For most tokamak plasmas

$$\tau_{plasma} \sim \tau_g \sim \tau_m >> \tau_o \tag{3.5}$$

where τ_g represents the relaxation time of ground state populations of ions (a composite of τ_{rec} and τ_{ion}) and τ_{plasma} represents the time for plasma ion transport across the temperature or density scale lengths. The timescale for redistribution

[2]The O VI ($n = 8 \rightarrow 7$) line occurs at a similar wavelength to the C VI ($n = 8 \rightarrow 7$) line.

of population amongst excited states, τ_{red}, is complicated due to the very large variation in collisional excitation/de-excitation reaction rates with the n-shells of participating states; therefore τ_{red} can span the inequalities of equation 3.5. The timescale orderings are considered in greater detail for fast beam atoms and radially moving impurity ions in section 3.5.

The influence of the ordinary states is condensed and projected on to the ground state population to produce stage to stage CR ionisation and recombination rate coefficients. Helium and carbon atoms have metastable states with relaxation timescales somewhere between ordinary states and ground states. GCR theory can provide resolved CR rate coefficients for these metastable states or unresolved stage to stage rate coefficients by condensing the influence of the metastables on to the ground in a similar manner to the ordinary states [79, 80]. ADAS calculations of ADF11 coefficients for light element ions are performed in the more precise GCR treatment at root, with the less precise CR coefficients being condensed from them. The requirement in this section is the unresolved stage to stage CR effective ionisation and recombination coefficients stored in the ADAS ADF11 data set. They are used to determine the ionisation balance of the helium and carbon ions, and to model the source terms for each ionisation stage in the transport equations described later in chapter 5.

In the following paragraphs, a brief summary is made of the relevant parts of GCR/CR theory. Consider the 'collisional-radiative matrix', $C^{(k,j)}_{i,z}$, where off-diagonal elements for an ion i, z contain the collisional and radiative rate coefficients linking states k and j and diagonal elements $C^{(k,k)}_{i,z}$ contain the total loss rate coefficients from state k. The recombination rate into the level k from the $z+1$ ion is denoted by $r^{(k)}_{i,z}$. The long-lived time dependent levels are denoted by ρ, ϵ and the remaining quasi-static ordinary states are denoted by k and j. The continuity equation for the population densities in matrix form are given in equation 3.6 where an implicit sum over repeated superscript indices is implied.

$$\begin{bmatrix} \frac{dn^{(\rho)}_{i,z}}{dt} \\ 0 \end{bmatrix} = \begin{bmatrix} C^{(\rho,\epsilon)}_{i,z} & C^{(\rho,j)}_{i,z} \\ C^{(k,\epsilon)}_{i,z} & C^{(k,j)}_{i,z} \end{bmatrix} \begin{bmatrix} n^{(\rho)}_{i,z} \\ n^{(j)}_{i,z} \end{bmatrix} + n_e n_{i,z+1} \begin{bmatrix} r^{(\rho)}_{i,z} \\ r^{(k)}_{i,z} \end{bmatrix} \tag{3.6}$$

Expressing the population of quasi-static excited levels as

$$n^{j}_{i,z} = -n_e n_{i,z+1} C^{(j,k)-1}_{i,z} r^{(k)}_{i,z} - C^{(j,k)-1}_{i,z} C^{(k,\rho)}_{i,z} n^{(\rho)}_{i,z} \tag{3.7}$$

and substituting $n^{(j)}_{i,z}$ into equation 3.6 for $n^{(\rho)}_{i,z}$ allows the influence of the excited state populations to be condensed and projected on to the time dependent states

giving the effective GCR ionisation and recombination rate coefficients as [3].

$$S^{\rm CD}_{i,z} = C^{(\rho,\rho)}_{i,z} - C^{(\rho,j)}_{i,z} C^{(j,k)-1}_{i,z} C^{(k,\rho)}_{i,z} \tag{3.8}$$

$$\alpha^{\rm CD}_{i,z} = r^{(\rho)}_{i,z} - C^{(\rho,j)}_{i,z} C^{(j,k)-1}_{i,z} r^{(k)}_{i,z} \tag{3.9}$$

$$\tag{3.10}$$

One component of $r^{(k)}$ is the CX recombination rate coefficient, $q^{(k)}_{\rm CX}$, which is multiplied by $\zeta = n_H/n_e$, where n_H is the hydrogen (or donor) density. This is usually separated from $r^{(k)}$ and quoted as the effective CX recombination rate coefficient, denoted by $C^{\rm CD}_{i,z}$ as

$$C^{\rm CD}_{i,z} = q^{(\rho)}_{\rm CX} - C^{(\rho,j)}_{i,z} C^{(j,k)-1}_{i,z} q^{(k)}_{\rm CX} \tag{3.11}$$

The time dependence of a population of ions in charge state z can be written in terms of these GCR coefficients as shown in equation 3.12.

$$\begin{aligned} \frac{dn_{i,z}}{dt} &= \left(n_e n_{i,z-1} S^{\rm CD}_{i,z-1} + n_e n_{i,z+1} \alpha^{\rm CD}_{i,z+1} + n_H n_{i,z+1} C^{\rm CD}_{i,z+1}\right) \\ &- n_{i,z}\left[n_e S^{\rm CD}_{i,z} + n_e \alpha^{\rm CD}_{i,z} + n_H C^{\rm CD}_{i,z}\right] \end{aligned} \tag{3.12}$$

Note that the terms in $(\ldots)$ and $[\ldots]$ denote the source terms referred to later in chapter 5. In equilibrium ionisation balance, the charge state populations are the solutions of the matrix equation

$$n_e \begin{bmatrix} -S^{\rm CD}_{i,0} & \alpha^{\rm CD}_{i,1} + \zeta C^{\rm CD}_{i,1} & 0 & 0 \\ S^{\rm CD}_{i,0} & -(S^{\rm CD}_{i,1} + \alpha^{\rm CD}_{i,1} + \zeta C^{\rm CD}_{i,1}) & \alpha^{\rm CD}_{i,2} + \zeta C^{\rm CD}_{i,2} & 0 \\ 0 & S^{\rm CD}_{i,1} & . & . \\ 0 & 0 & . & . \end{bmatrix} \begin{bmatrix} n_{i,0} \\ n_{i,1} \\ n_{i,2} \\ . \end{bmatrix} = 0 \tag{3.13}$$

subjection to the normalisation $n^{\rm T}_i = \sum_z n_{i,z}$.

Dashed lines in figure 3.1b and 3.1c represent the fractional abundance of the helium and carbon ionisation stages calculated in ADAS using equation 3.13 with the temperature and density profiles illustrated in figure 3.1a. He^{2+} and C^{6+} ions are dominant over the range $0 \leq r/a \leq 1$ and $0 \leq r/a \leq 0.8$ respectively. Transport also influences the distribution of charge states within the plasma, and this can be accounted for by expanding the total time derivative in equation 3.12 in terms of the particle flux $\mathbf{\Gamma}_{i,z}$ as shown in equation 3.14.

$$\frac{dn_{i,z}}{dt} = \frac{\partial n_{i,z}}{\partial t} + \nabla \cdot \mathbf{\Gamma}_{i,z} \tag{3.14}$$

To model the ionisation balance including transport, a 1.5D transport code named

[3] The suffix CD indicates that the coefficients include dielectronic recombination rates. Note the difference between plasma and atomic physics notation. Usual atomic physics notation uses a superscript z and a subscript CD.

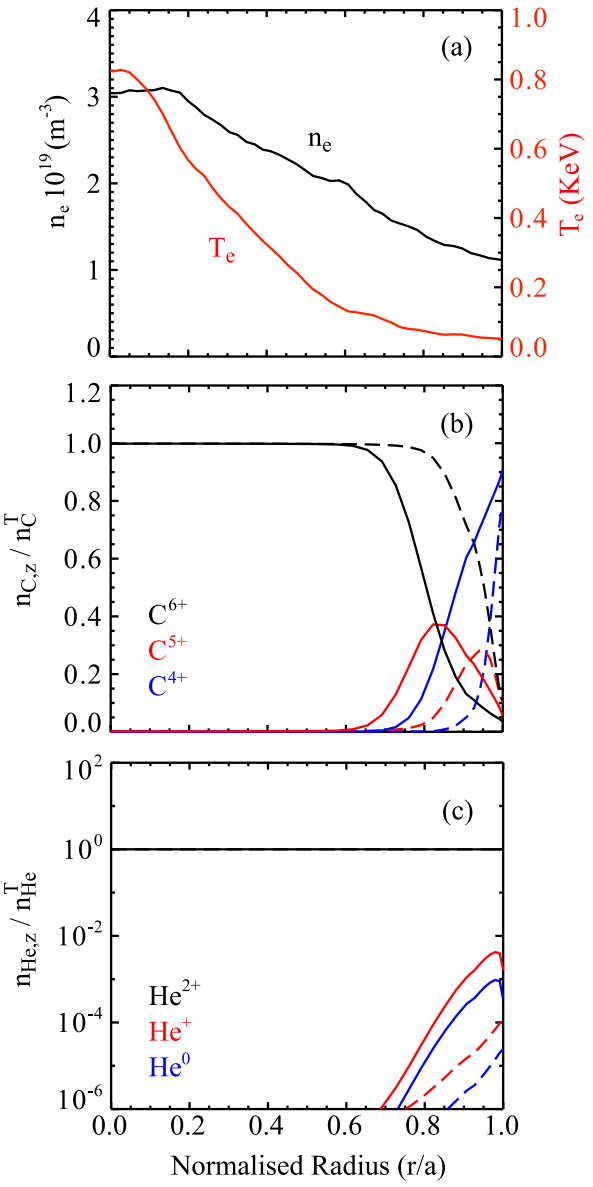

Figure 3.1: (a) Time averaged n_e and T_e profiles from MAST discharge #29424 used to calculate the ionisation balance of helium (b) and carbon (c). The dashed lines are calculated using ADAS assuming zero particle flux and the solid lines are calculated using SANCO assuming a particle flux based on the D_i and v_i profiles from an L-mode discharge (see chapter 5).

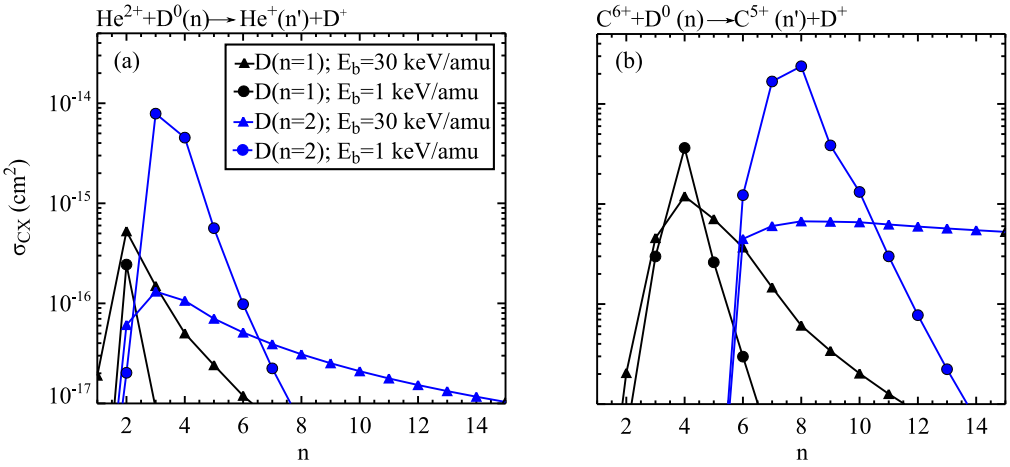

Figure 3.2: The state selective CX capture cross-sections from a beam atom with an electron in the $n = 1$ and $n = 2$ states into a He^+ (a) and C^{5+} (b) ion as a function of principal quantum shell for two different collision energies.

SANCO [81] uses the CR rate coefficients from ADAS and models $\Gamma_{i,z}$ with a radial diffusion, D_i, and convection, v_i, profile. The transport model will be explained in greater detail in chapter 5; here a particle flux typical of an L-mode plasmas is used to illustrate the effect of transport on the ionisation balance. The solid lines in figures 3.1b and 3.1c are calculated using SANCO and demonstrate that transport has a minor effect on the abundance of helium ionisation stages, whereas the fractional abundance of C^{4+} and C^{5+} ions become significant in the range $0.8 \leq r/a \leq 1.0$ in MAST.

3.3 CX Effective Emission Coefficient

The population model required to predict the rate of spectral line emission is a special type of CR model. It includes ACX capture from hydrogen beam atoms into all excited states up to some cut-off principal quantum shell. Tabulations of experimental or theoretical state selective charge exchange cross-section data, stored in the ADAS ADF01, span the important range of principal quantum shells $n_0 < n < n_1$. The method of solution used is called the 'l-redistributive cascade model'. It progresses the solution recursively downwards from the cut-off n-shell using these CX cross-sections in association with spontaneous emission coefficients and both electron and ion impact re-distributive cross-section between l-substates. The population solution therefore progresses downwards in n with lower levels populated by CX and cascading electrons from higher states; no collisional excitation from lower to higher n-shells is allowed although direct collisional-ionisation losses are allowed. The ADAS solution used here works with nl-subshell populations. An alternative ADAS lj-redistributive cascade model works with nlj-sublevels but results are little different and the nl-method results are the most widely used [82].

At this point, it is worth discussing the state selective CX cross-section data

to explain the main difference between thermal and non-thermal CX. Figure 3.2 illustrates these cross-sections as a function of n-shell capture for a thermal and non-thermal collision energy and an $n = 1$ and $n = 2$ donor state population. Thermal hydrogen donors in the $n = 1$ shell tend to transfer into a critical n-shell of the impurity ion, $n_{crit} \sim Z^{3/4}$. Shells around n_{crit} are called the dominant receiver shells. Donation from the $n = 2$ shell populates n-shells approximately $\sim 2n_{crit}$. Levels of the receiver ion above n_{crit} are called sub-dominant levels. Visible spectral line emission from the receiver is between sub-dominant levels, typically with upper level around $2n_{crit}$. At low donor atom speeds, typical of thermal plasma, the selectivity is very strongly into n_{crit} from the ground state donor. Thus thermal CX into the sub-dominant states requires an excited donor (in states $n > 1$). As the beam energy of the donor increases towards that of typical beams, the n-shell selectivity of the capture becomes less pronounced and capture cross-sections to sub-dominant levels approach a fall-off with $\sigma \propto n^{-3}$. Thus at full beam energies it is generally the ground state donor which is most effective in populating the receiver levels emitting visible transitions. Because there are fractional energy components in the beam, both ground and excited donor levels are included.

The chord-integrated ACX line radiance (in ph/s/m^2/sr) can be calculated using the expression

$$\begin{aligned}
\epsilon_{i,z-1}^{(n\to n')} &= \sum_{l,l'} \epsilon_{i,z-1}^{(nl\to n'l')} \\
&= \frac{1}{4\pi}\int_S \sum_{l,l'} A^{(nl\to n'l')} n_{i,z-1}^{(nl)} ds \\
&= \frac{1}{4\pi}\int_S \left(\sum_{l,l'} \frac{A^{(nl\to n'l')} n_{i,z-1}^{(nl)}}{n_b n_{i,z}} \right) n_b n_{i,z} ds \\
&= \frac{1}{4\pi}\int_S q_{eff}^{(n\to n')} n_{i,z} n_b ds \\
&\approx \frac{1}{4\pi} q_{eff}^{(n\to n')} \int_S n_{i,z} n_b ds \\
&\approx \frac{1}{4\pi} q_{eff}^{(n\to n')} n_{i,z} \int_S n_b ds
\end{aligned} \tag{3.15}$$

S is the intersection path length of the line-of-sight and the beam and $A^{(nl\to n'l')}$ is the spontaneous decay rate. The expression (...) is evaluated in the l-redistributive CR model. It depends on local plasma conditions, but is independent of $n_b n_{i,z}$. It is the local CX effective emission coefficient, $q_{eff}^{(n\to n')}$. If the approximation is made that T_e, n_e, B_T etc. are constant along the sight-line S, $q_{eff}^{(n\to n')}$ can be taken outside the integral. The term $\int_S n_{i,z} n_b ds$ is called the 'emission measure'. The further assumption may be made that $n_{i,z}$ is constant along S. The total $q_{eff}^{(n\to n')}$ is dependent on the fraction of donor atoms in the $n = 1, 2, ..., \infty$ shells. However, the fraction of donor atoms in $n = 3$ is of the order of 10^{-4} across most of

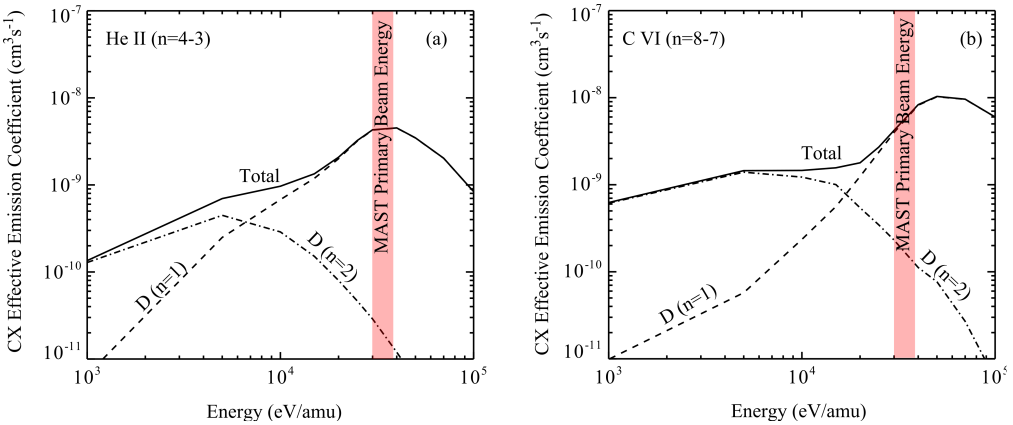

Figure 3.3: The CX effective emission coefficient for the He II ($n = 4 \rightarrow 3$) (a) and C VI ($n = 8 \rightarrow 7$) (b) spectral lines are shown as a function of collision (or beam) energy. The contributions from the $n > 2$ donor atoms are ignored in this analysis.

the temperature and density ranges of interest, therefore the contribution from the $n > 2$ donor atoms is ignored in this analysis. The total $q_{eff}^{(n \rightarrow n')}$ values provided by the ADAS ADF12 dataset for the He II ($4 \rightarrow 3$) and C VI ($8 \rightarrow 7$) spectral lines are illustrated in figures 3.3a and 3.3b respectively; these graphs have accounted for the fraction of donor atoms in the $n = 1$ and $n = 2$ shells using data from the ADF22 dataset.

This model is only used to provide the effective emission rate for the ACX process. Passive emission from electron excitation and thermal CX is separated from the ACX signal using an experimental subtraction technique (discussed later in chapter 4). There are, however, two secondary sources of active emission induced by NBI that are not accounted for in this model which are difficult to separate experimentally from the primary ACX. Firstly, the beam is surrounded by a diffusive 'halo' of thermal neutrals created following the charge transfer between the hydrogen beam donor atoms and the thermal hydrogen ions in the plasma. This thermal halo acts as a secondary donor source for the impurities. The second source of emission stems from the hydrogen-like impurity ions that are created following the ACX reactions. The impurity electron decays to the ground state almost instantaneously and the resultant ion then continues to follow the field lines; these ions are referred to as 'plume' ions [83]. As the plume ions travel around the plasma, there is a probability of secondary emission due to electron excitation which can contribute to different ACX sight-lines. A model for these two processes is presented in the following subsections.

3.3.1 Beam Halo

The ratio of the averaged density of halo atoms to beam atoms (assuming $Z_{eff} = 1$ and neglecting CX ionisation losses for simplicity) is given by $n_h/n_b = q_{\mathrm{CX}}^{\mathrm{TOT}}/q_e^{n \rightarrow \infty}$, where $q_{\mathrm{CX}}^{\mathrm{TOT}}$ and $q_e^{(n \rightarrow \infty)}$ are the total CX rate from a donor beam atom into the receiver halo atom and electron impact ionisation rate respectively. In the core

plasma of MAST ($Z_{eff} \sim 1.2$, $T_e = T_i \sim 1$ keV and $n_e \sim 4 \times 10^{19}$ m^{-3}), $q_e^{(n\to\infty)} \sim 2.2 \times 10^{-8}$ cm^{3}s^{-1} and $q_{\rm CX}^{\rm TOT} \sim 4.6 \times 10^{-8}$ cm^{3}s^{-1} which gives a ratio of ~ 2.1. This ratio will decrease with increasing beam energy and electron temperature.

An estimate of the fraction of $n = 2$ halo atoms can be made by considering a balance of the main populating and de-populating processes of the $n = 2$ halo atom, as shown in equation 3.16 where n_i is the plasma proton density, $q_{\rm CX}^{(k\to n)}$ is the CX rate coefficient from donor state k into receiver shell n, $q_e^{(n\to n')}$ is the electron impact excitation rate coefficient, and $n_b^{(k)}$ and $n_h^{(n)}$ are the hydrogen beam and halo densities in state k and n respectively.

$$\begin{aligned} n_i n_b^{(2)} q_{\rm CX}^{(2\to 2)} + n_e n_h^{(1)} q_e^{(1\to 2)} &= n_h^{(2)} A^{(2\to 1)} + n_e n_h^{(2)} q_e^{(2\to\infty)} \\ n_h^{(2)} &= \frac{n_i n_b^{(2)} q_{\rm CX}^{(2\to 2)} + n_e n_h^{(1)} q_e^{(1\to 2)}}{A^{(2\to 1)} + n_e q_e^{(2\to\infty)}} \\ n_h^{(2)} &\approx \frac{n_e q_{\rm CX}^{(2\to 2)}}{A^{(2\to 1)} + n_e q_e^{(2\to\infty)}} n_b^{(2)} \\ n_h^{(2)} &\approx \frac{n_e q_{\rm CX}^{(2\to 2)}}{A^{(2\to 1)}} n_b^{(2)} \end{aligned} \tag{3.16}$$

The first approximation in equation 3.16 is made because the CX rate from the $n = 2$ beam atom donor into the $n = 2$ halo atom receiver is of the order of 10^{-6} cm^{3}s^{-1}, while the electron collisional excitation rate for $n = 1 \to 2$ is of the order 10^{-12} cm^{3}s^{-1}. The second assumption in equation 3.16 is made because, according to equations 3.2 and 3.4, the spontaneous decay rate of the $n = 2$ shell is of the order of 10^8 s^{-1}, while the electron ionisation rate from $n = 2$ is of the order of 10^7 s^{-1}. It is therefore reasonable to assume that the density of halo atoms in level $n = 2$ is less than or equal to the density of beam atoms in the level $n = 2$, that is $n_h^{(2)} \leq n_b^{(2)}$.

With this approximation, the graphs in figure 3.3 can be used to provide an estimate of the halo atom contribution to the active emission. At thermal energy (1 keV), $q_{\rm CX}^{(n\to n')}$ is approximately two orders of magnitude less than the value at typical beam energies for the He II ($n = 4 \to 3$) line and approximately an order of magnitude less for the C VI ($n = 8 \to 7$) line. One could expect the halo to increase the helium and carbon emission by ~ 2 % and ~ 20 % respectively. This has been tested explicitly (see figure 4.12 in chapter 4) by including a fourth thermal beam fraction representative of the halo within the impurity density calculations.

3.3.2 Plume Ions

Next, consider a plume ion created along the beam path at a radius R_1. The ratio of ACX to plume emission at R_1 can be calculated using the expression

$$\frac{\epsilon_{\rm ACX}^{(n\to n')}}{\epsilon_{\rm PL}^{(n\to n')}} = \frac{\int_S n_{i,z} q_{eff}^{(n\to n')} n_b ds}{\int_S n_{\rm PL} q_e^{(1\to n)} b^{(n\to n')} n_e ds} \tag{3.17}$$

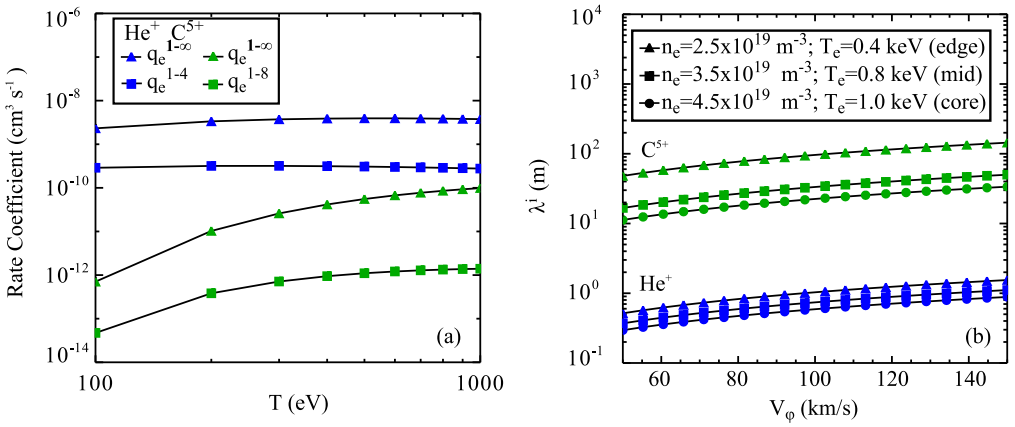

Figure 3.4: (a) The relevant electron impact excitation and ionisation rates for the plume ions and (b) the ionisation mean free path of the He^+ and C^{5+} plume ions as a function of the ion toroidal velocity for three different regions of the plasma.

where $b^{(n\to n')} = A^{(n\to n')}/\sum_{n'} A^{(n\to n')}$ is the dimensionless branching ratio and $n_{\rm PL}$ is the plume density which can be modelled using the expression derived by Bell et al. [84]. The average plume density, $< n_{\rm PL} >$, can be estimated by assuming the plume cloud to have a linear extent of the beam width, $w \sim 15$ cm, plus the ionisation length, $\lambda_{i,z} = v_\phi/n_e q_e^{1\to\infty}$, while the ACX signal is assumed to only originate from the region w. This gives the expression

$$< n_{\rm PL} >= n_{i,z}\frac{n_b q_{cx}^{tot}}{n_e q_e^{1\to\infty}}\frac{w}{w+\lambda_{i,z}} \tag{3.18}$$

where q_{cx}^{tot} is the total CX rate coefficient from all beam donor states into all plume receiver states.

If the integrals in equation 3.17 are approximated by multiplying the mean values of the corresponding densities and rate coefficients by w, then the expression for $< n_{\rm PL} >$ in equation 3.18 can be substituted into equation 3.17 to give

$$\frac{\epsilon_{\rm ACX}^{(n\to n')}}{\epsilon_{\rm PL}^{(n\to n')}} = \frac{q_{eff}^{n\to n'}}{q_{cx}^{tot}}\frac{q_e^{1\to\infty}}{q_e^{(1\to n)}b^{(n\to n')}}\frac{w+\lambda_{i,z}}{w} \tag{3.19}$$

The direct rate coefficients for electron ionisation and excitation are provided by the ADAS ADF07 and ADF04 data sets respectively and illustrated in figure 3.4a. Branching ratios for the $n = 4 \to 3$ and $n = 8 \to 7$ transitions are 0.298 and 0.127 respectively. Figure 3.4b illustrates the dependence of $\lambda_{i,z}$ on v_ϕ for three different values of n_e and T_e. The total rate coefficients for CX into the He^+ and C^{5+} plume ions are both of the order of 10^{-7} cm^3/s. Consider a point along the beam path with $T_e = T_i = 1$ keV, $n_e = 3.5 \times 10^{19}$ m^{-3} and a parallel velocity equal to the thermal velocity. The C^{5+} plume ions have relatively long ionisation lengths and low electron excitation rate coefficients meaning that the plume brightness is negligible compared to the ACX brightness. On the other hand, for He^+ the ACX signal is only around five times brighter than the plume signal.

There is then the issue of the plume ions travelling along the field lines and emitting in sight-lines measuring ACX emission from different regions along the beam path. The ACX emission is dimmer in the core due to the exponential decay of the neutral beam donor atoms, while the plume brightness decays at a rate proportional to $\exp(-L/\lambda_{i,z})$, where L is the distance along the flux surface. In addition, C^{5+} plume ions complete at least one revolution around the plasma and therefore emit in front of and behind the beam volume. However He^{+} plume ions do not complete one revolution and therefore only radiate behind the beam volume (assuming anti-clockwise toroidal I_p flow). If the pitch angle of the magnetic flux surfaces is such that the plume ions don't physically intersect the active sight-lines, then plume emission can be disregarded. A review of the magnetic geometry and RGB sight-lines with respect to the plume emission is given in section 4.3.

3.4 Beam Stopping and Emission

The final ingredient required to model the impurity density is the line-of-sight integrated hydrogen beam donor density. In chapter 2, an expression was derived for the number of beam atoms entering the plasma based on the beam current and voltage. An attenuation model is required to determine how far these hydrogen atoms penetrate into the plasma before ionising (or charge exchanging). This distance can be determined by calculating the CR ionisation coefficient (including loss by charge transfer) of the hydrogen beam atom at each point along the beam path, which in literature is commonly referred to as the beam stopping coefficient. The CR model described in section 3.2 models the hydrogen atoms in a beam by incorporating the beam atom translational velocity in the integrals of cross-sections over Maxwellian distributions. Only populations of complete n-shells are evaluated (the bundle-n approximation) since redistribution among l-substates of the beam atoms is complete, establishing a statistical population of l-substates. More precisely, it is noted that the hydrogen beam atoms experience a large motional Stark electric field which also mixes l-substates of different parity. The substates of n-shells of the moving beam atom are properly represented as Stark manifold states in nkm quantisation. The Stark manifold populations of an n-shell are very close to statistical. Observations of the D_α beam emission show that the radiative transitions are spectrally resolved into motional Stark multiplets. Although there is the capability in ADAS to expand the bundle-n solution over low n-shell Stark states, this is not required in this study since only beam stopping and integral $n \rightarrow n'$ emission are of concern.

Since ionised beam atoms are lost from the beam, there are no recombination processes for the beam. With a steady state neutral beam source ($\partial/\partial t = 0$), the expression in equation 3.12 can be simplified for the beam density along the beam

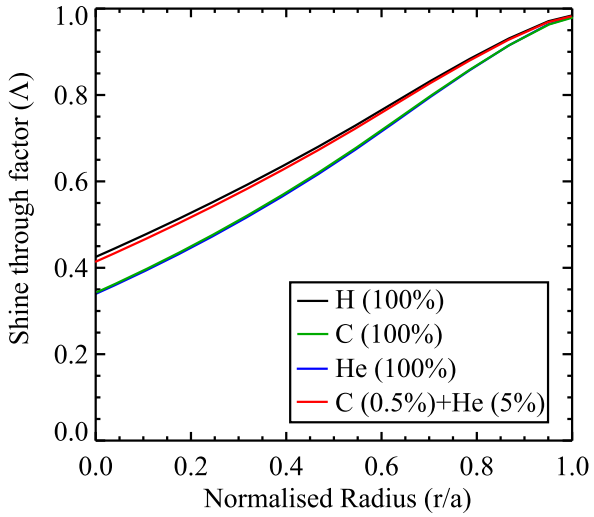

Figure 3.5: The shine through factor for the SS beam with energy 35 keV/amu travelling through the (time-averaged) L-mode plasma #29424.

path, with coordinate l, as

$$\nabla \cdot \mathbf{\Gamma}_b = v_b \frac{dn_b}{dl} = -n_e S_b^{\mathrm{CD}} n_b \tag{3.20}$$

with a general solution for each beam density fraction, F, written as

$$\begin{aligned} n_b^{\mathrm{F}} &= n_L^{\mathrm{F}} \exp\left(-\int_L \frac{n_e}{v_b^{\mathrm{F}}} S_b^{\mathrm{CD}} dl\right) \Phi^{\mathrm{F}} \\ &= n_L^{\mathrm{F}} \Lambda^{\mathrm{F}} \Phi \end{aligned} \tag{3.21}$$

where L is the path length of the beam atoms, n_L^{F} is defined in equation 2.1, v_b^{F} is the beam speed defined in equation 2.2 and $\Lambda^{\mathrm{F}} = \exp\left(-\int_L \frac{n_e}{v_b^{\mathrm{F}}} S_b^{\mathrm{CD}} dl\right)$ is called the shine through factor. Φ includes the divergence and focussing of the beam and has units of m^{-2}. A derivation of Φ is given in section 4.4.

Impurity collisions with the beam atoms play the central role in determining the effective ionisation rate coefficient. The CR model used within ADAS includes arbitrary mixtures of impurity ion colliders. However the associated multi-dimensional look-up tables are unsuitable for fast analysis. Rather, the code is executed for each light impurity species (from H^+ to Ne^{10+}) treating the plasma as composed of a pure species (and its associated electrons). A mixed species beam stopping coefficient is constructed as a linear superposition from these pure solutions as described and assessed by Anderson et al. [85]

$$S_b^{\mathrm{CD}}(E_b, n_e, T_i) = \frac{\sum_i z_i f_i S_{b,i}^{\mathrm{CD}}(E_b, n_{ei}^{equiv}, T_i)}{\sum_i z_i f_i} \tag{3.22}$$

where f_i is the fraction of impurity ion i. Since it is the ions driving the collisionality primarily and not the electrons, the density of impurities is derived from n_e using

the equivalent electron density, n_{ei}^{equiv}, defined as

$$n_{ei}^{equiv} = \frac{n_e}{z_i}\frac{\sum_k z_k^2 f_k}{\sum_k z_k f_k} \tag{3.23}$$

Concentrations of helium and carbon in MAST are generally $< 5\%$ and < 0.5 % respectively (see chapter 4), therefore the inclusion of each impurity in the ionisation calculation is only a minor correction. Figure 3.5b illustrates the Λ factor for a hydrogen beam atom entering the plasma with a beam speed of 35 keV/amu, using the plasma profiles from figure 3.1a. For a pure hydrogen plasma, around half the population of beam atoms ionise after they reach the plasma core. A pure helium or carbon plasma causes an enhanced attenuation of the beam, as shown by the green and blue lines respectively in figure 3.5b, however a difference of $< 1\%$ is found when using typical helium and carbon concentrations found in MAST, as shown by the red line in figure 3.5b.

A benchmark of this beam density model is carried out by comparing the modelled and measured beam D_α ($n = 3-2$) spectral line from the SW beam in MAST (see chapter 4). The intensity of the spectral line driven by excitations may be written as

$$\begin{aligned} \epsilon_b^{(n-n')} &= \sum_{\mathrm{F}=1}^{3}\int_S A^{(n-n')}\frac{n_b^{(n),\mathrm{F}}}{n_e n_b^{\mathrm{F}}} n_e n_b^{\mathrm{F}} ds \\ &= \sum_{\mathrm{F}=1}^{3}\int_S q_{\mathrm{BES}}^{(n-n')} n_e n_b^{\mathrm{F}} ds \end{aligned} \tag{3.24}$$

where $q_{\mathrm{BES}}^{(n-n')}$ is the effective beam emission coefficient stored in the ADF22 data set.

3.5 Atomic, Transport and Beam Timescales

The primary assumption used to obtain the CR rate coefficients is that ordinary states relax rapidly compared to the rate at which the temperature and density are changing spatially and temporally in the plasma. Consider first the time for plasma parameters to evolve in a typical MAST discharge, τ_{plasma}, compared to the spontaneous relaxation time of the ordinary states, τ_o. τ_{plasma} is also used later to define the time for particles to travel across the plasma pressure scale length. According to equation 3.2, the ordinary excited states relax in timescales of ≤ 10 ns. For MAST, the typical current flat-top and diffusion times are of the order of 100 ms and the global energy confinement time of the order of 10 ms. Fluctuations in the electron density caused by plasma turbulence generally have a wave like character with frequencies of the order of 1 μs [12]. Thus it may be assumed that $\tau_{plasma} >> \tau_o$ for plasma ions travelling along closed field lines, where the pressure is spatially constant (see equation 1.3). Transport in MAST causes the impurity ions to move across closed field lines and therefore the pressure is not spatially constant.

Similarly, NBIs direct hydrogen beam atoms towards the plasma core meaning that the pressure changes rapidly in space. Another concern is that an excited beam atom may travel a certain distance across the diagnostic field of view before radiatively decaying. It must be determined whether or not this distance is greater than the spatial resolution of the diagnostic.

The spontaneous decay time, $1/A^{n\rightarrow n'}$, provides an upper limit to the lifetime of each excited atomic state. Collisional excitation/de-excitation processes may decrease the lifetime of the state depending on the plasma collisionality and the n-shell of the participating state. The reciprocal of the diagonal components of the CR matrix created within ADAS provides the exact lifetime of each state and is therefore used in the following paragraphs, along with the spontaneous decay times, to provide a comparison of these various timescales and distances discussed in the paragraph above.

Let the time for particles to travel across the pressure gradient scale length be expressed generically as

$$\tau_{plasma} = \frac{L_p}{v_t} \tag{3.25}$$

where $L_p = -p(\partial p/\partial r)^{-1}$ is the plasma pressure scale length and v_t is the total particle speed defined separately for impurity ions and beam atoms as

$$v_t = \begin{cases} \frac{D_i}{L_{n_{i,z}}} + v_i & \text{Impurity ions} \\ v_b & \text{Beam atoms} \end{cases} \tag{3.26}$$

D_i and v_i are the radial impurity diffusion and convection coefficients, $L_{n_{i,z}}$ is impurity density scale length and v_b is the beam speed defined in equation 2.2.

Consider a He^{2+} ion being transported radially across the plasma cross-section with a constant impurity diffusivity of 1 m^2/s and convection of -20 m/s in the plasma edge (the minus indicating inward transport) and similarly a hydrogen beam atom injected towards the plasma core with an energy of 35 keV/amu. An illustration of τ_{plasma} is given in figure 3.6a for these two cases during an L-mode plasma. It is noted that L_p in H-mode plasmas is typically longer than in L-mode plasmas (except in the steep density pedestal of the H-mode plasma edge). Radial transport of impurity ions across L_p occurs in timescales many orders of magnitude longer than τ_o. On the other hand, fast hydrogen beam atoms travel across the plasma pressure gradient scale length in timescales similar to τ_o.

The exact lifetime of the $n = 2, 3, 4$ shells of the hydrogen beam atom, provided by the diagonal elements of the CR matrix generated in the ADAS model described in section 3.4, are illustrated as a function of n_e in figure 3.6b. At typical MAST densities (10^{19} m^{-3}), the $n = 3$ shell is the longest lived excited state with a lifetime approximately an order of magnitude less than τ_{plasma} in the plasma core. The finite distance travelled by the $n = 3$ hydrogen beam atom during its lifetime is illustrated in figure 3.6c. For MAST beam energies and densities, the distance is of the order

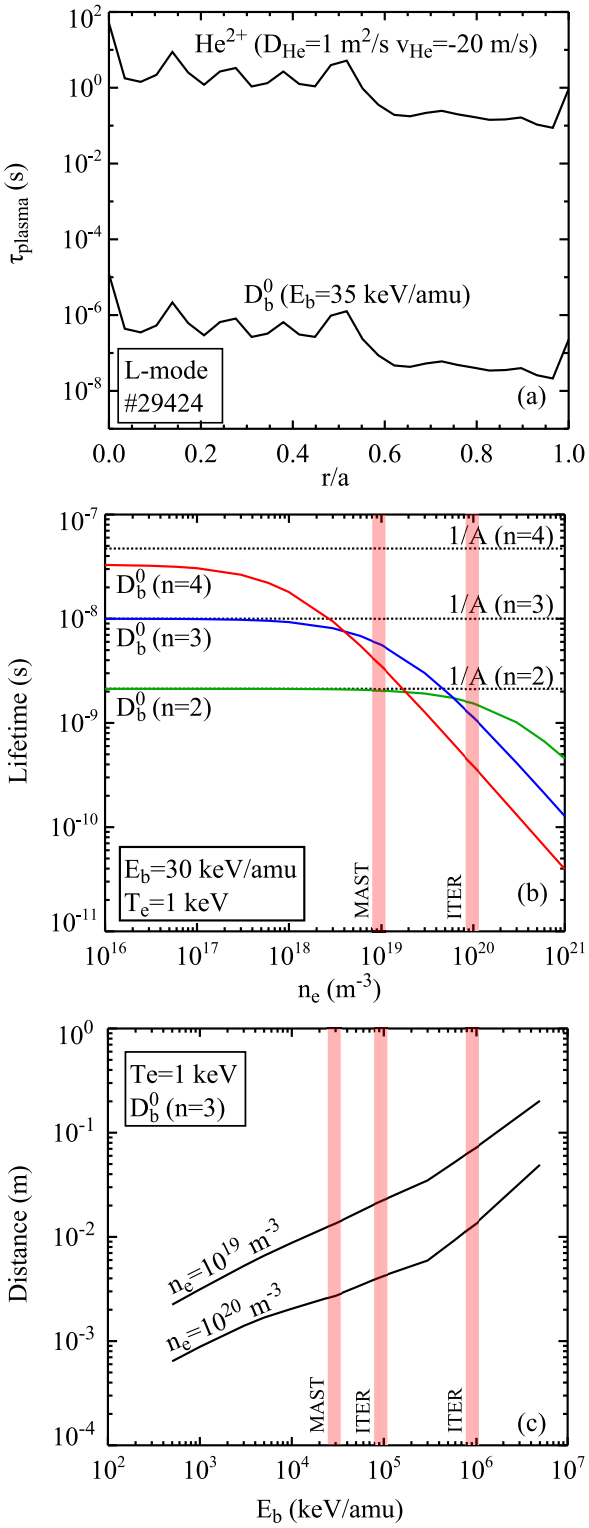

Figure 3.6: (a) The time for He^{2+} ions and D^0 beam atoms to travel across the plasma pressure scale length in the L-mode discharge #29424 as a function of normalised radius. The solid lines in (b) represent the lifetimes of the D_b^0 excited states calculated using ADAS and the dashed lines represent the spontaneous decay rates. (c) The distance travelled by the $n = 3$ beam atom before relaxing to the ground state as a function of beam energy.

of 1 cm. This is sufficient for the purposes of this thesis where the diagnostic spatial resolution is also of the order of 1 cm. It is also noted that, for the expected energies used by diagnostic beams on ITER, the predicted spatial displacement of the beam emission is closer to $\sim$ 1 mm assuming a higher density of the order of 10^{20} m^{-3}. The spatial displacement of the beam emission may increase up to $\sim$ 10 cm at densities of the order of 10^{19} m^{-3} and beam energies of 1 MeV which are predicted for the ITER heating beams.

3.6 Summary

This chapter has discussed three ADAS models that are used to determine the fractional abundance of helium and carbon charge states in the plasma, the CX effective emission rate coefficient and the attenuation and emission rate of the hydrogen beam atoms. The models suggest that the He^{2+} and C^{6+} ions exist over virtually all of the beam path, however a significant fraction of lower ionisation stages exist near the plasma edge for carbon (and to a lesser extent helium) which may reduce the ACX signal in the region $0.8 \leq r/a \leq 1.0$. The amount of secondary emission induced by the beam halo atoms and plume ions has been estimated by considering the balance of the primary atomic processes at play. Emission induced by the beam halo atoms is thought to increase the intensity of the He II ($n = 4 \rightarrow 3$) and C VI ($n = 8 \rightarrow 7$) spectral lines by $\sim$ 2 % and $\sim$ 20 % respectively. Emission from the electron excited plume ions at their point of creation is almost two orders of magnitude less than the ACX emission, however as they travel along the closed field lines and drift in front of different sight-lines their emission may become comparable to the ACX signal. This latter point is addressed further in the next chapter.

Lastly, focus was given to the assumption made in the CR models regarding the ordering of timescales for spontaneous decay time of the excited atomic states, τ_o, and the time for the excited atoms to travel across the plasma pressure gradient scale length, τ_p, that is $\tau_p >> \tau_o$. Radial transport of impurity ions across the plasma pressure gradient scale length occurs in timescales many orders of magnitude longer than τ_o. On the other hand, fast hydrogen beam atoms travel across the plasma pressure gradient scale length in timescales similar to τ_o. An illustration of the exact lifetimes of the excited beam atom states, provided by the CR matrix generated in ADAS, showed that the electron density in MAST is high enough such that collisional processes decrease the lifetime of the excited states to values around half that expected from the spontaneous decay time. The analysis also showed that $n = 3$ shell is the longest lived state and, with a beam energy of 35 keV/amu, may travel $\sim$ 1 cm across the diagnostic field of view before emitting.

Chapter 4

Plasma Scenarios and Measurements

4.1 Introduction

The global energy confinement time, τ_E, is a central parameter in the design of tokamak fusion reactors. The relationship between the thermal helium confinement time, τ_{He}, (which is directly related to the transport) and τ_E can also indicate whether plasma scenarios will be viable for future DT plasma [20]. Previous findings from CTs suggest that $\tau_E/\tau_{He} \sim 1$ [57, 86, 87], however this relationship in an ST has not been studied. It is commonly found in CTs that τ_E is around a factor of two greater in the core of H-mode plasmas compared to L-mode plasmas and scales almost linearly with I_p and weakly with inverse aspect ratio, ϵ, in both L-mode and H-mode plasmas [88]. However previous results from MAST indicate that τ_E exhibits a weaker dependence on I_p in H-mode [89] and stronger dependence on ϵ in L-mode [90]. In the present analysis, time-dependent impurity transport experiments, which involve puffing trace amounts of helium and methane (CH_4) gas into the plasma edge, have been carried out to study the behaviour of helium and carbon during a two point I_p scan in L-mode and a confinement mode scan, specifically L- and H-mode, at constant I_p. T_e, T_i and B_T have been matched in both scans in an attempt to produce essentially one dimensional scans of q_{95} (from the I_p scan) and the n_e gradient (from the confinement mode scan). Although results from MAST previously indicated that τ_E scales weakly with q_{95} in H-mode [91], these scalings have not been tested for impurity transport in L-mode.

The RGB diagnostic produces 2D pixel frames of emission measured through two narrow spectral band-pass filters. Pixels capturing ACX and passive emission in the vicinity of the beam volume are mapped to the plasma major radius by calculating the intersection point between the pixel line of sight and the beam axis. Radial measurements of the background plasma parameters (like n_e, T_i and Z_{eff}) are interpolated onto this radial map to extract the CX effective emission coefficients. The emission captured in pixels immediately above and below the beam and outside

of the halo region is averaged to estimate the magnitude of the passive emission within the beam volume. . The beam density is modelled separately in 3D machine coordinates and combined with the diagnostic sight-lines to provide the impurity density model with line-integrated beam densities. The following sections will review the plasma scenarios and scans used in the analysis and provide further detail of the steps involved in modelling the impurity density.

4.2 Plasma Parameter Scans

Both plasma parameter scans in this thesis begin from the same reference plasma scenario: an L-mode plasma with $I_p = 900$ kA, $B_T = 0.55$ T, additional heating power from the SS NBI of $P_{NBI} = 2.1$ MW, on-axis $n_e = 3.5 \times 10^{-19}$ m^{-3}, $R_0 = 0.83$ m, $a = 0.6$ m, $\kappa = 1.93$ and $\delta = 0.4$. Continuous NBI heating of the plasma is applied from $t = 0.05$ s onwards, meaning that CXS is also available from this time onwards. The plasma has an unconnected double null divertor configuration with deuterium as the working gas. This first scenario is based on the MAST H-mode plasma pulse #22664 described by Valovič et al. [91]. To keep the plasma in L-mode, the vertical position of the magnetic axis was shifted above the equatorial plane of the machine by ~ 5 cm; this technique is particular to MAST and is not general practice on other CTs. Ideally two repeat plasmas should be performed directly after each other, one without and one with a gas puff (and in that order), to obtain the unperturbed plasma profiles. In practice, this was not always achievable due to operation restrictions. Repeat plasmas were run when possible. In a number of the scenarios, the reference for the helium gas puff plasma was taken from the plasma with the methane gas puff, and vice versa for the methane gas puff plasma. This was possible because the gas puffs did not perturb the background plasma. A summary of the plasma parameters listed above are given in the first column of table 4.1. The second and third columns show parameters of two other plasma scenarios discussed in subsections 4.2.1 and 4.2.2.

Time traces of the plasma parameters for the first scenario are illustrated in

Table 4.1: A summary of each plasma scenario described in the text.

	L-mode, High I_p	Low I_p	H-mode
I_p (kA)	900	600	900
Confinement Mode	L-mode	L-mode	H-mode
On-axis n_e (10^{19} m^{-3})	3.5	4.2	3.8
On-axis B_T (T)	0.55	0.55	0.55
P_{NBI} (MW)	2.1	3.2	2.1
q_{95}	5.5	6.3	6.3
Helium pulse # (ref.)	29261 (29424)	29417 (29420)	29275 (29276)
Methane pulse # (ref.)	29424 (29261)	29421 (29417)	29425 (29426)
Helium gas timing (s)	$0.195 - 0.219$	$0.175 - 0.189$	$0.265 - 0.279$
Methane gas timing (s)	$0.185 - 0.219$	$0.160 - 0.189$	$0.240 - 0.279$

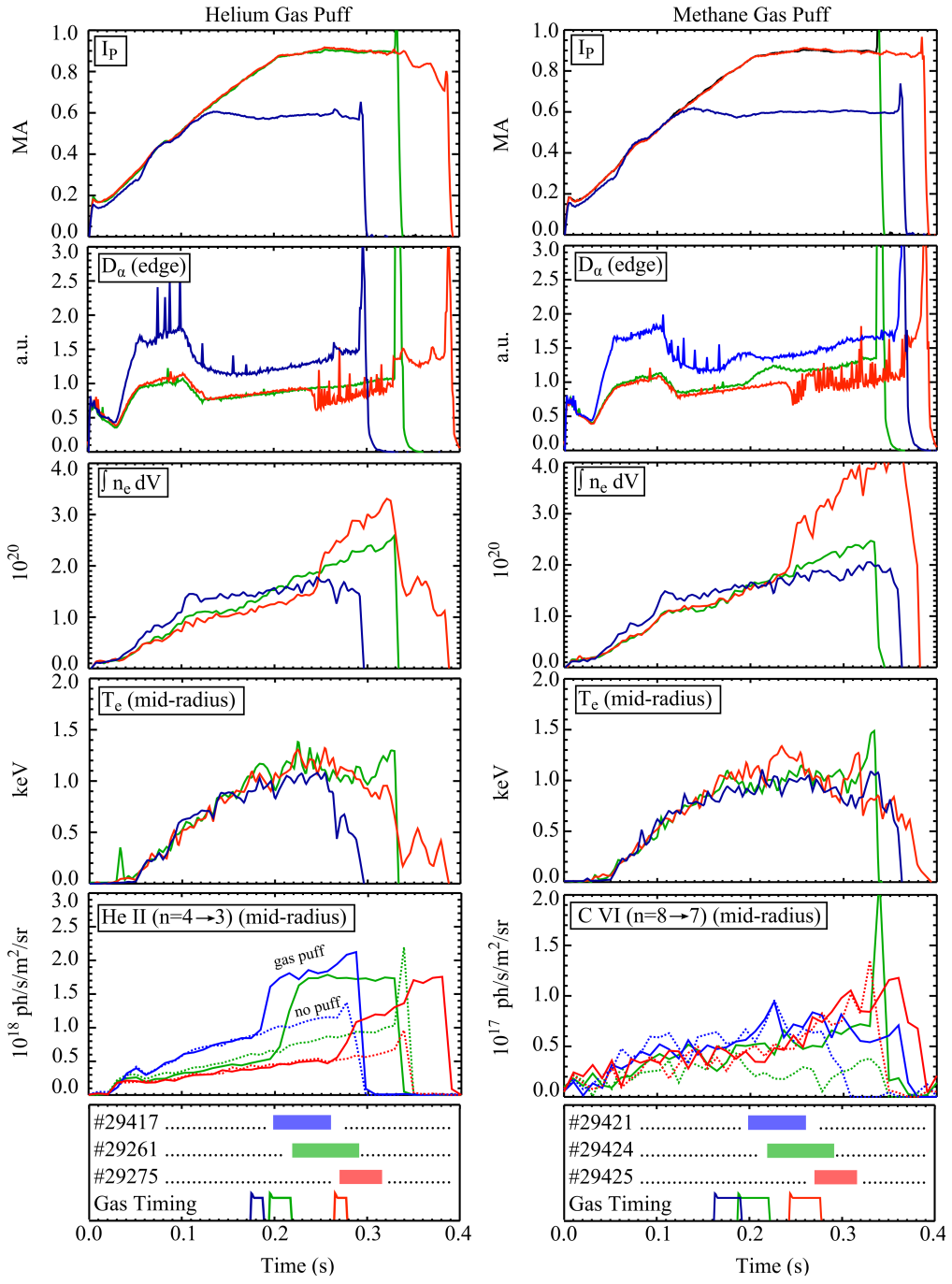

Figure 4.1: Time traces for the plasmas with helium (left) and methane (right) gas puffs. The averaging time periods and gas puff timings are shown at the bottom of both columns.

figure 4.1 by the green lines. Both helium and methane gas puffed plasmas have similar time histories except for the edge D_α emission, where a temporary increase is found during the methane puff but not during the helium puff plasma. This is probably due to the increase in the edge neutral hydrogen density following the dissociation of the injected hydrocarbon. The plasma evolves rapidly during the I_p ramp-up, as shown by the T_e traces, therefore the timing of the gas puff was triggered at the start of the I_p flat-top at $t \sim 0.2$ s. A sharp rise in the He II ($n = 4 \rightarrow 3$) emissivity is found at mid-radius indicating that the helium profile was successfully perturbed by the gas puff. A smaller rise in C VI ($n = 8 \rightarrow 7$) emissivity is found at mid-radius after the methane puff which is possibly due to an overall outflux of intrinsic carbon from the plasma as shown by the decrease in the dotted line representing the intrinsic signal.

The absence of edge localised modes (ELMs) in L-mode allows study of neoclassical and turbulent transport without the perturbations induced by the intermittent MHD phenomena [92]. However MHD activity is always present from a certain time onwards during MAST pulses, as is illustrated in figures 4.2a and 4.2b using the Fourier spectrogram from the inboard Mirnov coils. Frequency sweeping modes, known as fishbone instabilities, evolve at $t \sim 0.26$ s into the internal kink instability known as the 'long-lived mode' (LLM) which occurs at frequencies around $F \sim 20$ kHz [93]. Fishbones eject fast ions from the plasma reducing the heating efficiency of the neutral beam injection [94]. It is not thought that the fishbone instability significantly affects the impurity evolution. LLMs typically occur in MAST plasmas when the core safety factor is ≤ 1.3 and can cause a decrease in toroidal rotation and electron and ion confinement [93]. Since there is no model currently available to analyse the transport of impurities associated with MHD, the time window available for the time-dependent transport experiment is in practice reduced to $50-100$ ms so as to avoid the LLM. The analysis times are shown explicitly by the shaded regions at the bottom of figure 4.1.

Profiles of T_e and n_e from TS, the q-profile solved by EFIT++, Z_{eff} from the deuterium, helium and carbon ions (see equation 4.16) and T_i and v_ϕ measured by CX are time averaged over their respective analysis windows and illustrated by the green lines in figure 4.3. The figure shows only the profiles for the helium puff plasmas. Results from the carbon puff plasmas are similar within the error bars. The radial grid is $\rho = \sqrt{\phi_N}$, where ϕ_N is the toroidal flux normalised to the value at the LCFS. Both neoclassical and gyrokinetic codes used in chapter 6 operate in ρ space and therefore it is helpful in this chapter to map the background plasma profiles, required as inputs for the codes, and the impurity density profiles, required to determine the transport coefficients, in ρ space. Raw emissivity and neutral beam density profiles are still presented in R space, but note that the conversion between ρ, R and r/a for each plasma is demonstrated later in figures 5.5, 5.8 and 5.11. Although the analysis time window only captures the very beginning of the LLM,

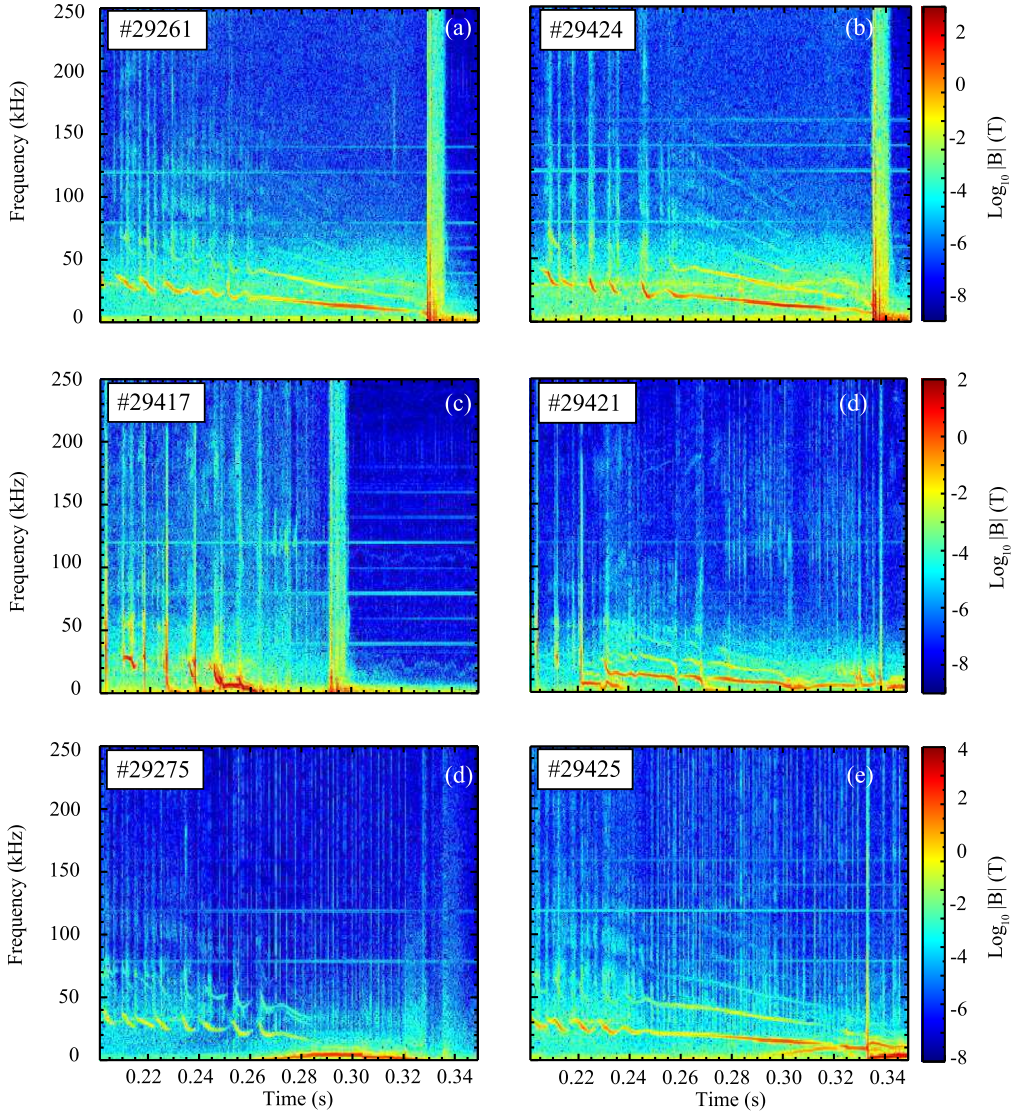

Figure 4.2: The Fourier spectrogram from the inboard Mirnov coils is used to highlight the MHD activity found through the L-mode high I_p plasma (top), the low I_p plasma (middle) and the H-mode plasma (bottom) with helium (left) and methane (right) injections. The sharp spikes in frequency found at the beginning of each scenario are caused by the fishbone instability. These fishbones evolve into a LLM which occurs at ~ 20 kHz. Lower frequency modes are caused by slowly rotating locked modes, like the neoclassical tearing mode (NTM).

flattening of n_e is evident within $\rho < 0.5$. The reason for the flattening is currently unclear, however it is probably caused by MHD activity.

4.2.1 Current Scan

A two point I_p scan in L-mode at fixed B_T was performed by lowering the I_p of the 900 kA L-mode plasma to 600 kA; the 600 kA plasma is referred to as the low I_p scenario. To match T_e and T_i from the high I_p plasma, both the SS and SW NBIs were used, increasing P_{NBI} from 2.1 MW to 3.2 MW. The gas puff timing was triggered earlier at low I_p to coincide with the earlier I_p flat-top. The main gas fuelling rate of the low I_p plasma was increased because n_e is lower at the beginning of the I_p flat-top compared to the high I_p plasma. A sharp rise in the mid-radius He II ($n = 4 \rightarrow 3$) emissivity is found following the helium gas puff, however the C VI ($n = 8 \rightarrow 7$) emissivity remains approximately unchanged following the methane gas puff.

Although the aim of this thesis is not to analyse the effect of impurities on MHD, or vice versa, it is noted that the duration of the low I_p plasma, without a disruption, is increased for the methane injection compared to the helium injection. Z_{eff} remains relatively unchanged during both gas puffs. After $t \sim 250$ ms in low I_p plasma with the helium gas puff, there is evidence of a slowly rotating magnetic island ($F \sim 5$ kHz) caused by a neoclassical tearing mode (NTM), which results in a locked mode as shown in figure 4.2c. For the same plasma, the NTM is replaced by the LLM during the methane injection, as shown in figure 4.2d. The reason the NTM grows into a locked mode during the helium gas puff, but not during the methane gas puff, may be caused by a difference in the local plasma pressure gradient within the magnetic island; a smaller plasma pressure gradient has been shown to increase the size of the NTM [95, 96].

As stated previously, there is no model at present to predict the transport caused by the LLM or NTM, therefore the impurity evolution is only analysed from $t = 0.2 - 0.25$ s during the low I_p plasma. Background plasma parameters averaged over this time period are shown in figure 4.3. The value of q_{95} increases moderately during the low I_p plasma. This q_{95} dependence can be attributed to the scaling law given in equation 4.1 [91].

$$q_{95} = \frac{2\pi a^2 \kappa B_T}{R \mu_0 I_p} \tag{4.1}$$

T_e and T_i profiles are very similar in the both high and low I_p L-mode plasmas because of the additional P_{NBI} applied during the low I_p plasma. Although the volume integrated n_e in both plasmas is similar, a higher value of on-axis n_e is found for the low I_p plasma compared to the high I_p plasma ($4.2 : 3.5 \times 10^{19}$ m^{-3}).

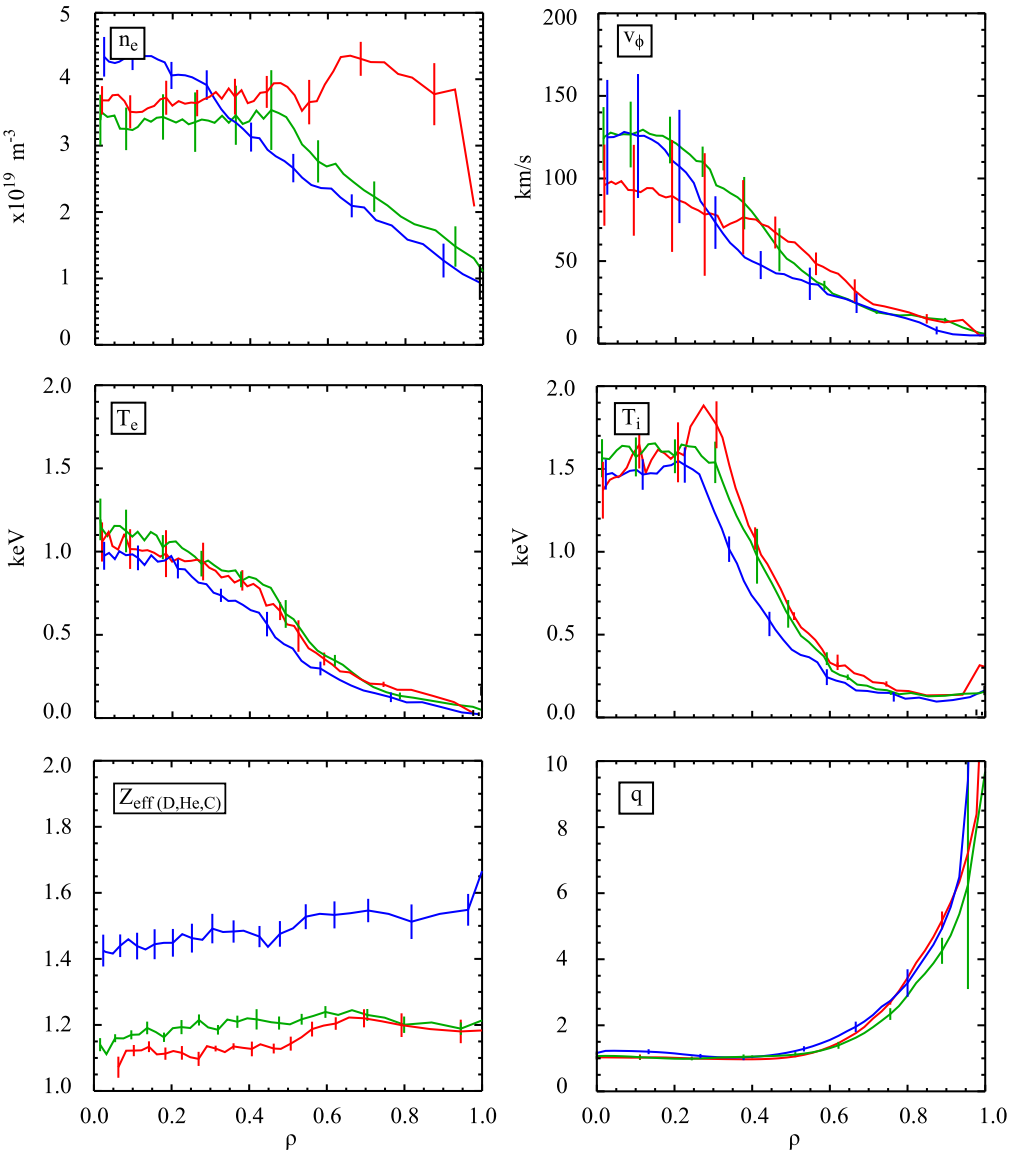

Figure 4.3: The background plasma profiles time averaged over the transport analysis window for the L-mode high I_p plasma (green #29261), the low I_p plasma (blue #29417) and the H-mode plasma (red #29275). The spatial coordinate is $\rho = \sqrt{\phi_N}$.

4.2.2 Confinement Mode Scan

The final scenario, referred to as the H-mode scenario, varied the confinement of the plasma by inducing a controlled L-H mode transition at $t \sim 0.25$ s during the L-mode high I_p plasma. The vertical position of the magnetic axis in L-mode was lowered by ~ 3 cm to induce the transition into an ELMy H-mode. The ELMs can be seen from the red trace in figure 4.1 as sharp, frequent spikes in the edge D_α emission. In this case, instead of triggering the impurity gas puff at the start of the I_p flat-top, it is triggered at the beginning of the H-mode period at $t \sim 0.25$ s. A rise in the He II ($n = 4 \rightarrow 3$) emissivity is measured following the helium gas puff, while the C VI ($n = 8 \rightarrow 7$) emissivity remains again unchanged following the methane gas puff. This shows that a transport analysis of helium is possible in each scenario, while it is only possible in the 900 kA L-mode plasma for carbon.

A difference to the duration of the H-mode phase is found, depending on the choice of the injected impurity gas. The ELMy H-mode period continues for longer during the methane gas puff compared to the helium gas puff, although the total duration of the plasma pulse remains the same during both gas puffs. MHD activity is unavoidable during the H-mode period as shown in figures 4.2e and 4.2f. Similar to the low I_p plasma, an NTM is excited and eventually locks from $t = 0.28 - 0.32$ s during the helium gas puff, while the LLM and NTM coexist together after the methane gas puff until a large sawtooth crash occurs at $t = 0.33$ s. The sawtooth is probably caused by the q profile falling below unity.

Focus is only given to the region of the plasma where MHD effects are expected to be minimal, therefore the evolution is only tracked for $t = 0.27 - 0.32$ s. The increased particle confinement associated with H-mode causes a steep rise in the plasma volume integrated n_e, as shown in figure 4.1. T_e and T_i remain fairly constant since no additional heating was applied during the L-H mode transition. Compared to the L-mode plasma, the time averaged n_e profile is flatter near the outer region of the H-mode plasma in the range $0.5 < \rho < 0.9$. At the very edge of the plasma from $\rho \geq 0.9$, the density profile is very steep and typically called the pedestal region. The density pedestal is characteristic of most H-mode plasmas. A decrease in v_ϕ is found in the region $\rho < 0.4$, which is probably due to the presence of the LLM [93].

4.3 Emissivity Measurements

The 2D pixel frames from the RGB diagnostic span the entire plasma cross-section with a pixel resolution of 640x480 (VGA) and a sampling rate of 200 Hz. The temporal and spatial resolution of RGB must be high enough to ensure that the relevant transport phenomena are captured fully. On the other hand, an advantage of a lower spatial and temporal resolution is that the statistical noise is averaged. Temporal resolution is largely dependent on the impurity particle confinement time, which is assumed here to be $\sim \tau_E$. For MAST, τ_E in H-mode plasmas is approximately 50

ms, while L-mode plasmas are found to be approximately 0.7 times shorter than the H-mode plasmas [90]. Reducing the temporal resolution from 200 Hz to 100 Hz, by averaging every two frames, is acceptable for the predicted confinement times.

To translate the pixel resolution in a radial resolution, the 2D pixel frame must be mapped to the relative R and Z of the SS beam axis. The intersection points in the xy-plane between the pixel (L_1) and SS beam (L_2) line-of-sight are found by solving the two simultaneous parametric line equations 4.2, where $P_1 = (x, y)$ for the pixel line-of-sight with unit vectors $\hat{P_1}$, and $P_2 = (x, y)$ for the beam line-of-sight with equivalent unit vectors $\hat{P_2}$.

$$\begin{aligned} L_1 &= P_1 + t\hat{P_1} \\ L_2 &= P_2 + s\hat{P_2} \end{aligned} \tag{4.2}$$

Solving for t and s when $L_1(t) = L_2(s)$ allows the intersection points to be calculated. The radial resolution of RGB along the SS beam axis is ~ 3 mm. The resolution is not a constant along the beam, since each pixel line-of-sight views the beam at a different angle, however it is reasonable to assume that each pixel line-of-sight has a perpendicular view of the SS beam. This technique can also be carried out for the SW beam, when making comparisons of the modelled and experimental SW beam emission in section 4.4.2. Impurity density profiles from the SW beam are not treated in this analysis because the SW was not operational during the L-mode low I_p plasma, whereas the SS beam was operational during all the plasma scenarios.

The required radial resolution for transport is more complex since it depends on the transport regime. In a classical straight cylindrical plasma with a uniform magnetic field, the diffusion step size, Δr, is of the order of the Larmor radius,

$$\rho_a = \frac{m_a v_{th}}{q_a B_T} \tag{4.3}$$

for species a where v_{th} is the thermal velocity, m_a the species mass and q_a the species charge. In neoclassical transport theory, it is shown in chapter 6 that the toroidal magnetic geometry can increase Δr above classical predictions. Since $\rho_C \approx \rho_{He} \approx 1$ cm, each 2D RGB pixel frame is rebinned over 5 pixels giving a pixel resolution of 128x96 and radial resolution of ~ 1.5 cm. A typical frame of helium and carbon ACX emission, with respect to the R and Z of the SS beam axis, is illustrated in figures 4.4a and 4.4b.

The PCX component is observed across the entire plasma cross-section, while the ACX component follows the Gaussian shape of the neutral beam in the vertical direction. To separate the ACX and PCX emission associated with the SS beam, the emissivity ~ 30 cm above and below the SS beam axis is averaged for each R column to identify the PCX component. This distance is chosen because it is outwith the ACX region and it avoids the brighter emission around the P5 coils. After the PCX has been subtracted, a least squares vertical Gaussian fit of the remaining

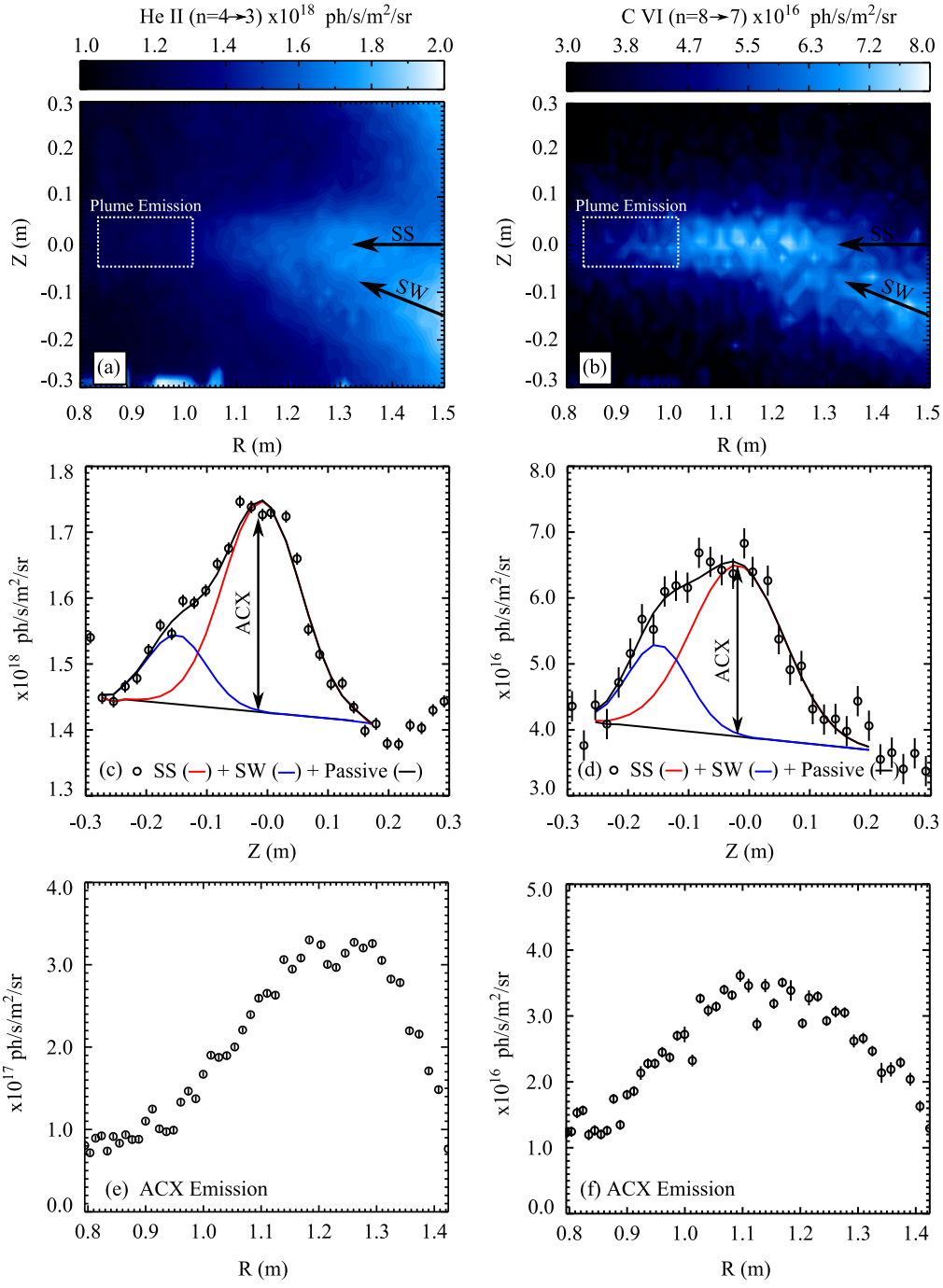

Figure 4.4: Emissivity contours, measured at $t = 0.22$ s during the L-mode 600 kA plasma (left:#29417 and right:#29421) using the two RGB band-passes centred on 468.5 nm and 529.51 nm ($\Delta\lambda \sim 3$ nm), are illustrated in (a) and (b) respectively; R and Z are with respect to the SS beam axis. The vertical Gaussian fits for the SS and SW ACX contributions at $R = 1.3$ m are indicated by the red and blue lines respectively in (c) and (d). Respective radial ACX profiles (for $Z = 0$) are shown in (e) and (f).

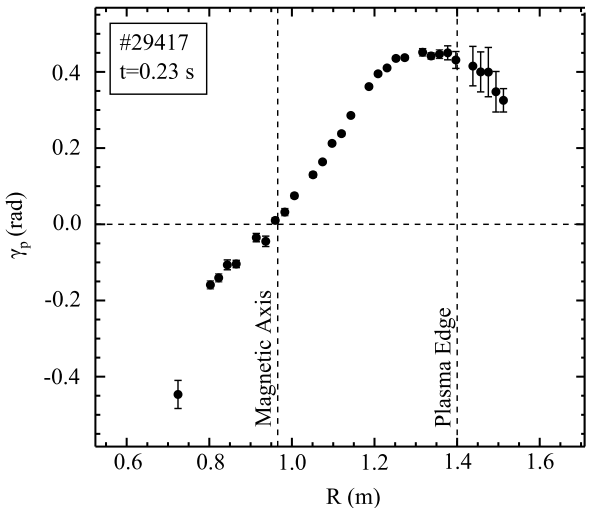

Figure 4.5: A plot of the pitch angle in radians, measured by the MSE diagnostic during the low I_p plasma at $t = 0.23$ s.

ACX emissivities along each R column is performed. Two Gaussian distributions are used in the fitting procedure when the SW beam is operation because it contributes to the ACX emission from the SS beam. An example of the Gaussian fit for one R column with both beams operating is illustrated in figures 4.4c and 4.4d for the He II ($n = 4 \rightarrow 3$) and C VI ($n = 8 \rightarrow 7$) emission respectively. The ACX emission associated with pixels corresponding to $Z = 0$ is then stored as a function of R, as shown in figures 4.4e and 4.4f.

Each pixel line-of-sight views the SS neutral beam approximately along the vessel equator. If a plume ion is vertically displaced by more than $\sim$ 10 cm along the magnetic field line before it has travelled across a different line-of-sight in the xy-plane, it can be assumed that it does not contribute to the ACX emission. For a plume ion travelling approximately 1 m along the field line, the vertical displacement of the plume ion can be approximated by the tangent of the pitch angle, γ_P, meaning that $\gamma_P < 0.15$ radians is required for a plume ion to intersect another sight-line. An example of γ_P, measured by the MSE diagnostic during the MAST pulse #29417 at $t = 0.23$ s, is illustrated in figure 4.5 and shows that γ_P falls below 0.15 radians within $R < 1.0$ m. The effect of the plume emission in this region is observed experimentally in figure 4.4e. The impurity density should be approximately constant in the region around the magnetic axis ($R \sim 0.93$ m), so one should expect to observe a decrease in ACX emissivity due to the exponential decay of the beam density. Instead, the He II ($n = 4 \rightarrow 3$) and C VI ($n = 8 \rightarrow 7$) emission profiles flatten within $R < 1.0$ m. To predict the radial plume emissivity profile, either a model which tracks the magnetic field lines around the plasma or a dedicated experiment (such as the experiment carried out by Bell [84]) would be needed; both of which are beyond the scope of this thesis. Radial n_{He2+} and n_{C6+} profiles are therefore only analysed in the range $R \geq 1.0$ m ($\rho > 0.2$).

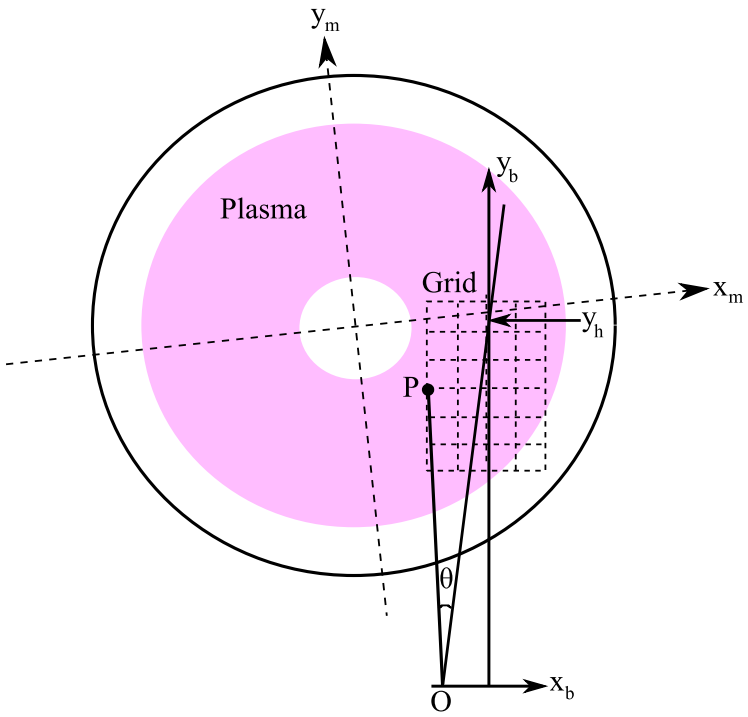

Figure 4.6: A plan drawing of the SS beam trajectory in beam coordinates (x_b, y_b) and in machine coordinates (x_m, y_b). The horizontal focal point of the beamlets is shown by y_h. An example of the grid of points used to interrogate the beam density in the NEBULA code is shown by the dashed rectangle.

4.4 Beam Density Model

To derive the impurity densities from the emissivity profiles, the line-of-sight neutral beam density must be determined. A general description of the beam density, n_b^F, of each beam fraction F is given in equation 3.21. Attention here is given to deriving an expression for the divergence and focussing factor Φ. A significant part of the work of this thesis was devoted to simulating a 3D deposition grid of n_b within the plasma using the IDL^{TM}programming language. The basic equations of photometry and beam shape relevant to neutral beams are explained by Tournianski [97]. The code designed to implement this was titled: NEutral Beam Universal Line-integrated Analysis (NEBULA). A benchmark of NEBULA will be made against experimental measurements from the RGB band-pass filter centred on $\lambda_0 = 660$ nm, that is on the Doppler shifted D_α emission from the SW beam.

NEBULA begins by creating a beam geometry coordinate system, (x_b, y_b, z_b), as shown in figure 4.6. The PINI grid consists of 262 beamlet slits, the trajectories of which are parametrised in terms of the horizontal, y_h, and vertical, y_v, focal lengths of the beam as follows:

$$(x_b, z_b) = \left(\left[1 - \frac{y_b}{y_h} \right] x_0, \left[1 - \frac{y_b}{y_v} \right] z_0 \right), \tag{4.4}$$

At any given point in the plasma, $P(\theta)$, the factor Φ for each beamlet, i, can be

expressed as

$$\Phi(P) = \sum_i \frac{I_i}{r_i^2} \cos\theta_i \quad [\mathrm{m}^{-2}] \tag{4.5}$$

where r_i is the distance OP and θ is the angle which OP makes to the normal of the beamlet. I_i denotes a dimensionless quantity that accounts for the Gaussian divergence of the beamlet and has the form

$$I_i(P) = \Delta_0 \Delta_1 e^{-\left(\frac{\theta_i}{\alpha_i}\right)^2} \tag{4.6}$$

Δ_0 and Δ_1 are normalisation constants and α_i is the divergence angle of each beamlet.

The two normalisation constants, which divide $\sum_i I_i$ between one hemisphere of solid angle, Ω, and the total number of beamlets, b^{tot}, are defined as:

$$\Delta_0 = \frac{1}{2\pi \int_0^\pi e^{-\left(\frac{\theta}{\alpha_i}\right)^2} \sin\theta d\theta} \tag{4.7}$$

$$\Delta_1 = \frac{1}{b^{tot}} \tag{4.8}$$

By substituting the expressions for Δ_0 and Δ_1 into Eq. 4.6, Φ may be written as

$$\Phi(P) = \sum_i \frac{e^{-\left(\frac{\theta_i}{\alpha_i}\right)^2} \cos\theta_i}{2\pi b^{tot} r_i^2 \int_0^\pi e^{-\left(\frac{\theta}{\alpha_i}\right)^2} \sin\theta d\theta} \tag{4.9}$$

Using the expression for n_b^F defined in equation 3.21, and substituting the values of n_L^F and Φ from equations 2.1 and 4.9 respectively, the full expression for n_b^F is

$$n_b^{\mathrm{F}}(P,t) = \frac{I_b^{\mathrm{F}}(t)\epsilon_N}{v_b^{\mathrm{F}}(t)e} \sum_i \frac{e^{-\left(\frac{\theta_i}{\alpha_i}\right)^2} \cos\theta_i}{2\pi b^{tot} r_i^2 \int_0^\pi e^{-\left(\frac{\theta}{\alpha_i}\right)^2} \sin\theta d\theta} \Lambda_i^{\mathrm{F}}(P,t) \tag{4.10}$$

An illustration of the beam density output from NEBULA in beam geometry is shown in figure 4.7.

It is necessary to convert from beam geometry into machine geometry (x_m, y_m, z_m) for two reasons. Firstly, values of S_b^{CD} are interpolated from the ADAS ADF21 data set with local inputs of n_e and T_e from TS measurements converted from machine geometry, and secondly, beam densities are integrated over the line-of-sight using machine geometry. The machine coordinates, which have the same origin as the beam coordinates, can be expressed using the 3D rotation equations,

$$x_m = x_b \cos\sigma_R + y_b \sin\sigma_R - z_b \sin\sigma_R \sin\sigma_T \tag{4.11}$$

$$y_m = -x_b \sin\sigma_R + y_b \cos\sigma_R - z_b \cos\sigma_R \sin\sigma_T \tag{4.12}$$

$$z_m = y_b \sin\sigma_T + z_b \cos\sigma_T \tag{4.13}$$

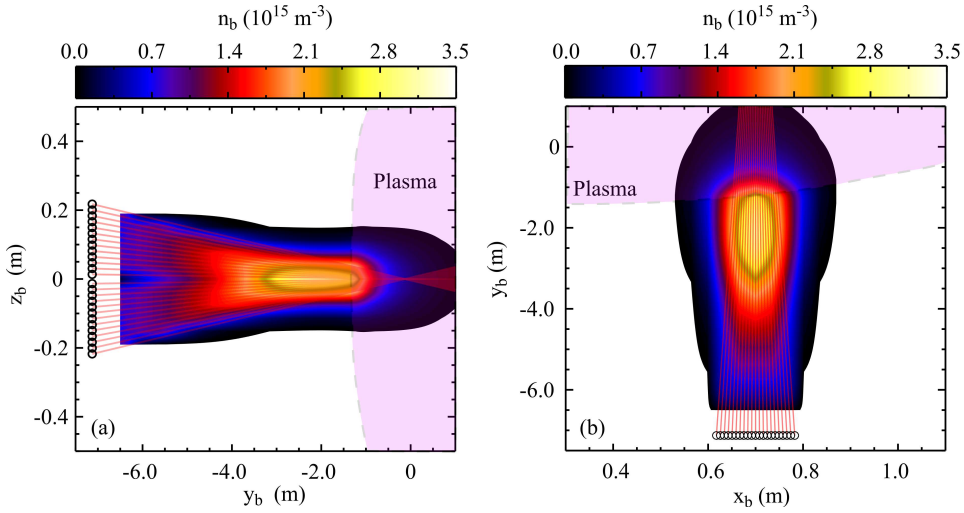

Figure 4.7: Results from NEBULA for a beam power of 1.8 MW are shown by a density contour plot, in beam geometry, through the centre of the neutral beam in the vertical and horizontal plane in (a) and (b) respectively. The red lines indicate the beamlet focal points and the circles represent the PINI grid, where the beamlets originate.

where σ_R is the rotation angle around z_b specified as 64.84° and 4.84° for the SW and SS PINIs respectively and σ_T represents the rotation angle around x_b.

With the RGB line-of-sight unit vectors and camera location, the line-of-sight neutral beam density, defined as $\int n_b^F ds$ where ds is the path integral of the line-of-sight through the beam volume, can be calculated and used to obtain the impurity density profile. An example of each line-of-sight beam density fraction, for the L-mode high I_p plasma at $t = 0.22$ s, is shown in figure 4.8a. One point to note from this graph, is that the second and third beam fractions are attenuated at a faster rate than the main beam fraction. This is illustrated by figure 4.8b, which shows the ratio of each line-of-sight beam density fraction compared to the total line-of-sight beam density. The main beam density fraction is most significant ($> 85\%$) throughout the entire plasma cross section. This is an important point when considering the contribution to the total ACX signal from the neutral beam atoms and the thermal beam halos.

4.4.1 Narrow Beam Approximation

A secondary requirement of NEBULA was the capability of executing between consecutive MAST pulses, requiring that the processing time be less than ∼5 minutes. Reducing the number of modelled beamlets on the PINI grid from 262 to 15 equally spaced beamlets is a simple approximation which can be applied to reduce the processing time of NEBULA without significantly altering the beam density profile. With this approximation, it was found using the IDL function SYSTIME that the code took $\sim$ 0.06 s per grid point (y_b, x_b, z_b). If the neutral beam density is modelled during the entire duration of the pulse ($\sim$ 400 ms), with a temporal resolution of 10 ms and a grid size of 15x11x11 giving a spatial resolution along the beamline of

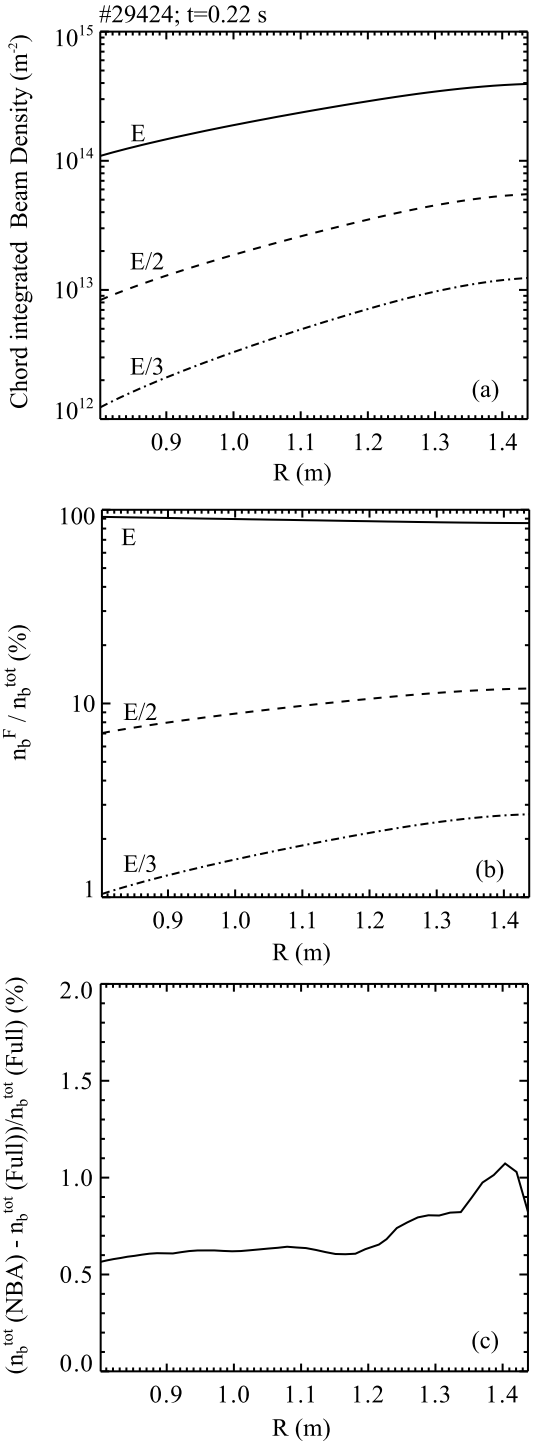

Figure 4.8: This figure illustrates the chord integrated beam density simulations made using NEBULA with respect to the RGB diagnostic. These densities are shown explicitly in (a) for each beam fraction during the L-mode high I_p plasma. The ratio of each integrated beam fraction compared to the total integrated beam density is plotted in (b) and the relative difference between the total integrated beam density modelled using the narrow beam approximation (NBA) and the full model is shown as a percentage in (c).

~ 10 cm, then the code takes ~ 1 hour to run.

Rather than going for a parallel optimisation of the code, a second simplification has been implemented. The assumption, known as the narrow-beam approximation (NBA) [98–100], is that $\Lambda_i^F(P,t)$ can be characterised by following the attenuation of one artificial central beamlet line, with n_b defined in beam geometry in equation 4.14.

$$n_b(P,t)^{\mathrm{F}} = n_L^{\mathrm{F}}(t) \sum_i \Phi_i(P) \Lambda_i^{\mathrm{F}}(y_b,t) \tag{4.14}$$

Two approximations are present in the NBA model: the PINI grid is considered a point source with respect to a point in the plasma and each $x_b z_b$ plane of the beam represents a single magnetic flux surface. Figure 4.8c shows the ratio of the line-of-sight neutral beam profile calculated by the NBA and by the full model. The difference between the two models is $\leq 1\%$. Implementing the NBA model in NEBULA reduced the calculation time per grid point to 1.7 ms which, for the same example described in the previous paragraph, gives a total processing time of ~ 2 minutes.

4.4.2 Beam Emission

To separate the contribution to the D_α spectral line at $\lambda = 656.1$ nm from hydrogen beam atoms and thermal neutral hydrogen in the plasma edge, RGB observes the beam at an angle so that the wavelength of the beam emission is Doppler shifted. However, the viewing angle changes across the beam line meaning that the spectral line is emitted through a range of wavelengths. Consequently the measurement, which is in units of ph/s/m^2/sr/nm, cannot be multiplied simply by one effective filter width to remove the nm^{-1} dependence. The RGB (lower red channel) band-pass filter is shown in figure 4.9a. Although the shifted line wavelength of the main beam energy fraction lies consistently within the centre of the filter, the emission from the second and third beam fractions lie at the edge of the filter for sight-lines observing the beam near the edge of the plasma. The filter attenuation is accounted for in the model by the following method: the effective beam emission coefficient provided by the ADAS ADF22 data set is used to determine the number of photons in units of ph/s/m^3/sr emitted from each hydrogen beam atom (see equation 3.24). The beam emission is integrated through each pixel line-of-sight giving units of ph/s/m^2/sr. The angle between the pixel line-of-sight and the centre of the beam is used to calculate the effective width of the filter using equation 2.3 to give values in units of ph/s/m^2/sr/nm. Lastly, the emission from each beam fraction is summed together and then compared directly with the measured beam emission.

A comparison of the modelled and experiment beam emission from the SW NBI is illustrated in figure 4.9b. A good match in the radial shape of the beam emission is found for $R > 1.1$ m. This is of most importance to transport studies which rely primarily on the impurity density shape rather than the absolute concentration. As

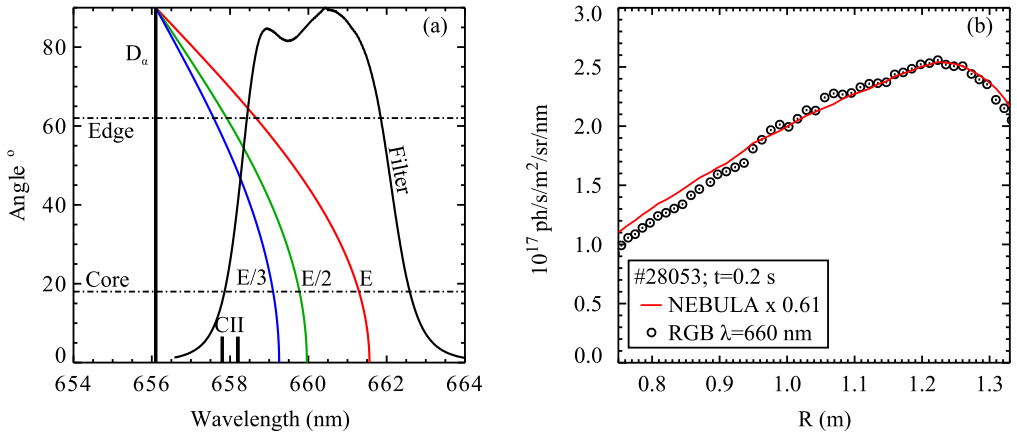

Figure 4.9: (a) The Doppler shifted wavelengths of the D_α beam emission as a function of the line-of-sight angle to the SW beam line. The system band-pass is overplot for reference. (b) A comparison between the SW beam D_α emission measured by the RGB diagnostic and modelled by NEBULA. The filter transmission curve in (a) is applied to each modelled beam fraction.

the beam travels further into the plasma, the modelled beam emission attenuates more slowly than experiment. This could be due either to additional plasma impurities contributing to the attenuation of the beam, or to the exponential error propagation of the beam stopping coefficient. The measured beam emission is a factor of ~ 0.61 times lower than the modelled emission over the entire beam path. A similar over estimation in magnitude of the simulated beam emission was also found in a study on JET [101] and on MAST in the thesis written by McCone [102]. The cause of this discrepancy is currently unknown and is the subject of further work.

4.5 Impurity Density Model

To calculate the impurity density from CXS, equation 3.15 is rewritten in terms of $n_{i,z}$ as

$$n_{i,z} = \frac{4\pi\epsilon_{i,z-1}^{(n\rightarrow n')}}{\sum_{F=1}^{3} q_{eff}^{F,(n\rightarrow n')} \int n_b^F ds} \tag{4.15}$$

First, the effect of the derived impurity concentration on the attenuation of the neutral beam is discussed. For the first iteration of the impurity density deduction, the plasma is assumed to be 100% deuterium. In the second iteration, the derived n_{He2+} and n_{C6+} profiles are included in the calculation of the beam attenuation in the plasma. These iterative steps are continued until convergence is reached. Z_{eff} is close to unity in most plasmas on MAST, therefore the convergence of the calculation occurs after ~ 3 iterations. Figure 4.10 shows the final plasma volume integrated impurity concentrations, $\int n_{He2+}/n_e dV$ and $\int n_{C6+}/n_e dV$, after the third iteration of the impurity density calculation for each plasma.

The intrinsic He^{2+} and C^{6+} concentrations increase during the I_p ramp-up

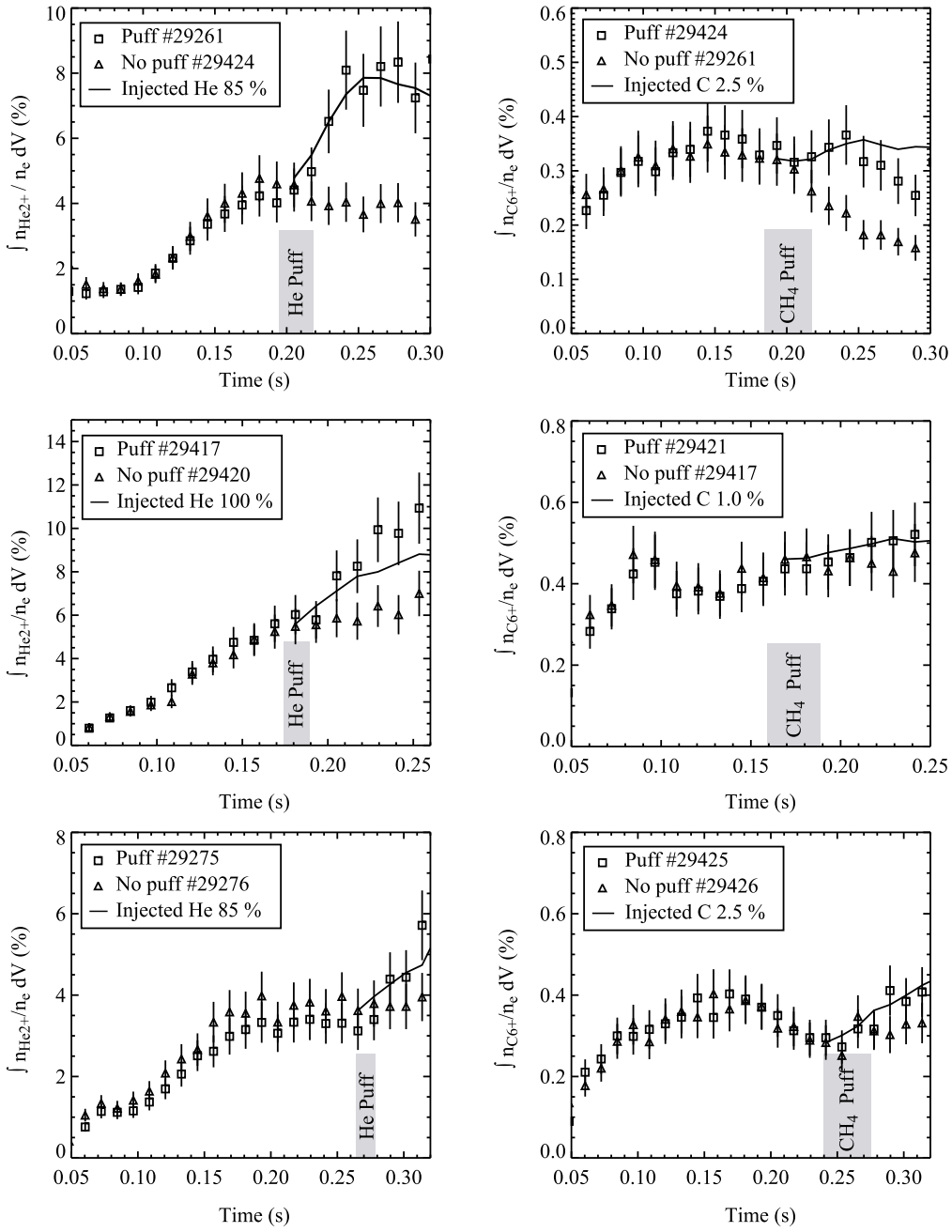

Figure 4.10: The temporal evolution of the plasma volume integrated n_{He2+}/n_e (left) and n_{C6+}/n_e (right) is shown for the L-mode high I_p plasma (top), the low I_p plasma (middle), and the H-mode plasma (bottom). In each plot, the impurity concentration is plotted for the plasma with and without a gas puff. The red line indicates the simulated injected impurity concentration based on the gas influx calibration with a pre-defined fuelling efficiency.

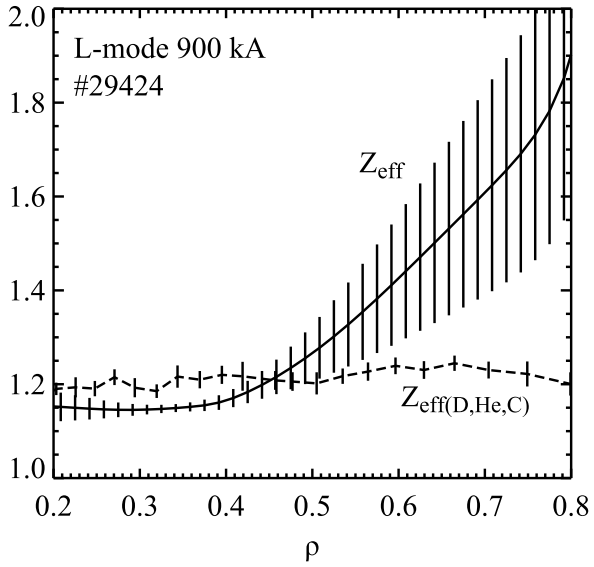

Figure 4.11: A comparison of the Z_{eff}, measured from the Bremsstrahlung radiation, and the $Z_{(D,He,C)}$, calculated using the modelled n_{He2+} and n_{C6+} profiles, for the L-mode high I_p plasma.

phase mainly due to the strong interaction between the plasma and the centre column. During the I_p flat-top, the plasma is moved away from the centre column and the intrinsic He^{2+} generally remains approximately constant while the C^{6+} concentrations either remain constant or decrease. For the L-mode high I_p plasma, the He^{2+} concentration remains constant whereas the C^{6+} decreases. For the low I_p plasma, the He^{2+} concentration continues to increase during the I_p flat-top, while the C^{6+} concentration remains constant. The transition to H-mode does not significantly affect the He^{2+} concentration which remains constant, but it does cause a change to the C^{6+} concentration, where a decrease is found in L-mode and a constant concentration is found in H-mode. These results all indicate a higher recycling rate of helium into the plasma compared to carbon.

A comparison of the concentration with and without the impurity gas puff in figure 4.10 can be used to demonstrate the fuelling efficiency of the gas puff. Intrinsic impurity concentrations on MAST are $n_{He2+}/n_e \sim 0.04$ and $n_{C6+}/n_e \sim 0.004$. A $\sim 85 - 100$ % fuelling efficiency is found for the helium gas puff, which agrees quite well with the fuelling efficiency derived from the TS measurements in section 2.4.2. For the methane gas puff, a fuelling efficiency of the C^{6+} ions is $\sim 1.0 - 2.5$ %, moderately lower than the 10 % fuelling efficiency determined from the TS measurements. In each case, this rise in impurity concentration induced by the gas puff is small enough for the injected impurity to be considered as trace and therefore does not influence the equilibrium background plasma parameters.

To test whether the dominant impurities have been taken into account during the attenuation of the beam, it is important to compare the overall Z_{eff} inferred from Bremsstrahlung measurements with the $Z_{eff(D,He,C)}$ contribution from the

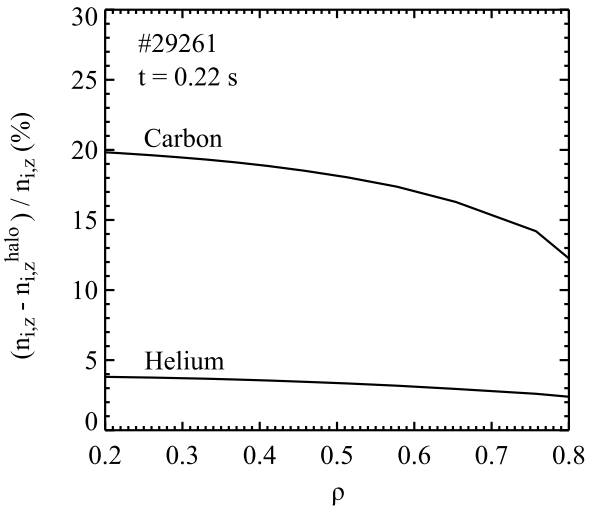

Figure 4.12: A simulation of n_{He2+} and n_{C6+} has been carried with and without an artificial 4^{th} beam fraction representing the halo population around the beam. This plot illustrates the percentage difference between the two simulations for each density.

deuterium, helium and carbon ions defined as

$$Z_{eff(D,He,C)} \quad = \quad 1 + \frac{\sum_{i,z} n_{i,z} z_i (z_i - 1)}{n_e} \tag{4.16}$$

A comparison of Z_{eff} and $Z_{eff(D,He,C)}$ during the L-mode high I_p plasma with no gas puff is shown in figure 4.11. Both measurements suggest an effective charge close to unity in the plasma core, however Z_{eff} increases rapidly near the plasma edge. It is noted that the diagnostic used to measure the Bremsstrahlung also captures molecular emission near the plasma edge which could account for this rise [52]. A similar behaviour is also found the 600 kA L-mode plasma and the H-mode plasma.

The thermal halo atoms situated around the neutral beam can induce secondary ACX emission leading to an overestimation of the impurity concentration. The discussion in section 3.3.1 stated that the halo population is $\sim 2.1 n_b$ and the fraction of $n = 2$ halo atoms is approximately equal to the fraction of $n = 2$ beam atoms. Therefore an estimation of the halo contribution is made by creating an artificial 4^{th} beam fraction with thermal energy. Figure 4.12 shows the percentage difference between the n_{He2+} and n_{C6+} concentrations with and without the addition of this 4^{th} beam fraction. The results suggest that the n_{He2+} and n_{C6+} profiles may be overestimated by $\sim 4\%$ and $\sim 20\%$ respectively, however the halo light does not lead to significant changes of the evaluated impurity density profile shape.

4.5.1 Peaking Factor

A study of the peaking factor, $1/L_{n_{i,z}} = -(1/n_{i,z})\partial n_{i,z}/\partial r$, provides an indication of where the impurities accumulate, whereas the evolution of the injected impurities allows an understanding of the underlying transport mechanisms. A positive peaking factor indicates an inward impurity density gradient and therefore an accumulation

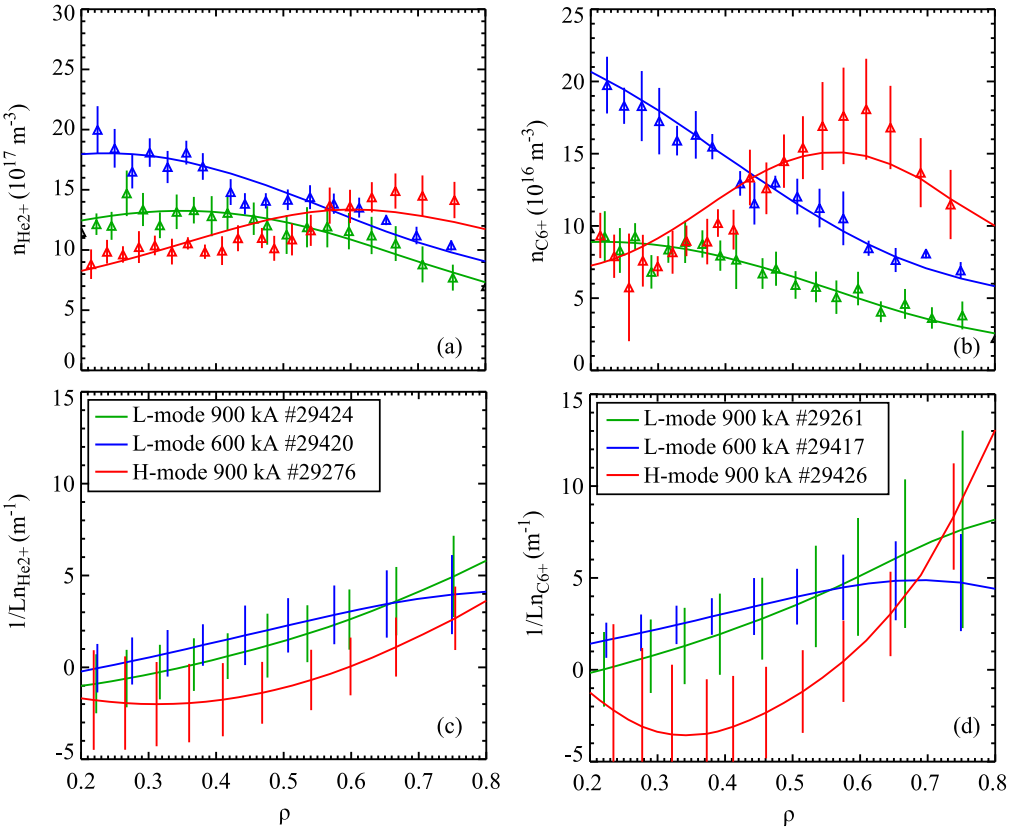

Figure 4.13: Time averaged profiles of n_{He2+} (a) and n_{C6+} (b) are shown for the reference plasmas with no gas puff. The peaking factor, $1/L_{n_{i,z}}$, for both impurities is shown respectively in (c) and (d). These profiles are based on the fits illustrated by the solid lines in (a) and (b).

of impurities in the direction of the plasma core. On the other hand, a negative peaking factor indicates a positive impurity density gradient and therefore a hollow impurity profile. In the limit of zero flux, which is the assumption made for the intrinsic impurities in the plasma without a gas puff, the peaking factor can be shown (see equations $5.1 - 5.3$) to be equal to the ratio of $-v_i/D_i$. If the impurity gas puff does not change the transport properties of the plasma, and it is assumed that it does not, then the zero flux peaking factor should be equal in magnitude to $-v_i/D_i$ derived in the next chapter. It is shown later in figure 6.6 that good agreement is found in general between the transport coefficients and the zero flux peaking factors.

Figures 4.13a and 4.13b illustrate the time averaged intrinsic n_{He2+} and n_{C6+} profiles as a function of ρ during each plasma. The respective peaking factors are also plotted in figures 4.13c and 4.13d. There is little difference between the peaking factors for the high and low I_p L-mode plasmas, however it is clear that a larger concentration of impurities penetrate into the low I_p plasma compared to the high I_p plasma. In H-mode, the impurity profiles are hollow between $0.2 \leq \rho \leq 0.6$ suggesting a significant difference in transport between L-mode and H-mode plasmas. The trends are fairly similar for helium and carbon, however it can be

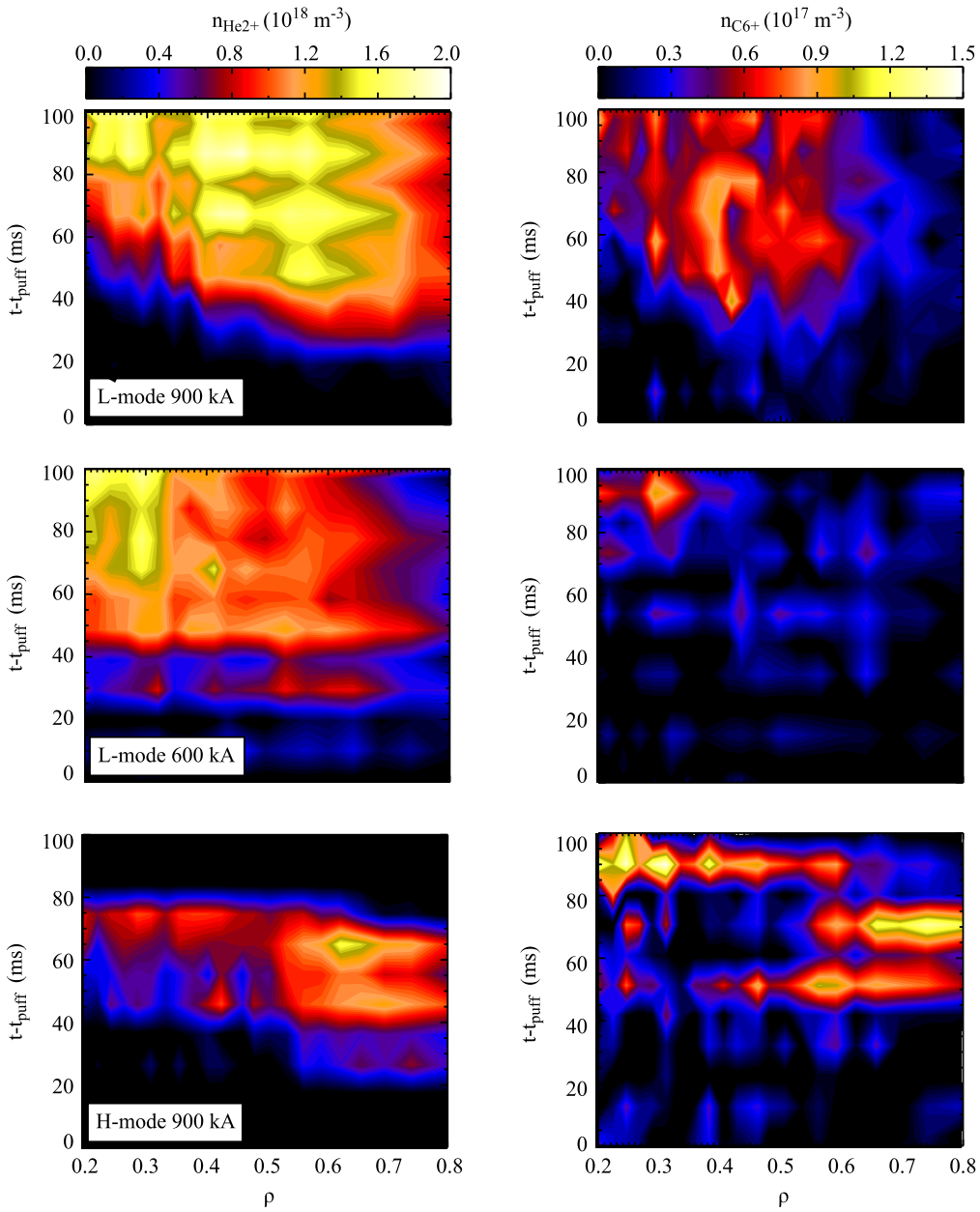

Figure 4.14: Contour plots of the modelled n_{He2+} (left) and n_{C6+} (right) profiles as a function of ρ and t injected from the gas puff during each plasma. The intrinsic n_{He2+} and n_{C6+} profiles has been subtracted to illustrate the evolution of the injected impurities from the plasma edge into the core.

seen that the negative peaking factor in H-mode is larger for carbon compared to helium. In addition, the difference in magnitude between the carbon profiles in each plasma is greater compared to the helium profiles.

4.5.2 Injected Impurity Evolution

The evolution of n_{He2+} and n_{C6+} associated with the helium and methane gas puffs, with the subtracted intrinsic impurity profiles from the reference plasmas, is illustrated in figure 4.14. The evolution of the n_{He2+} profile following the gas puff is clearly observed in the range $0.2 \leq \rho \leq 0.8$ in all three plasmas. The same can be said for the n_{He2+} profile in the L-mode 900 kA plasma, but not the L-mode 600 kA plasma nor the H-mode 900 kA plasma. The resulting evolution of the n_{C6+} profiles during the latter two plasmas are inconclusive as the methane gas puff did not produce a significant perturbation.

For the L-mode high I_p plasma, the carbon seems to penetrate into the mid-radius of the plasma in a shorter time scale than helium, however both impurities reach the inner core on similar time scales. This would suggest a region of higher transport for carbon in the region $0.5 \leq \rho < 0.8$ compared to helium, but similar rates of transport between the two impurities in the region $0.2 \leq \rho < 0.5$. For the I_p scan in L-mode, helium seems to penetrate into the core in a shorter timescale at low I_p compared to high I_p suggesting higher rates of transport at lower I_p. In H-mode, it is difficult to draw any conclusions within $\rho \leq 0.4$, but it is evident that a significant concentration of helium builds up around $\rho \sim 0.6$ in H-mode. An MHD event occurs 60 ms after the gas puff and redistributes helium around the plasma.

4.6 Summary

This chapter has described the plasmas designed to analyse the helium and carbon transport during a two-point scan of I_p in L-mode (600 kA, 900 kA) and a confinement scan (L-H) at 900 kA. The analysis aimed to avoid MHD activity, however towards the end of the L-mode plasmas and throughout the inner core of the H-mode plasma this was not possible. The helium gas puff provided a significant perturbation to the helium density in all three scenarios, however a sufficient perturbation of the carbon density was only achieved in the high I_p L-mode plasma. Gaussian fits are used to distinguish between the ACX and PCX components along each column of the pixel image. This provides a reliable background subtraction of the passive emission. Radial profiles are derived by taking the pixel value of the vertical Gaussian fit closest to $Z = 0$ and storing this for each radial column. The Gaussian fitting does not account for plume or halo emission. Estimates made in this thesis suggest that the plume emission is only significant within the range $\rho < 0.2$, and therefore profiles are not used within this range. Halo emission can cause a 20% over estimation of the carbon profile, and is less significant for helium.

A benchmark of the NEBULA code, designed specifically for this thesis, was carried out by comparing the modelled and experimental beam emission. The degree of attenuation along the beam trajectory is well matched by NEBULA, however the magnitude of the simulated beam emission from NEBULA is greater than experiment. Core values of $Z_{eff(D,He,C)}$, calculated from the modelled impurity concentrations, are in reasonable agreement with the Z_{eff} profile in the core. The zero flux peaking factors of the intrinsic n_{He2+} and n_{C6+} profiles were fairly similar during both L-mode plasmas, but moderately different in H-mode. In the range $0.2 \leq \rho \leq 0.4$, the peaking factors in L-mode are close to zero, but increase with radius in the range $0.4 < \rho \leq 0.8$. In H-mode, both impurities have a hollow profile in the range $0.2 \leq \rho \leq 0.6$, with a moderately inward peaking factor in the range $0.6 < \rho \leq 0.8$. The magnitude of the inward peaking factor in H-mode is generally smaller than the L-mode plasma. The magnitude of the peaking factor in the hollow region is larger for carbon than helium.

Chapter 5

Impurity Transport Coefficients

5.1 Introduction

Transport studies usually characterise the evolution of the impurity flux in terms of radial diffusion, D_i, and convection, v_i, profiles. They provide an estimate of the impurity confinement time in the core plasma which is compared against τ_E to predict whether the fusion produced thermal helium particles quench the fusion burn. Neoclassical and gyrokinetic impurity fluxes can be written in terms of D_i and v_i and compared to the transport coefficients determined from experiment. This allows specific driving mechanisms for transport to be identified and provides a basis for understanding and controlling transport in future tokamaks.

Two methods are used to determine D_i and v_i following the injection of a trace amount of impurity gas into the plasma. 'Trace' implies that the perturbation does not alter the transport or any other background plasma parameters. Shortly after the gas puff, at each point in space, there is an influx phase where the impurity flux is negative and followed by an outflux phase with a positive impurity flux. Plasma pulses on MAST are not long enough to observe this outflux phase. During the influx phase at each point in space, the rate at which the impurity flux decays compared to the impurity density gradient can be interpreted in terms of a D_i and v_i coefficient. This method is advantageous as it does not require any knowledge of the gas fuelling rate into the plasma, however the impurity flux can only be determined in plasma regions where the atomic source coefficients, that is the effective ionisation and recombination rate coefficients, are negligible. Therefore this interpretative method cannot be used to determine the transport coefficients near the plasma edge.

A predictive model, that solves the particle continuity equation with a given set of boundary conditions, can be used to reproduce the impurity density evolution inferred from CXS by using the D_i and v_i coefficients as free parameters in a least squares fit. This model uses the unresolved CR ionisation and recombination coefficients described in chapter 3 to model the atomic source terms and therefore can be used to determine the D_i and v_i coefficients in the plasma edge. However, in reality, the ACX signal from the impurities is weak in the plasma edge, which

typically gives rise to a high degree of uncertainty in the edge transport coefficients. One disadvantage of this method is that, as with any least squares fitting algorithm, there may exist multiple local minima in χ^2 space, so care must be taken to ensure that the solution is physically plausible. The following chapter describes both models in greater detail and presents (and compares) the helium and carbon transport coefficients for each plasma scenario.

5.2 Transport Model

The continuity equation for the impurity ions was defined in equation 3.12, with particular attention on the atomic source rate coefficients. Focus is now given to the impurity flux which contains the physics of impurity transport. Equation 3.12 is re-written more compactly as

$$\frac{\partial n_{i,z}}{\partial t} = -\nabla \cdot \mathbf{\Gamma}_{i,z} + S_{i,z} \tag{5.1}$$

with $S_{i,z}$ representing the sources from ionisation, recombination and CX. The common ansatz describing the impurity flux, $\mathbf{\Gamma}_{i,z}$, is written as

$$\mathbf{\Gamma}_{i,z} = -D_i \nabla n_{i,z} + \mathbf{v}_i n_{i,z} \tag{5.2}$$

A negative flux implies that the impurity ions are flowing towards the core of the plasma and the assumption is made that D_i and $\mathbf{v}_i$ are the same for all charge states of the impurity. D_i is always positive and therefore acts in the opposite direction to the impurity density gradient, whereas $\mathbf{v}_i$ can be positive or negative depending on the physical driving mechanism for the transport.

Using equation 5.2, the zero-flux ($\mathbf{\Gamma}_{i,z} = 0$) peaking factor, defined as $1/L_{n_{i,z}}$, can be written as

$$\frac{1}{L_{n_{i,z}}} = -\frac{|\nabla n_{i,z}|}{n_{i,z}} = -\frac{|\mathbf{v}_i|}{D_i}. \tag{5.3}$$

where $|\nabla n_{i,z}| \sim \partial n_{i,z}/\partial r$ and $|\mathbf{v}_i| \sim v_i(r)$. The magnitude of the peaking factor informs on the amount of accumulation and the sign reveals the direction of the particle convection since D_i is always positive. For zero-flux, only the ratio of v_i/D_i can be determined from experiment. This is known as the 'ambiguity problem'. A transient event, such as a sawtooth, ELM or short gas puff, disturbs the impurity equilibrium ($\mathbf{\Gamma}_{i,z} \neq 0$) and allows D_i and $\mathbf{v}_i$ to be evaluated separately, rather than as a ratio. The two models that determine D_i and $\mathbf{v}_i$ use equations 5.1 and 5.2 and are discussed next in section 5.2.1 and 5.2.2.

5.2.1 UTC-SANCO Approach

The first method of determining the D_i and $\mathbf{v}_i$ coefficients uses a 1.5D[1] radial transport code, called SANCO [81], to solve equation 5.1 for the impurity density with a given set of boundary conditions and a description of the impurity flux (in terms of equation 5.2). One of the benefits of SANCO is that it uses the CR ionisation, recombination and CX rate coefficients provided by the ADAS ADF11 data set to determine the atomic source terms for each ionisation stage. To interpolate these coefficients from the data set, T_e, T_i, n_e and n_i as a function of r/a and t must be supplied as inputs to SANCO. A simplification of the magnetic equilibrium is used in SANCO. Firstly, the plasma profiles and transport coefficients are assumed to be flux surface averages and secondly, a cylindrical geometry is used. The former simplification assumes that there is no asymmetry between the HFS and LFS of the plasma. This is justified on MAST, since no significant asymmetries are found in the TS or SXR measurements. The latter simplification could be cause for error on MAST due to the triangular shape of the plasma, however the error is not thought to exceed the typical error bars of the transport coefficients. In cylindrical geometry, the transport equations are re-written as

$$\frac{\partial n_{i,z}(r,t)}{\partial t} = -\frac{1}{r}\frac{\partial}{\partial r}(r\Gamma_{i,z}(r,t)) + S_{i,z}(r,t) \tag{5.4}$$

$$\Gamma_{i,z}(r,t) = -D_i(r,t)\frac{\partial n_{i,z}(r,t)}{\partial r} + v_i(r,t)n_{i,z}(r,t) \tag{5.5}$$

where the radial coordinate $r = \sqrt{V/2\pi^2 R_0}$ is based on the enclosed plasma volume of a flux surface, V. D_i and v_i are given as a function of r and t, however usually these coefficients are assumed to be constant in time over the analysis window; in fact, the second method of determining the transport coefficients relies on this assumption.

An arbitrary (but realistic) set of parametrised radial D_i and v_i profiles are specified by the user as an initial match to the experimental and modelled impurity density evolution. The Universal Transport Code (UTC) [58,103] uses the Levenberg-Marquardt least-squares fitting algorithm to determine best fit values of the free parameters, p_i, which include the D_i and v_i profiles and also ϵ_F. The algorithm proceeds by varying the free parameters by a small amount, δp_i, (typically 10 %) to obtain the partial derivatives,

$$\frac{\partial f_n}{\partial p_i} = \frac{f_n' - f_n}{\delta p_i} \tag{5.6}$$

where f_n corresponds to the predicted quantity. Corrections to δp_i are then obtained

[1] SANCO works in 1.5D because it includes a simplified SOL where ions may travel poloidally along the field lines to and from the divertor. This simplified SOL regulates the influx rate of particles into the LCFS.

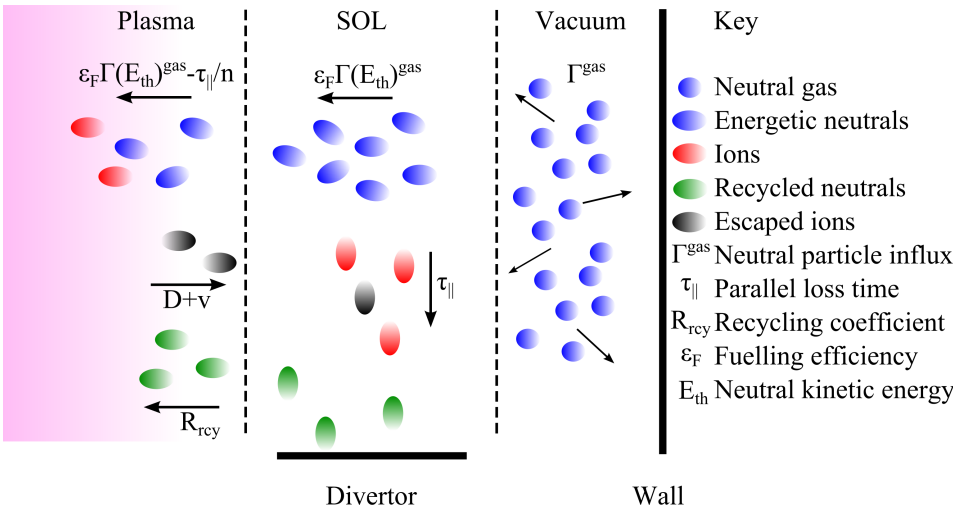

Figure 5.1: An illustration of the simplified SOL used by SANCO to model the influx of neutral atoms into the plasma.

by inverting $M_{i,j}\Delta p_i = b_i$. The matrix $M_{i,j}$ and vector b_i are defined as

$$M_{i,j} = \sum_{n=1}^{N} \frac{\partial f_n}{\partial p_i}\frac{\partial f_n}{\partial p_j} w_n \tag{5.7}$$

and

$$b_i = -\sum_{n=1}^{N} \frac{\partial f_n}{\partial p_i}(f_n - y_n) w_n \tag{5.8}$$

where w_n signifies the weighting of each data point and y_n corresponds to the measured quantity. The normalised covariance matrix, C^N, is defined as

$$C^N_{i,j} = \begin{cases} \frac{C_{i,j}}{\sqrt{C_{i,i}C_{j,j}}} & \text{i} \neq \text{j} \\ \sqrt{C_{i,j}} & \text{i} = \text{j} \end{cases} \tag{5.9}$$

where $C_{i,j} = M^{-1}_{i,j}$. Diagonal and non-diagonal elements reflect the errors and covariance in the free parameters respectively. However, these errors only represent the range of p_i which provide the same solution of χ^2. If the solution is not the global minimum, then the physical solution may not be within the limits of the error bars.

SANCO models the flux of neutral impurities entering the plasma by creating a simplified SOL and plasma edge description, which is illustrated in figure 5.1. There are five main inputs to the model: the neutral particle influx, Γ^{gas}, the parallel loss time, $\tau_{||}$, the effective recycling coefficient, R_{rcy}, the fuelling efficiency, ϵ_F, and the thermal kinetic energy of the neutral atoms E_{th}. Γ^{gas} and ϵ_F are described in section 2.4 of chapter 3. An accurate description of the remaining parameters requires complex models which are not considered in this work. Instead, various estimates are made based on physical assumptions.

Atoms and molecules leaving the gas valve have thermal velocities corresponding to room temperature. As they interact with the SOL plasma, the molecules dissociate at a threshold T_e forming atoms with Franck-Condon, or breakup energies, of a few eV. The atoms are kinetically energised by elastic collisions and CX reactions with plasma ions, however their ionisation times are too short for them to thermalise fully with the SOL plasma (generally around $10 - 20$ eV on MAST), therefore the assumption is made that $E_{th} \sim 2$ eV [58, 104]. The value of E_{th} determines the distance that the neutral particles travel into the plasma before ionising. For $E_{th} = 2$ eV, the neutrals travel ≤ 10 cm into the core plasma. Underestimating E_{th} will cause an overestimation of D_i and v_i over the range in r up to the maximum penetration depth of the neutrals.

A neutral impurity atom ionised in the SOL via CX reaction forms part of the neutral influx into the core plasma otherwise, as ions, they will be transported along the field lines towards the divertor plates. It is important to estimate the impurity ion transit time to the divertor plates to predict the number of recycled impurities re-entering the plasma. This transit time, $\tau_{||}$, can be estimated using the expression

$$\tau_{||} = \frac{Rq_{95}}{\sqrt{2E_{th}/m}} \tag{5.10}$$

where Rq_{95} is the connection length. For example, in the L-mode high I_p plasma, the connection length is calculated using $R \sim 1.4$ m and $q_{95} \sim 15$ to give 21 m, so that a He^+ ion with $E_{th} = 2$ eV will take ~ 2 ms to travel to the divertor.

The fraction of particles recycled into the plasma is denoted as R_{rcy}. This parameter is principally dependent on the divertor configuration and difficult to predict. In most divertor configurations, helium is primarily recycled back into the plasma with $R_{rcy} \rightarrow 1$. With a cryopump applied with an argon frost layer, the recycling rate has been shown to reduce to $R_{rcy} = 0.85 - 0.95$ [105, 106]. The divertor in MAST does not have a cryopump and therefore the recycling is expected to be close to unity for helium. Conversely, carbon is extremely reactive and tends to stick to the divertor material and the assumption is made that $R_{rcy} \rightarrow 0$.

The edge model coefficients are only a basic estimate of the complex processes occurring in the plasma edge ans SOL. These simplifications are a weakness of the present use of SANCO, although SANCO can be coupled to edge models that seek to model these coefficients with more accuracy, but these models are not used in this thesis. Instead, the transport coefficients are compared with a second model (described in the next subsection) which does not rely on a model of the plasma edge parameters.

5.2.2 Flux Gradient Approach

The second method of determining the transport coefficients uses the interpretative approach described in two previous studies [57, 87]. Reducing the problem to

cylindrical coordinates and integrating equation 5.4 over r with the expression for $\Gamma_{i,z}$ given in equation 5.5 yields

$$\begin{aligned}\frac{1}{rn_{i,z}(r,t)}\frac{\partial}{\partial t}\int_0^r n_{i,z}(r,t)r'dr' &= D_i(r,t)\frac{1}{n_{i,z}(r,t)}\frac{\partial n_{i,z}(r,t)}{\partial r} - v_i(r,t) \\ &+ \frac{1}{n_{i,z}}\int_0^r S_{i,z}(r,t)dr' \end{aligned} \quad (5.11)$$

Consider a radial region of plasma where $S_{i,z} \approx 0$ and where the plasma transport is constant in time (i.e. $D_i(r,t) \equiv D_i(r)$). At each point in space, equation 5.11 can be re-written in the linear form $y = mx + c$, where the term on the LHS of equation 5.11 is y, the spatial gradient is x, the gradient (m) is D_i and the y-intercept (c) is $-v_i$. Both y and x are determined directly from impurity density measurements inferred from CXS and fitted as a function of time at each point in space, with the fit providing the D_i and v_i coefficients. This method will be referred to as the Flux Gradient (FG) method.

Although the FG and UTC-SANCO methods both deduce the transport coefficients from fits to the experimental impurity density evolution, the FG method is a more direct approach as it does not need to solve the transport equation or rely on any simplified edge model. However one disadvantage of the FG method is that it breaks down in regions where $S_{i,z}$ becomes non-negligible. An attempt is made in this analysis to provide a robust evaluation of the transport coefficients based on results from the FG and UTC-SANCO methods. One should find agreement between the two codes, within the error bars of the transport coefficients, in the limit of $S_{i,z} = 0$. Disagreement may occur if the solution of the least squares fit during the UTC-SANCO method is not the global minimum. The FG method is extremely sensitive to noise in the impurity density profiles, since the transport coefficients are determined from the evolution of two gradients. Therefore it is necessary to smooth the density profiles in time and space to average out the noise. It has been found that a representation of $n_{i,z}$, which is smooth in time and space, can be made by fitting the following temporal functions to each spatial location [57]:

$$n_{i,z}(r,t) = \begin{cases} A_1 + A_2\tanh[A_3(t-A_0)] & \text{r/a} \leq 0.5;\ \text{t} > 0 \\ A_1 + A_2\exp[-A_3(t-A_0)^2] & \text{r/a} > 0.5;\ \text{t} \leq A_0 \\ A_1 + A_2\exp[-A_4(t-A_0)^2] & \text{r/a} > 0.5;\ \text{t} > A_0 \end{cases} \quad (5.12)$$

Once values of A_1, A_2, A_3 and A_4 have been determined for every spatial point, a 5^{th} order polynomial fit is made to the spatial profile for every moment in time. Carrying out the fitting in this order produced satisfactory smooth gradients in both time and space. The density evolution inside the region $\rho = 0.2$ is treated by interpolating the fit, whilst ensuring a density greater than zero.

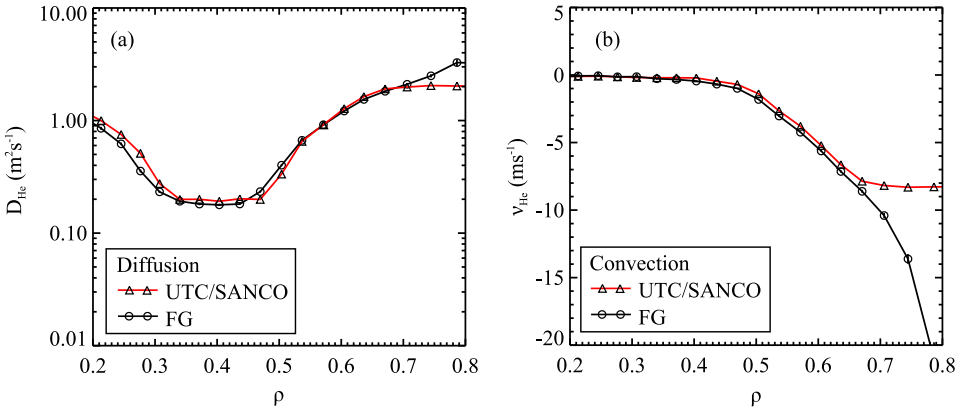

Figure 5.2: The FG code is benchmarked against the UTC-SANCO method. The red line shows the D_{He} and v_{He} profile used by SANCO to simulate n_{He2+}. The D_{He} and v_{He} coefficients determined by applying the FG method to n_{He2+} are illustrated by the black lines.

5.2.3 Flux Gradient Benchmark

The UTC-SANCO method has been used and documented in a number of studies (for example by Giroud et al. [58]) and can therefore be considered benchmarked. A code has been developed for this thesis to determine the transport coefficients using the FG method and therefore requires benchmarking. Consider an $n_{i,z}$ profile modelled using SANCO with an arbitrary D_{He} and v_{He} profile based on the expected neoclassical predictions described in chapter 6 (illustrated by the red line in figures 5.2a and 5.2b respectively). Applying the FG method to the simulated $n_{i,z}$ should return the same pre-defined D_{He} and v_{He} profile. For this benchmark, the edge influx conditions and source terms for $n_{i,z}$ are calculated using the L-mode high I_p plasma conditions (described in table 5.1). As described in chapter 4, $\rho = \sqrt{\phi_N}$, where ϕ_N is the normalised toroidal flux. The conversion between ρ, R and r/a is given in figure 5.5.

The FG method produces a good match in D_{He} and v_{He} in the range of $\rho < 0.7$, illustrated by the comparison of the red (SANCO) and black (FG) lines in figures 5.2a and 5.2b respectively. The increase in D_{He} and v_{He}, calculated by the FG method in the range $\rho \geq 0.7$, is due to the non-negligible source terms. In coronal equilibrium, one would not expect significant sources as far into the plasma as $\rho = 0.7$. In this case however, the energy of the injected neutrals is sufficient to allow penetration further into the plasma. Since the simulated density has been created with conditions designed to represent the experimental plasma conditions, the FG D_{He} and v_{He} will only be quoted for the region of $\rho < 0.7$. The source terms for C^{6+} are significant further into the plasma, therefore FG D_C and v_C coefficients are only quoted for $\rho < 0.6$.

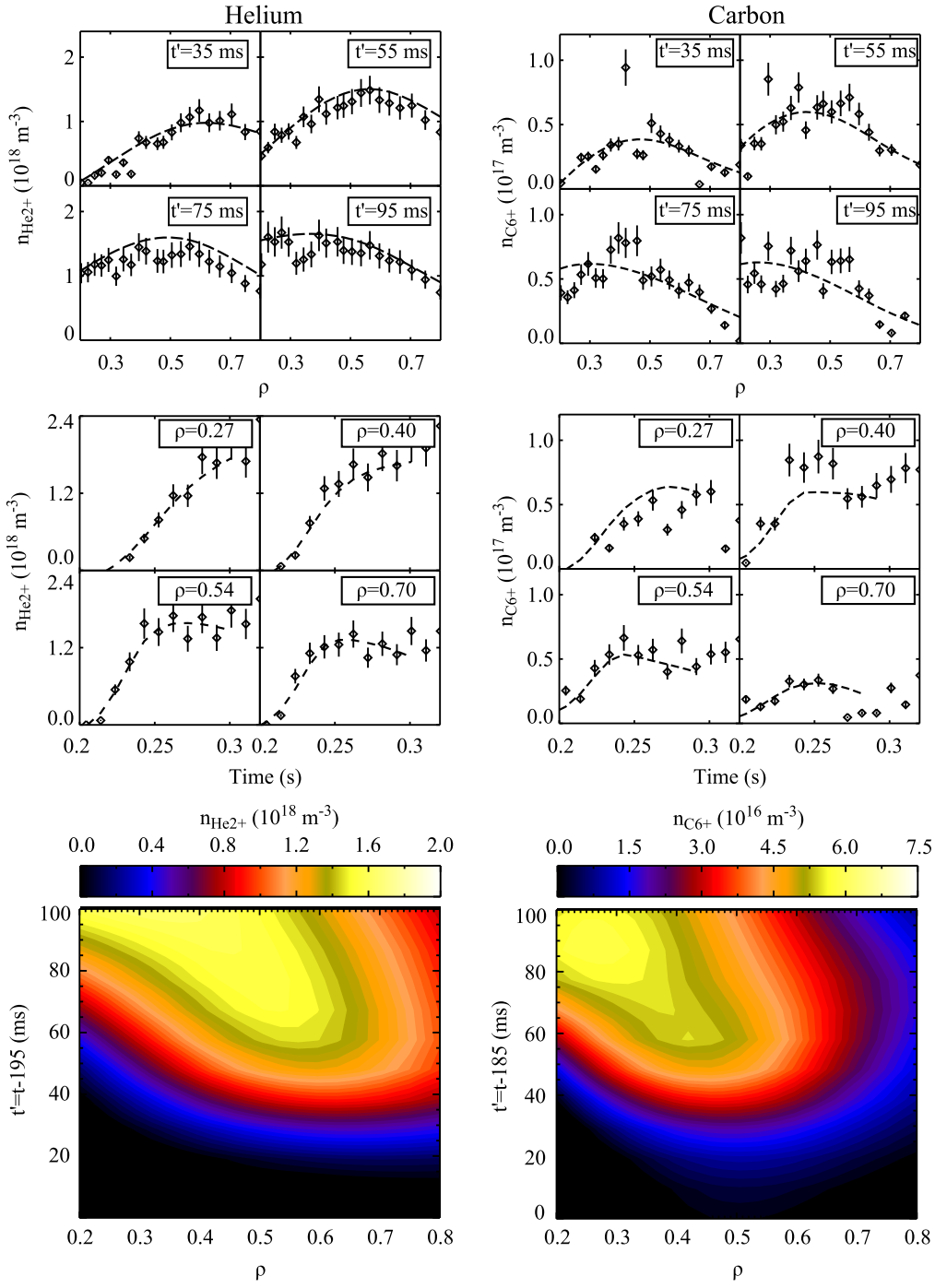

Figure 5.3: A comparison of the fitted and experimental n_{He2+} (left) and n_{C6+} (right) profiles for the L-mode high I_p plasma as a function ρ (top), t (middle) and ρ and t (bottom).

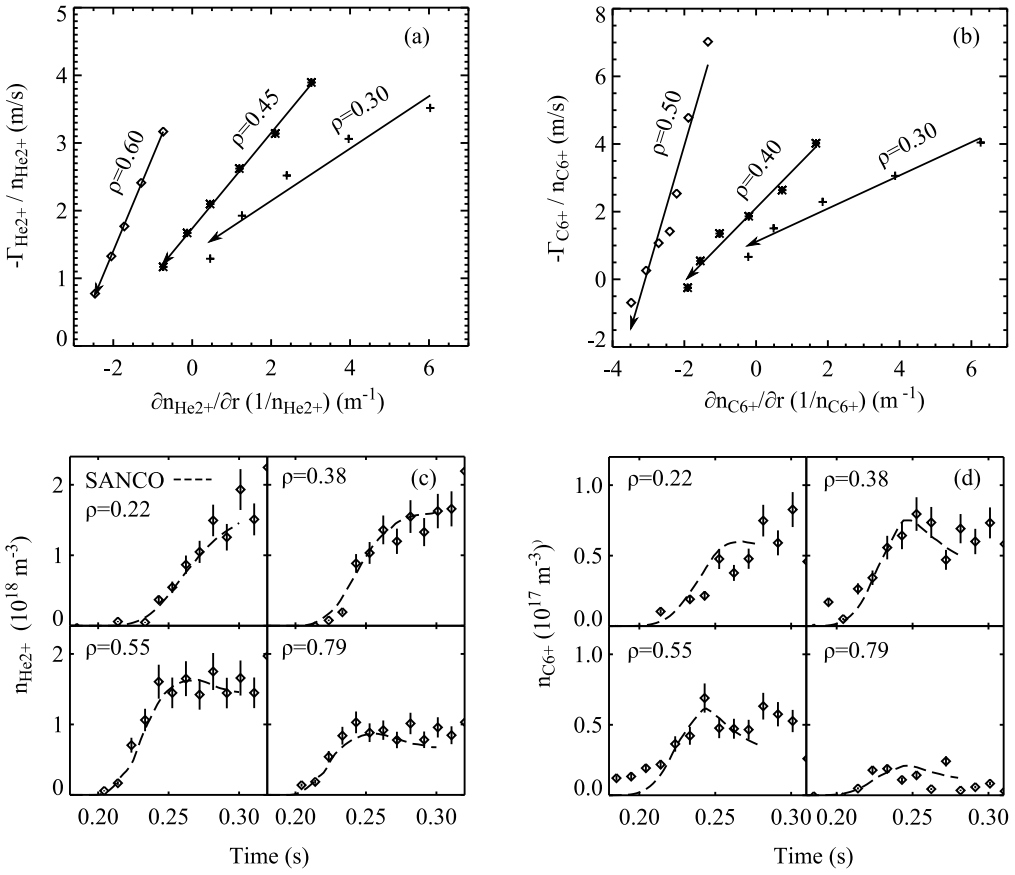

Figure 5.4: This figure shows an example of the fitting procedures required to determine the helium (left) and carbon (right) transport coefficients for the L-mode high I_p plasma. The top two graphs show the linear fits (solid lines) made for the FG method at three different values of ρ for both impurities, while the two sets of four graphs at the bottom compare the simulated SANCO n_{He2+} (dashed lines) with the experimental n_{He2+} profiles.

5.3 Impurity Charge Scan

A transport analysis of both n_{He2+} and n_{C6+} is possible in the L-mode high I_p plasma. An example of the fitted and experimental n_{He2+} and n_{C6+} profiles following the helium and methane gas puffs is shown in figure 5.3. In the plasma core, the n_{C6+} rises faster than n_{He2+}, suggesting a larger inward flux for carbon. The temporal evolution of $-\Gamma_{He2+}$ and $-\Gamma_{C6+}$ are shown as a function of $\partial n_{He2+}/\partial r$ and $\partial n_{C6+}/\partial r$ in figures 5.4a and 5.4b respectively. The arrows on the linear fits indicate the direction in time following the gas puff. The bottom two graphs of figure 5.4 show the fit between the experimental and modelled impurity density from SANCO. Table 5.1 lists the edge model parameters used in SANCO for each impurity. A moderately higher fuelling efficiency of $\epsilon = 1.0$ and $\epsilon = 0.04$ was needed for helium and carbon respectively compared to the values illustrated in figure 4.10 of $\epsilon \sim 0.85$ and $\epsilon \sim 0.025$. $\tau_{||}$ is determined using $E_{th} = 2$ eV. As expected, a value of η_F close to unity was also required to produce the best fit.

The D_i and v_i coefficients deduced from both methods are shown in figures 5.5a

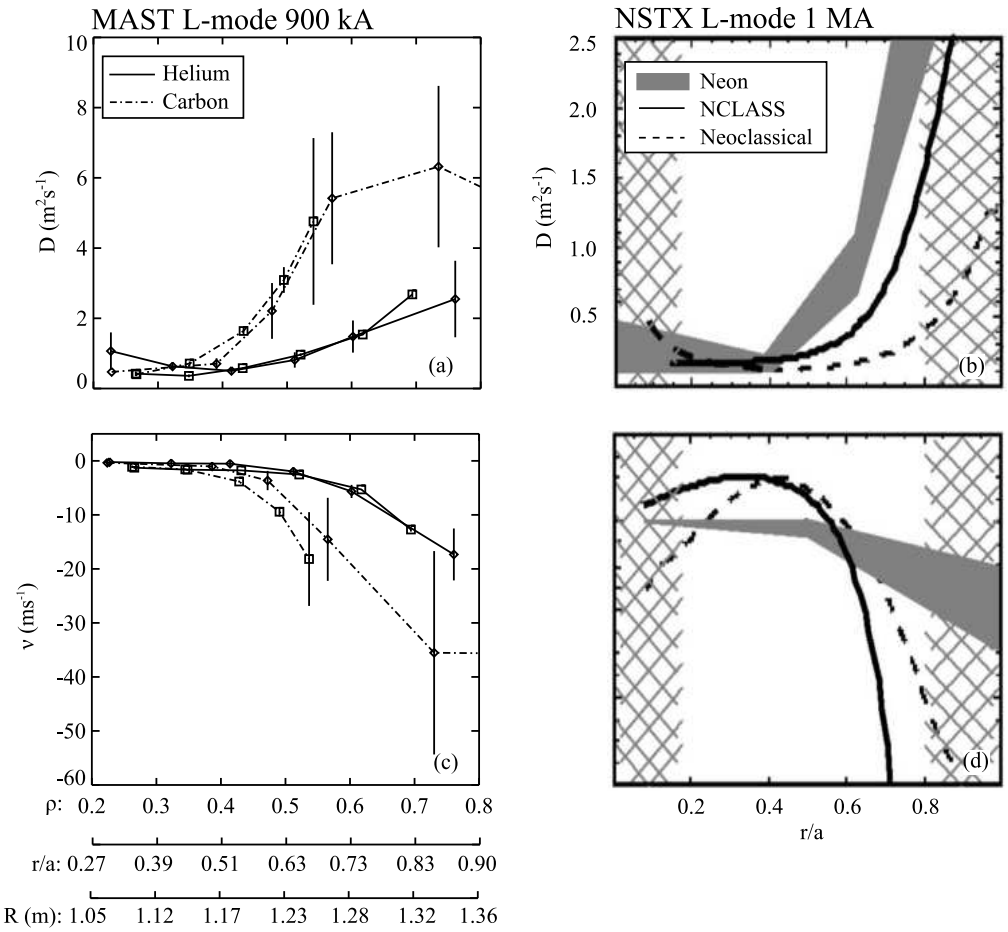

Figure 5.5: On the left, the D_i (top) and v_i (bottom) coefficients for helium and carbon, determined using the UTC-SANCO (diamonds) and FG (squares) method in the L-mode 900 kA plasma, are illustrated as a function of R, r/a and ρ. On the right, the experimental Ne transport coefficients (grey shaded region) taken from a study on NSTX [41] during an L-mode 1 MA plasma, are illustrated as a function of r/a.

and 5.5c respectively for helium and carbon. Over the range where the sources are negligible, the two methods agree within error bars for both D_i and v_i giving confidence in the methods evaluation of the transport coefficients. In the inner region of the plasma ($\rho < 0.4$), helium and carbon both experience low transport with $D_i \sim 0.5$ m^{2}s^{-1} and $v_i \sim -1$ ms^{-1}. Outside this radius ($\rho \geq 0.4$), the transport of both impurities increase with radius. D_C and v_C increase up to ~ 6 m^{2}s^{-1} and ~ -30 ms^{-1} respectively, while D_{He} and v_{He} increase to values of ~ 2 m^{2}s^{-1} and ~ -15 ms^{-1} respectively.

Similar plasma conditions on NSTX (L-mode, I_p =1 MA and B_T =0.45 T) have been studied with neon [41]. D_{Ne} and v_{Ne} coefficients from this study are shown in figures 5.5b and 5.5d respectively. Note that this graph is given as a function of r/a, not ρ. A scale matching R and r/a to ρ is shown at the bottom of figure 5.5c to aid comparison between the radial grids. The region of low transport found for both impurities in the plasma core ($\rho < 0.4$) in the present work seems to be consistent with the NSTX neon transport results. At mid-radius, the rapid increase

in D_i found in the present analysis is also found for D_{Ne}. Somewhat higher rates of v_C are found compared to v_{Ne}, although the magnitude of v_{Ne} near the plasma edge is not given in their results.

From these comparisons, it can be concluded that the magnitude of D_i and v_i increases with z in the outer region of the plasma ($\rho > 0.4$). For the inner core of the plasma, no obvious trend with z is found.

5.4 Current Scan

For the low I_p plasma, it was shown in section 4.5.1 that the methane gas puff did not significantly perturb the background n_{C6+} concentration, therefore transport analysis is only carried out for n_{He2+}. Comparisons of the fitted and experimental n_{He2+} are shown in figure 5.6. A rise in n_{He2+} can be seen over the entire plasma cross-section, however the MHD activity 80 ms after the gas puff ($t > 0.27$ s) rapidly ejects the He^{2+} ions towards the plasma edge and therefore the time window is limited to 80 ms.

The fits produced with the FG and UTC-SANCO methods are shown in figure 5.7. Similar to the previous scenario, the FG linear fits show a clear change in transport, in space but not time, and the evolution of n_{He2+} has been reproduced by SANCO within error bars. Identical edge model parameters to those for the L-mode high I_p plasma are used in SANCO, as shown in table 5.1. The D_{He} and v_{He} coefficients are shown in figures 5.8a and 5.8c respectively. Both the FG and UTC-SANCO methods show agreement within error bars for $\rho < 0.6$. The D_{He} and v_{He} for the high I_p plasma are over-plotted in both graphs to aid the comparison. Decreasing I_p causes an increase in D_{He} within $\rho < 0.5$. There is also a suggestion that D_{He} increases nearer the plasma edge at low I_p, but the large error bars qualify the certainty of this conclusion. v_{He} follows the same trend as found in the high I_p plasma, where the large inward pinch near the plasma edge reduces almost to zero in the core. Decreasing I_p causes a small increase in the magnitude of v_{He}.

These results suggest that reducing I_p in L-mode acts to increase the magnitude of both D_{He} and v_{He}. This is a result that has also been inferred from argon transport measurements made during a four point I_p scan in L-mode plasmas on C-mod [30]. The D_{Ar} and v_{Ar} coefficients for the latter study are shown in figures 5.8b and 5.8d respectively. For the C-Mod study, B_T was kept constant at ~ 8 T

Table 5.1: SANCO edge coefficients for each plasma [L-mode high I_p, low I_p, H-mode]

	Helium	Carbon
$\tau_{\|\|}$ (ms)	[3, 3, 3]	[2, / , /]
R_{rcy}	[1.0, 1.0, 1.0]	[0.10, / , /]
ϵ_F	[1.0, 1.0, 1.0]	[0.04, / , /]
E_{th} (eV)	[2, 2, 2]	[2, / , /]

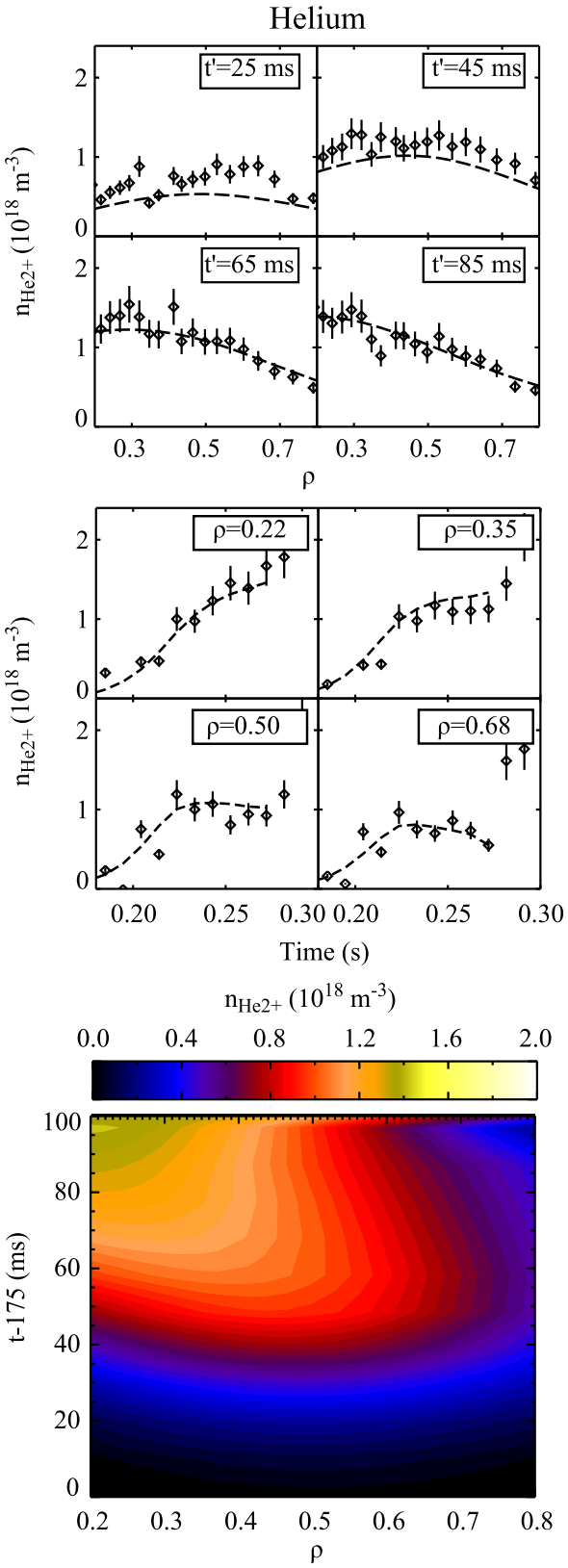

Figure 5.6: A comparison of the fitted and experimental n_{He2+} profiles for the low I_p plasma as a function ρ (top), t (middle) and ρ and t (bottom).

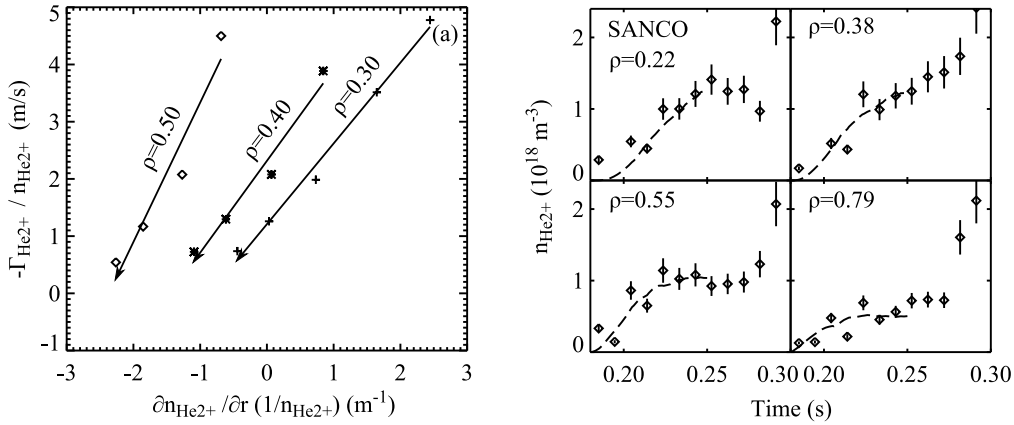

Figure 5.7: This figure shows an example of the fitting procedures required to determine the helium transport coefficients for the low I_p plasma. The left graph shows the linear fits (solid lines) made for the FG method at three different values of ρ, while the four graphs on the right compare the simulated SANCO n_{He2+} (dashed) with the experimental n_{He2+} profiles.

to vary the q profile, however the temperature profiles were not matched in each plasma. An increase in D_{Ar} is observed from mid-radius towards the plasma edge (r/a>0.3) as I_p is decreased. In this same radial region, the inward v_{Ar} increases in magnitude as I_p is decreased. Although these trends show striking similarities to the helium transport on MAST, it cannot be concluded unambiguously that the same underlying transport mechanisms are responsible for the trends in each study.

5.5 Confinement Mode Scan

The largest difference between the L-mode and ELMy H-mode plasmas occurs in n_e in the region $0.5 \leq \rho \leq 0.9$. For the H-mode plasma, the n_e profile is hollow in this range compared to the steep gradient in L-mode. Only helium transport is evaluated because the methane gas puff failed to perturb the intrinsic n_{C6+}. Comparisons of the fitted and experimental n_{He2+} profile are illustrated in figure 5.9. The fit is limited to the region $0.4 \leq \rho \leq 0.8$ because of the onset of significant MHD activity 60 ms after the gas puff.

Figure 5.7 shows the FG and UTC-SANCO fits respectively. The FG linear fits show a clear change in transport in space but not time and the evolution of n_{He2+} has been reproduced by SANCO within error bars. The experimental n_{He2+} profile has been produced by UTC-SANCO using the same edge parameters as the L-mode case. The D_{He} and v_{He} coefficients are shown in figures 5.11a and 5.11c respectively, with the results from the L-mode plasma also plotted for comparison. Within $0.4 \leq \rho \leq 0.7$ there is agreement within error bars between the FG and UTC-SANCO transport coefficients. The magnitude of D_{He} is marginally smaller near the edge of the H-mode plasma. There is a more obvious difference found in v_{He} between the two scenarios, with the inward pinch in L-mode becoming less significant in H-mode. In fact, v_{He} changes direction from inwards to outwards

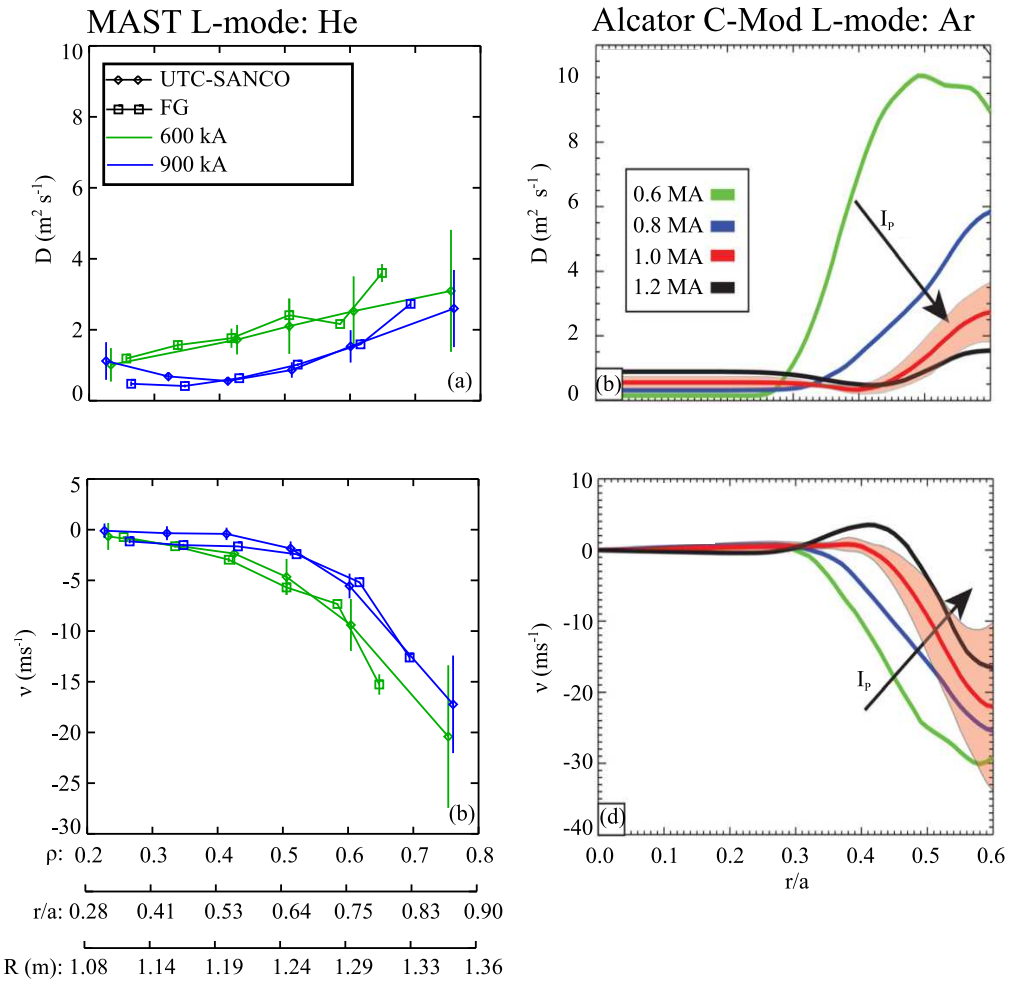

Figure 5.8: On the left, the D_{He} (top) and v_{He} (bottom) coefficients, determined using the UTC-SANCO (diamonds) and FG (squares) method in the 900 kA and 600 kA L-mode plasmas, are plotted as a function of R, r/a and ρ. On the right, the experimental Ar transport coefficients taken from a study on C-Mod [30] during an L-mode I_p scan are shown as a function of r/a.

within $\rho < 0.6$ in the H-mode plasma. This could explain why an out-flux of He^{2+} (and also C^{6+}) is observed in the intrinsic n_{He2+} and n_{C6+} profiles in figure 4.13.

A different study on NSTX determined neon transport coefficients in an ELMy H-mode plasma during an I_p scan at 1 MA and 1.2 MA [39]. In this case, B_T was varied between 0.45 T and 0.55 T meaning that q_{95} was kept constant. D_{Ne} and v_{Ne} coefficients from this study are shown in figures 5.11b and 5.11d respectively. It is more accurate to compare the results from the 1.2 MA H-mode plasma since the n_i gradient becomes positive at mid-radius in the NSTX study; a phenomenon also observed in the MAST H-mode plasma. A region of positive v_i coincides with this region of positive n_i gradient in both studies. The comparison between the 1 MA H-mode NSTX discharge in figures 5.11b and 5.11d and the 1 MA NSTX L-mode discharge shown in figures 5.5b and 5.5d also shows a small difference in D_{Ne}. On the other hand, there is also only a very small difference between v_{Ne} in both cases at 1 MA. But, a change in the direction of v_{Ne} is found in the NSTX study when

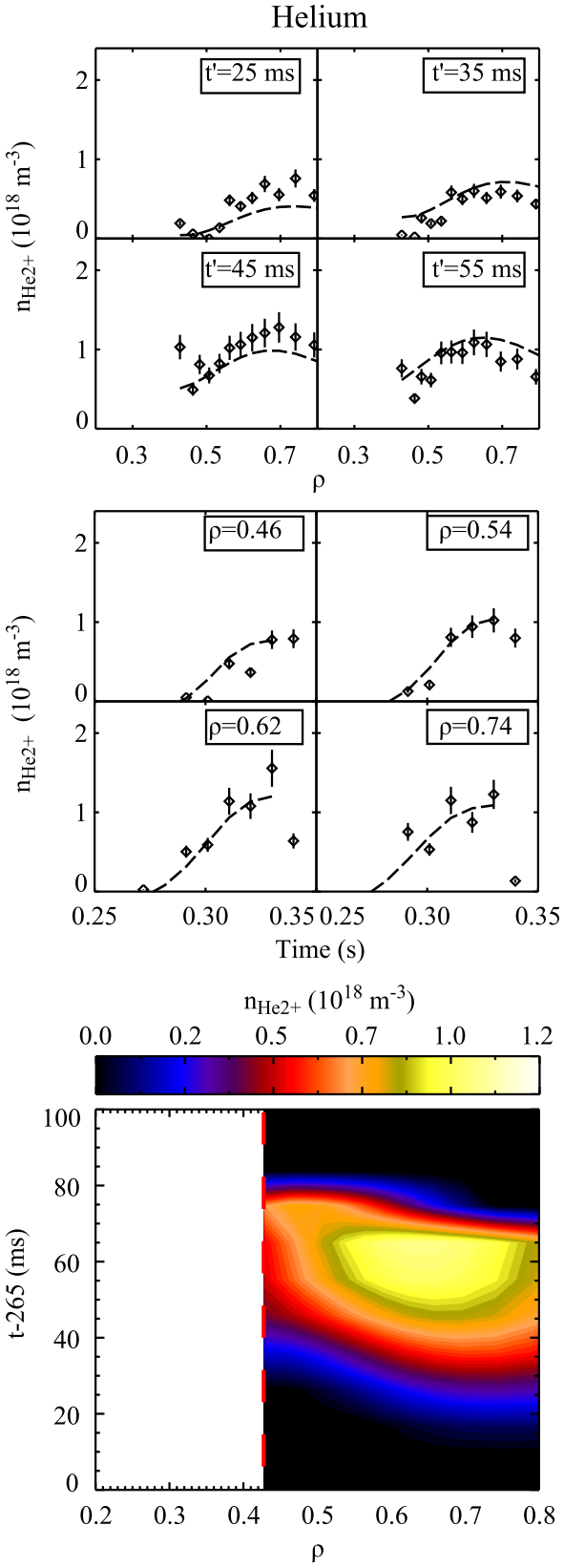

Figure 5.9: A comparison of the fitted and experimental n_{He2+} profiles for the H-mode plasma as a function ρ (top), t (middle) and ρ and t (bottom).

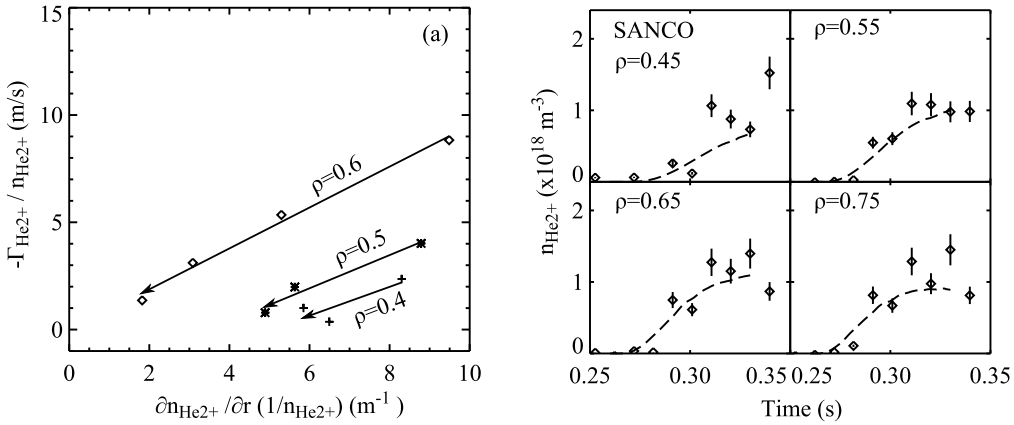

Figure 5.10: This figure shows an example of the fitting procedure required to determine the helium transport coefficients for the H-mode plasma. The left graph shows the linear fits (solid lines) made for the FG method at three different values of ρ, while the four graphs on the right compare the simulated SANCO n_{He2+} (dashed lines) with the experimental n_{He2+} profiles.

I_p is increased to 1.2 MA. It is unclear from the published NSTX results how v_{Ne} behaves at 1.2 MA in L-mode.

In summary, the results suggest that D_{He} remains approximately constant in L-mode and ELMy H-mode plasmas, but the inward pinch found in L-mode is smaller than in H-mode plasmas. It is noted that a study on DIII-D also found only a small difference between D_{He} in L-mode and ELMy H-mode, however a large decrease in D_{He} was found in ELM-free H-mode [57].

5.6 Extrapolation to ITER

The ratio of the τ_E and the effective helium confinement time, $\tau*_{He}$, must exceed a critical value, generally of the order of 0.1 [20]. This ratio is often defined as η and is expressed in equation 5.13, where τ^0_{He} and τ^{edge}_{He} are the confinement times of helium within the core and edge plasma respectively.

$$\eta \equiv \frac{\tau_E}{\tau*_{He}} = \tau_E \left(\tau^0_{He} + \tau^{edge}_{He} \frac{R_{rcy}}{(1 - R_{rcy})} \right)^{-1} > \eta_{crit} \tag{5.13}$$

The first term in brackets on the RHS of equation 5.13 shows that the transport of helium from the plasma core to the plasma edge must occur on a time scale faster than its production rate. The second term in brackets on the RHS of equation 5.13 shows that, even if the transport from the plasma core to the plasma edge is rapid, an inefficient pumping rate or low edge transport could still lead to the build up of helium within the plasma core.

It is not realistic to calculate $\tau*_{He}$ in this thesis because the high helium recycling rate in MAST would make the second term in brackets on the RHS of equation 5.13 unphysically large compared to a machine like ITER, which is envisaged to operate

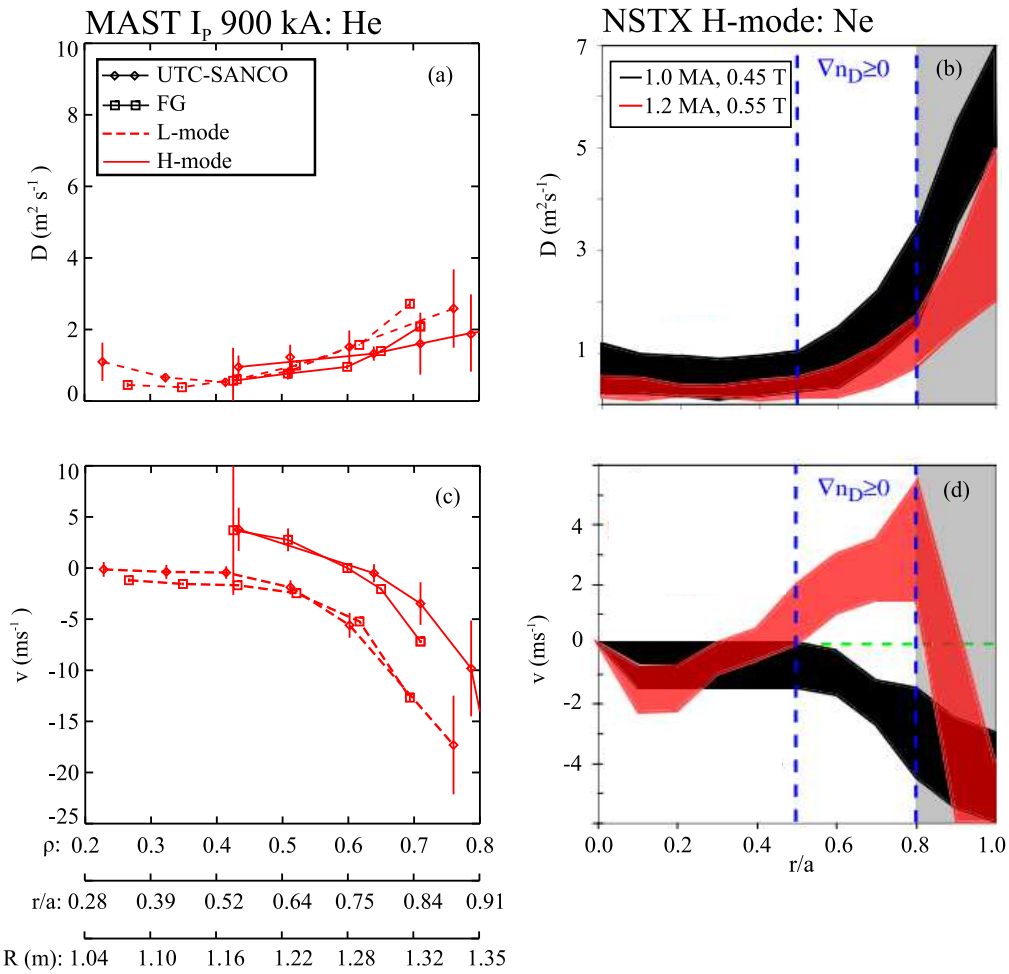

Figure 5.11: On the left, the D_{He} (top) and v_{He} (bottom) coefficients, determined using the UTC-SANCO (diamonds) and FG (squares) method in the L-mode and H-mode plasmas, are plotted as a function of R, r/a and ρ. On the right, experimental Ne transport coefficients from an H-mode I_p scan on NSTX [39] are shown as a function of r/a. This figure does not show the equivalent L-mode results for the NSTX study.

with enhanced helium pumping. Furthermore, a lack of reliable transport coefficients for the plasma edge mean that the predicted τ_{He}^{edge} will have a relatively high degree of uncertainty. Results from this thesis can however be used to examine τ_{He}^{0} by using the relation [107]

$$\frac{\tau_{He}^{0}}{\tau_E} = \frac{\chi_T^{eff}}{D_{He}} + P_V \tag{5.14}$$

where χ_T^{eff} is the total effective thermal diffusivity and P_V essentially plays the role of the zero flux profile peaking factor. Equation 5.14 shows that the amount of helium in the plasma core is directly related to the core helium transport coefficients. A reasonable estimate of P_V on MAST would suggest a value in the range of 0 and 10 based on the ratio v_i/D_i. It is expected that the transport in a CT like ITER will be predominantly driven by D_i, leading to relatively smaller values of C_V. Low-Z impurities generally experience a pinch of the order of the Ware pinch ($|v_i| < 4$ m/s) [58, 108].

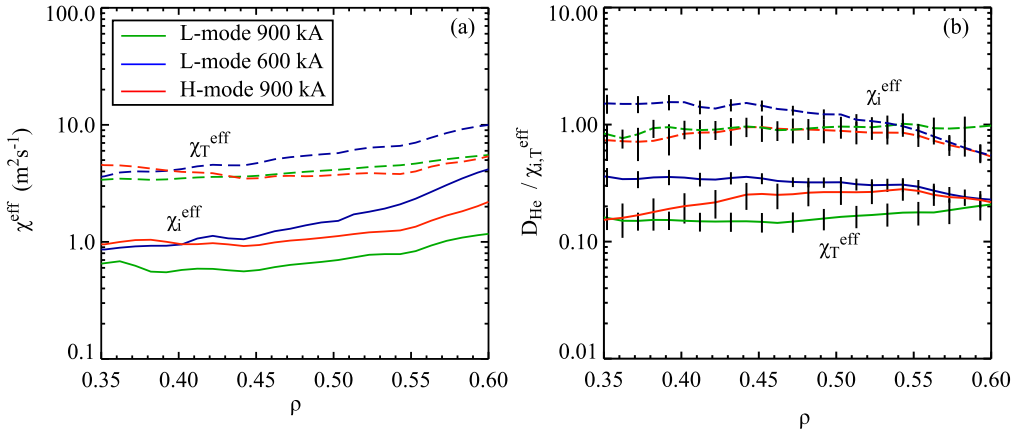

Figure 5.12: The magnitude of $\chi_{T,i}^{eff}$ is shown on the left for each plasma in the range where the T_e and T_i gradient is well defined. The ratio of $D_{He}/\chi_{T,i}$ is shown on the right in the same radial range.

The definition of χ_T^{eff} can be written as [87]

$$Q_e = -\chi_e^{eff} n_e \frac{\partial}{\partial r} T_e \tag{5.15}$$

$$Q_i = -\chi_i^{eff} n_i \frac{\partial}{\partial r} T_i \tag{5.16}$$

$$Q_e + Q_i = -\chi_T^{eff} \left(n_e \frac{\partial}{\partial r} T_e + n_i \frac{\partial}{\partial r} T_i \right) \tag{5.17}$$

where Q_e and Q_i are the electron and ion heat fluxes respectively. Generally, χ_T^{eff} is only analysed in the mid-radius region where the temperature gradients are well defined. For MAST, this range is $\rho \approx 0.35 - 0.6$. Radial $\chi_{e,i,T}$ profiles are calculated for each plasma using the predictive transport code JETTO [109, 110]. An input of the time-averaged experimental inputs of n_e, T_e, T_i and Z_{eff} mapped to a magnetic equilibrium are required by JETTO. Time averaged profiles of n_e, T_e and T_i are used for each scenario as shown previously in figure 4.3. A constant value of 1.2 is used over the plasma radius for Z_{eff}, which is a reasonable estimate based on the n_{He2+} and n_{C6+} profiles calculated in chapter 4.

$\chi_{T,i}^{eff}$ profiles and the $D_{He}/\chi_{T,i}^{eff}$ ratios are shown for each scenario in figures 5.12a and 5.12b respectively. For the range shown, χ_T^{eff} follows the same trend as D_{He} in each scenario with a magnitude ~ 4 times greater than D_{He}. The agreement in magnitude between χ_i^{eff} and D_{He} is far closer than χ_T^{eff} with $D_{He}/\chi_i^{eff} \sim 1$. On the other hand, χ_i^{eff} does not strictly follow the same trend as D_{He} in H-mode, as χ_i^{eff} increases in the H-mode plasma. This figure also shows that $\chi_e^{eff} > \chi_i^{eff}$, a result also found previous on MAST and NSTX [111, 112]. χ_i^{eff} is typically of the same order of magnitude as neoclassical predictions, whereas χ_e^{eff} is predominantly driven by turbulence [113].

A number of CT studies have tried to quantify D_{He}/χ^{eff}. Two helium gas puff studies on TFTR showed that values of D_{He} in the plasma core agree in magnitude

with χ_i^{eff}, but also found that $\chi_i^{eff} > \chi_e^{eff}$ [86,87]. Similarly on DIII-D, D_{He}/χ_i^{eff} is found close to unity [57]. Although these studies state that $D_{He}/\chi_T^{eff} \sim 1$, this is due to the fact that $\chi_i^{eff} > \chi_e^{eff}$. The ratio of $D_{He}/\chi_T^{eff} \sim 0.25$ found in this thesis has also been observed for the main gas species on JET [114]. A moderately larger ratio of $D_D/\chi_T^{eff} \sim 0.4$ was found on MAST [90]. This would indicate that the confinement time of helium is approximately equal to the confinement time of the main gas species. This is encouraging because it suggests that helium will be ejected from the core plasma in a time scale approximately equal to that of the main ion gas. If helium was confined for a longer period of time than the main gas, then this would lead to a build up in the overall concentration of helium.

For a larger D-T spherical tokamak, or even a next step device such as MAST-U where helium is still intrinsic from the HeGDC, the role of P_V must be taken into account when analysing the η ratio. Results from the present study indicate that the large inward pinch found in the L-mode plasmas could cause a large accumulation of helium in the plasma core. P_V is less significant in H-mode because the pinch is reduced and actually enhances the outward flux of impurities at mid-radius.

5.7 Summary

Two models, one using a predictive approach (UTC-SANCO) and one using an interpretative flux gradient approach (FG), have been used to determine the D_i and v_i coefficients for the plasma scenarios described in chapter 4. A code was developed to implement the FG model and benchmarked by reproducing the arbitrary transport coefficients used by SANCO to model a helium density profile. Each plasma scenario has a region of low transport within $\rho \leq 0.4$, which increases with radius towards the plasma edge. A correlation was found between the transport coefficients and each of the scanning parameters, consistent with other impurity transport studies carried out on NSTX and C-mod. These trends are summarised as follows: in the range of $\rho \geq 0.4$, the carbon transport was greater than the helium transport. A peak of ~ 3 m^{2}s^{-1} was found for D_{He}, while a peak of ~ 6 m^{2}s^{-1} was found for D_C. The convection was directed inwards for both impurities with a peak of -20 ms^{-1} for v_{He} and -35 ms^{-1} for v_C. No significant difference between $D_{He,C}$ and $v_{He,C}$ was found within $\rho < 0.4$. Reducing I_p caused an increase in D_{He} and $|v_{He}|$ in the range of $0.3 < \rho < 0.7$. Due to the large error bars of D_{He} and v_{He} near the plasma edge, it is unclear whether there is any correlation with I_p for $\rho \geq 0.8$. The results also suggest that there is no correlation of D_{He} and v_{He} with I_p within $\rho \leq 0.3$. For the confinement scan, the main difference in D_{He} occurs between $0.6 < \rho < 0.8$, where D_{He} is found to marginally decrease in the ELMy H-mode. A clearer correlation with the confinement mode is found for v_{He}. The absolute magnitude of the inward pinch found in L-mode is significantly reduced in H-mode for $\rho > 0.6$ and changes direction (from inwards to outwards) within the $\rho \leq 0.6$.

The ratio of $D_{He}/\chi^{eff}_{T,e,i}$ was discussed. It was found that χ_T closely followed the same trend as D_{He} throughout the parameter scans, but produced a ratio of $D_{He}/\chi^{eff}_T \sim 0.25$. On the other hand, χ^{eff}_i was more closely matched in magnitude to D_{He}, with $D_{He}/\chi^{eff}_e = 0.5 - 1.5$. χ^{eff}_i followed the same trend as D_{He} for the I_p scan in the L-mode plasma, but the opposite trend was found during the confinement mode scan at constant I_p. The next chapter will compare these experimental findings with neoclassical and gyrokinetic simulations.

Chapter 6

Theoretical Transport Modelling

6.1 Introduction

The ultimate goal of any transport theory is to derive an expression for the particle flux. Radial transport in magnetically confined toroidal plasma can either originate from Coulomb collisions, or from the effects of short-range fluctuations in the plasma parameters. The study of the particle flux generated by Coulomb collisions in a cylindrical geometry forms the basis of classical transport. In this model, it is not practical to treat each particle separately; rather averages over larger distributions of particles are handled using macroscopic fluid equations [115]. It can readily be shown that the moments of the Vlasov equation, with a Fokker-Plank collision operator (Vlasov-FP), yield expressions for the conservation of particles (zeroth moment), momentum (first moment), and energy (second moment) [116]. The classical particle flux due to collisions is determined by analysing the momentum balance equation. Tokamaks operate with a toroidal plasma geometry, which causes a geometrical enhancement of the transport coefficients. To distinguish between the physics of the classical cylindrical plasma geometry and the toroidal plasma geometry found in tokamaks, the term 'neoclassical transport' is used.

In tokamaks, the actual impurity flux usually exceeds the neoclassical predictions. The additional transport is referred to in literature as 'anomalous transport'. Neoclassical predictions assume that the plasma parameters are stationary but plasmas are rarely quiescent as fluctuations in the plasma parameters arise spontaneously. Plasma turbulence is the result of non-linear interaction between small scale parameter fluctuations of the order of the ion Larmor radius, ρ_i, which are driven unstable mainly by the plasma currents and the spatial gradients in temperature and density. These types of instability are called microinstabilities and the study of plasma behaviour on spatial scales comparable to the gyroradius is the subject of gyrokinetic theory. Microinstabilities are generally thought to cause the anomalous transport found in CTs [117], although an important feature of the ST is

that the equilibrium flow shear, driven by the strong toroidal rotation, is predicted to stabilise the turbulence in both L-mode and H-mode plasmas [12].

Linear gyrokinetic simulations yield the properties of the most unstable microinstabilities. Strictly, more demanding non-linear gyrokinetic simulations are required to predict the properties of the saturated turbulence. A quasilinear approach is used in the present analysis, exploiting the properties of the dominant linear modes to model the saturated turbulence. This chapter summarises the neoclassical and gyrokinetic models and compares the diffusion and convection coefficients inferred from the transport models with the results deduced from CXS.

6.2 Neoclassical Transport

The classical transport model analyses the radial particle flux induced by collisions in the simplest confined plasma; a straight cylindrical plasma with a uniform magnetic field. In this simplest form, the plasma can be described by Braginskii's fluid-like equations [115]. Consider a fluid species, a, with mass, m_a, number density, n_a, and charge, z_a, undergoing collisions with background fluid species denoted by b. The momentum balance equation, derived from the first moment of the Vlasov equation, can be written as (Helander and Sigmar equation 2.16 [116])

$$\mathbf{R}_a = n_a m_a \frac{d\mathbf{v}_a}{dt} + \nabla p_a + \nabla \cdot \pi_a - q_a n_a (\mathbf{E} + \mathbf{v_a} \times \mathbf{B}) \tag{6.1}$$

where $\mathbf{v}_a$ denotes the mean fluid velocity, p_a is the pressure, π_a is the viscosity tensor and $\mathbf{E}$ and $\mathbf{B}$ are the average electric and magnetic fields respectively. $\frac{d}{dt} = \left(\frac{\partial}{\partial t} + \mathbf{v}_a \cdot \nabla\right)$ is the convective derivative which describes the rate of change with respect to a moving coordinate system with the fluid element. $\mathbf{R}_a$ is the total force exerted on species a due to Coulomb collisions from the different species in the plasma, defined as $\mathbf{R}_a = \sum_b \mathbf{R}_{a,b}$.

Taking the vectorial product of equation 6.1 with $\mathbf{B}$ gives an expression for the perpendicular fluid velocity as

$$\mathbf{v}_{a\perp} = \frac{\mathbf{E} \times \mathbf{B}}{B^2} + \frac{1}{n_a m_a \Omega_{ac}} \mathbf{b} \times \left(\nabla p_a + \nabla \cdot \pi_a - \mathbf{R}_a + n_a m_a \frac{d\mathbf{v}_a}{dt} \right) \tag{6.2}$$

where $\Omega_{ac} = z_a B / m_a$ is the gyrofrequency and $\mathbf{b} = \mathbf{B}/B$ is the unit vector in the direction of the magnetic field. When the distribution of particles is close to a Maxwellian, the terms in equation 6.2 can be ordered in terms of their relative contribution. The leading order terms are

$$\mathbf{v}^0_{a\perp} = \frac{\mathbf{E} \times \mathbf{B}}{B^2} + \frac{\mathbf{b} \times \nabla p_a}{n_a m_a \Omega_{ac}} \tag{6.3}$$

where the first term on the RHS is known as the $\mathbf{E} \times \mathbf{B}$ drift and the second term is the diamagnetic drift which causes a drift of particles in the poloidal direction.

The reduction of equation 6.3 can be justified by the following considerations. If the fluid motion is constant in time ($\partial \mathbf{v}_a/\partial t = 0$) and space ($\mathbf{v}_a \cdot \nabla \mathbf{v}_a = 0$), then the convective derivative term is negligible. For a rapidly rotating plasma in toroidal geometry, the centrifugal force can create a significant fluid drift and therefore the convective term becomes significant. This point will be addressed in section 6.2.3. The viscosity term can be neglected if the gradient scale length of the macroscopic plasma parameters is greater than the collision mean free path. In a cylindrical plasma, this approximation is acceptable since the collisional mean free path is given by the Larmor radius, ρ_a, as shown in the next subsection (ρ_a is defined previously in equation 4.3), but in a toroidal plasma, this approximation does not always hold as the collisional mean free path is enhanced by the toroidal geometry. Lastly, when the gyrofrequency is larger than the collision frequency (see equation 6.7 below), then the perpendicular force can be neglected. The gyrofrequency is smaller for low B_T operation, as is typical in STs, since $\Omega_{ac} \propto B$ and therefore the collision force can become significant. It is this collisional force which is of interest for the present analysis.

6.2.1 The Role of Collisions

The fluid species a experiences a perpendicular collision force due to the combination of the friction force caused by the velocity difference with fluid species b, denoted by $\mathbf{R}^{Fr}_{a,b\perp}$, and the thermal force induced by the temperature gradient, denoted by $\mathbf{R}^{Th}_{a,b\perp}$. These terms are summarised as (Helander and Sigmar equations $4.37 - 4.38$ [116])

$$\mathbf{R}^{Fr}_{a,b\perp} = m_a n_a \nu_{a,b}(\mathbf{v}_{b\perp} - \mathbf{v}_{a\perp}) = \frac{n_a \nu_{a,b} k T_a}{\Omega_{ac}} \mathbf{b} \times \left(\frac{z_a T_b}{z_b T_a} \frac{\nabla p_b}{p_b} - \frac{\nabla p_a}{p_a} \right) \quad (6.4)$$

$$\mathbf{R}^{Th}_{a,b\perp} = \frac{3}{2} \frac{n_a \nu_{a,b}}{\Omega_{ac}} \mathbf{b} \times k \nabla T \quad (6.5)$$

so that

$$\mathbf{R}_{\mathbf{a}\perp} = -\sum_b \frac{n_a \nu_{a,b} k T_a}{\Omega_{ac}} \mathbf{b} \times \left(\frac{\nabla p_a}{p_a} - \frac{z_a T_b}{z_b T_a} \frac{\nabla p_b}{p_b} - \frac{3}{2} \frac{\nabla T_a}{T_a} \right) \quad (6.6)$$

The collision frequency, $\nu_{a,b}$, is defined as (Helander and Sigmar equation 1.4 [116])

$$\nu_{a,b} = \frac{4\sqrt{2\pi}}{3(4\pi\epsilon_0)^2} \frac{z_a^2 z_b^2 \ln \Lambda_{a,b}}{\sqrt{m_a}(kT)^{3/2}} n_b \quad (6.7)$$

where $\ln \Lambda_{a,b}$ is the Coulomb logarithm and k is the Boltzmann coefficient. The expression for $\mathbf{v}^0_{a\perp}$ in equation 6.3, is substituted into the initial definition of $\mathbf{R}^{Fr}_{a,b\perp}$ in equation 6.4 to give the final expression in equation 6.4. Note the $\mathbf{E} \times \mathbf{B}$ term in equation 6.3 is the same for all species and therefore cancels out in equation 6.4 and the perpendicular component $\mathbf{R}_{a\perp}$ is directed in the poloidal direction. Coulomb collisions obey the conservation of momentum, therefore $\sum_a \mathbf{R}_a = 0$.

The plasma ions experience friction with both electrons and impurities; collisions between like species cause a net zero friction force. The relative magnitude of the frictional forces from electrons and ions can be estimated by the expression (Helander and Sigmar equation 5.8 [116])

$$\frac{\mathbf{R}_{i,e}^{Fr}}{\mathbf{R}_{i,\mathrm{I},z}^{Fr}} \approx \frac{1}{\alpha}\sqrt{\frac{m_e}{m_i}} << 1 \tag{6.8}$$

where $\alpha = n_{\mathrm{I},z} z_{\mathrm{I}}^2 / n_i z_i^2$ is the impurity strength parameter. In the previous chapters, the subscript i has denoted all ions in the plasma, but for this chapter i is limited only to the primary ion species (i.e. D^+) and the subscripts I, z represents all the remaining z charged impurity ions in the plasma. The friction between the plasma ions and electrons is weak compared to the impurities. For a pure plasma, the plasma ion flux is constrained to the electron particle flux to conserve quasi-neutrality.

The perpendicular plasma ion particle flux is calculated from $\mathbf{\Gamma}_{i\perp} = n_i \mathbf{v}_{i\perp}$ (including the smaller terms of $\mathbf{v}_{i\perp}$ in equation 6.2). In cylindrical geometry, focus is only given to the part of $\mathbf{\Gamma}_{i\perp}$ induced by collisions. Since $\mathbf{R}_i = -\mathbf{R}_{\mathrm{I},z}$, the radial impurity particle flux is related to the plasma ion flux as $\mathbf{\Gamma}_{\mathrm{I},z} = -\frac{1}{z_{\mathrm{I}}}\mathbf{\Gamma}_i$. Making the assumption that $T_i = T_{\mathrm{I},z}$ and expressing the pressure gradient as $\nabla p_a = k(n_a \nabla T + T \nabla n_a)$ allows $\mathbf{\Gamma}_{\mathrm{I},z\perp}$ to be written in terms of the density and temperature gradients as

$$\begin{aligned} \mathbf{\Gamma}_{\mathrm{I},z\perp} &= \frac{1}{z_{\mathrm{I}}}\frac{\mathbf{b}\times\mathbf{R}_{i\perp}}{m_i\Omega_{ic}} \\ &= \frac{1}{z_{\mathrm{I}}^2}\frac{n_i \nu_{i,\mathrm{I},z} kT}{m_i \Omega_{ic}^2}\left(-\frac{\nabla n_{\mathrm{I},z}}{n_{\mathrm{I},z}} + z_{\mathrm{I}}\left(\frac{\nabla n_i}{n_i} - \left(\frac{1}{2}+\frac{1}{z_{\mathrm{I}}}\right)\frac{\nabla T}{T}\right)\right) \end{aligned} \tag{6.9}$$

Comparing equation 6.9 with equation 5.5 and using equation 6.7, the classical radial diffusion, $D_{\mathrm{I},z}^{\mathrm{CL}}$, and convection, $v_{\mathrm{I},z}^{\mathrm{CL}}$, coefficients can be defined as

$$D_{\mathrm{I},z}^{\mathrm{CL}} = \left(\frac{4\sqrt{2\pi m_i}}{3(4\pi\epsilon_0)^2}\right)\frac{\ln\Lambda_{i,\mathrm{I},z} n_i}{\sqrt{T}B_T^2} = 2.24\cdot 10^{-4}\ln\Lambda_{i,\mathrm{I},z}\frac{n_i}{\sqrt{T}B_T^2} \tag{6.10}$$

$$v_{\mathrm{I},z}^{\mathrm{CL}} = D_{\mathrm{I},z}^{\mathrm{CL}} z_{\mathrm{I}}\left(\frac{\partial \ln n_i}{\partial r} - \left(\frac{1}{2}+\frac{1}{z_{\mathrm{I}}}\right)\frac{\partial \ln T}{\partial r}\right) \tag{6.11}$$

T is in keV, n_i is in 10^{19} m^{-3}, B is in T and $D_{\mathrm{I},z}^{\mathrm{CL}}$ and $v_{\mathrm{I},z}^{\mathrm{CL}}$ are in m^2/s and m/s respectively.

Attention is drawn in equations 6.10 and 6.11 to the parameter dependencies. The diffusion can be described as a random walk process with $D \sim \Delta r^2/\Delta t$, using the mean free path $\Delta r \sim \rho_i$, and the collision time step, $\Delta t \sim \nu_{i,\mathrm{I},z}$. The $1/B^2$ dependence in equation 6.10 implies a significant difference in radial diffusion across the plasma in an ST, due to the anisotropic B_T. Also $D_{\mathrm{I},z}^{\mathrm{CL}}$ is independent of impurity charge. For $v_{\mathrm{I},z}^{\mathrm{CL}}$, a steep main ion density profile causes a particle pinch (inward convection), while a steep temperature gradient screens the particles from the core.

6.2.2 Toroidal Geometry

The classical particle flux is purely the result of perpendicular friction. In a toroidal system, the classical $\Gamma_{\mathrm{I},z\perp}$ is enhanced by parallel friction contributions resulting from various mechanisms, depending on the collisionality regime. The full derivation of the neoclassical terms is given in the overview by Hirshman and Sigmar [118]. Since the parameter dependencies of the neoclassical transport coefficients are relevant to this thesis, a brief description of the underlying transport processes is given, along with the key equations from Hirshman and Sigmar. These equations have also been summarised by Fussman et al. [119].

The collisionality, ν_*, defined as the ratio of the collision frequency and the guiding-centre transit frequency, Ω_t, (see equation 6.12 where v_{th} is the thermal velocity) identifies the different physical regimes involved in neoclassical transport.

$$\nu_* \equiv \frac{\nu}{\Omega_t} = \nu\frac{qR}{v_{th}} \sim \frac{d_{||}}{\Delta r}\begin{cases} >> 1 & \text{Pfirsch-Schlüter Regime} \\ << 1 & \text{Banana-Plateau Regime} \end{cases} \tag{6.12}$$

When $\nu_* >> 1$, the mean free path $\Delta r = v_{th}/\nu$ is shorter than the parallel distance around a flux surface $d_{||} \sim qR$ and the Braginskii fluid equations may still be used to analyse the transport. This collisionality regime is called the 'Pfirsch-Schlüter' (PS) regime. In the opposite limit, $\nu_* << 1$, referred to as the 'Banana-Plateau' (BP) regime, the fluid equations are no longer applicable and a kinetic description of the plasma must be used. For the plasma scenarios used in this thesis, it can be seen from figure 6.1 that D^+ and He^{2+} ions are within the BP regime over the entire plasma cross section, whereas C^{6+} ions lie between the PS and BP regime.

Pfirsch-Schlüter Regime

Consider first the C^{6+} ions in the PS regime near the edge of the plasma. In this regime, the parallel motion along a field line is purely diffusive, since the guiding-centre orbits are constantly interrupted by collisions. From the random walk picture, the parallel diffusivity can be estimated as $D_{||} \sim \Delta r^2\nu \sim v_{th}^2/\nu$, which allows the (diffusive) transit frequency to be expressed as

$$\Omega_t^{\mathrm{PS}} \sim D_{||}/(qR)^2 \sim \frac{1}{\nu}\left(\frac{v_{th}}{Rq}\right)^2 \tag{6.13}$$

As the fluid diffuses in the parallel direction, the vertical particle drifts, v_d, caused by the grad-B and curvature drift lead, to a random walk in the radial direction with a mean free path

$$\Delta r \sim \frac{v_d}{\Omega_t^{\mathrm{PS}}} \sim \frac{\rho_a v_{th}}{R}\frac{1}{\Omega_t^{\mathrm{PS}}} \tag{6.14}$$

The expression for v_d is obtained from Helander and Sigmar [116] equation 6.20. The random walk estimate for the perpendicular transport can be written using the

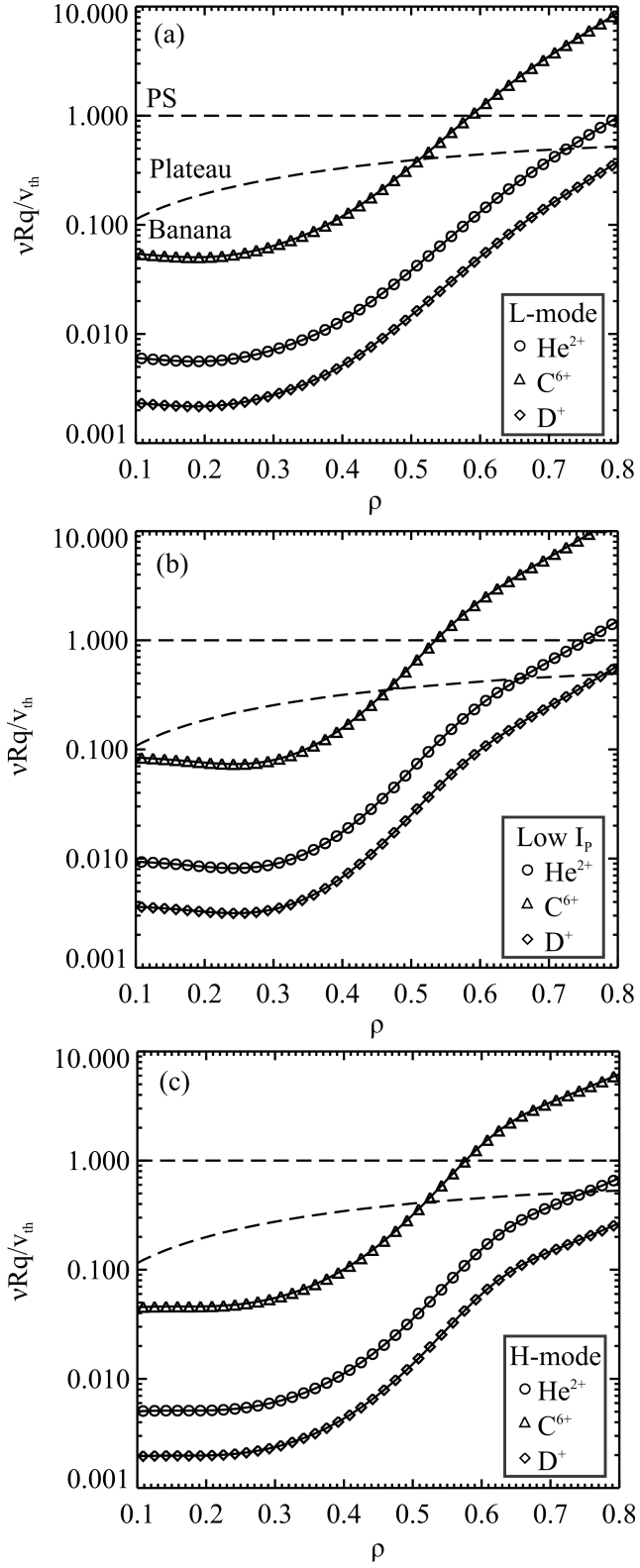

Figure 6.1: The variation of the effective collisionality and bounce frequency ratio with ρ for the D^+, He^{2+} and C^{6+} ions is shown for L-mode high I_p plasma (a), the low I_p plasma (b) and the H-mode plasma (c). Dashed lines represent the cut-offs for each neoclassical regime: Banana, Plateau and Pfirsch-Schlüter.

expressions in equations 6.13 and 6.14 as

$$D \sim \Delta r^2 \Omega_t^{\rm PS} \sim q^2 \rho_a^2 \nu \tag{6.15}$$

which is larger than the classical diffusion coefficient by a factor q^2.

This enhanced transport in the PS regime, over the classical value, is because the perpendicular diamagnetic current, $\mathbf{j}_\perp = \mathbf{b} \times \nabla P/B$, is not divergence free (i.e. $\nabla \cdot \mathbf{j}_\perp \neq 0$). The magnetic field strength varies radially across the plasma approximately as

$$B_T = \frac{B_0}{1 + (r/R_0)\cos\theta} \tag{6.16}$$

where B_0 is the field at R_0 and θ is the poloidal angle. The addition of a parallel current produces a divergence free total current and conserves quasi-neutrality (i.e. $\nabla \cdot (\mathbf{j}_\perp + \mathbf{j}_{||}) = 0$). It is shown in Helander and Sigmar (see equation 8.18 [116]) that this parallel current is the combination of a small PS current and a larger Ohmic current, the latter induced by the central solenoid, neutral beams or the so-called bootstrap-current. A small electric field is required to drive the parallel PS current against friction, which causes a radial $\mathbf{E}^{\rm PS} \times \mathbf{B}$ drift and therefore contributes to the radial particle flux. The full PS diffusion coefficients listed in equations 20 and 21 of Fussman et al. [119] are

$$D_{{\rm I},z}^{\rm PS} = 2Kq^2 D_{{\rm I},z}^{\rm CL} \tag{6.17}$$

$$v_{{\rm I},z}^{\rm PS} = D_{{\rm I},z}^{\rm PS} z_{\rm I} \left(\frac{\partial \ln n_i}{\partial r} + \frac{H}{K} \frac{\partial \ln T}{\partial r} \right) \tag{6.18}$$

where H and K are functions of the impurity strength parameter and the collisionality. The values of these two coefficients for a low collisionality case with low impurity concentrations are $H \sim -0.5$ and $K \sim 1$ as shown by Hirshman and Sigmar on page 1138 [118]. The PS transport is therefore similar to the classical case, except for the $\sim q^2$ enhancement of $D_{{\rm I},z}^{\rm CL}$.

Banana-Plateau Regime

The transport of the He^{2+} and C^{6+} ions in the BP regime is now considered. Recall that, in this regime, a kinetic description of the plasma must be used. When the particles travel along a field line from the point of lowest magnetic field, $B_T^{min} \propto (R_0 + r)^{-1}$, into the region of higher field, the mirror force acts to repel a certain fraction of particles back into the region of low magnetic field, as shown by the bold line in figure 6.2a. The fraction of reflected and unreflected particles are known as the 'trapped' and 'passing' particles respectively.

The fraction of trapped particles can be determined by noting that, when moving from one region of magnetic field to another, the kinetic energy, $W = \frac{m}{2}(v_\perp + v_{||})$, and magnetic moment, $\mu = W_\perp/B$, of the particles are conserved (in the absence of $\mathbf{E}$ fields) [1]. For trapping to occur, the magnetic field required to produce $v_{||} = 0$

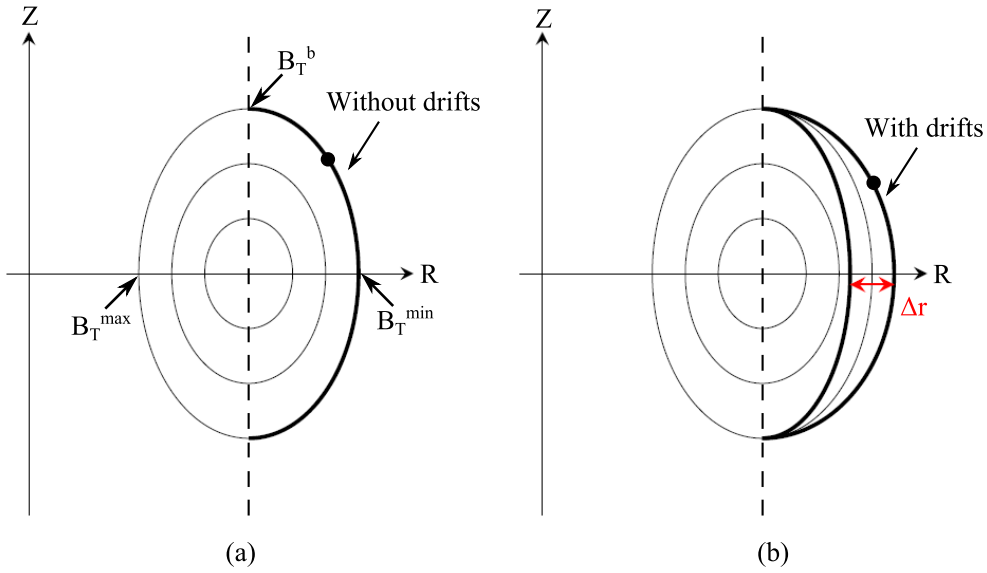

Figure 6.2: A poloidal cross section showing the magnetic flux surfaces and the trajectory of a trapped particle (shown in bold) without (a) and with (b) radial drifts included. The minimum and maximum magnetic field along the particle trajectory is denoted by B_T^{min} and B_T^{max} respectively, while the magnetic field at the bounce point, where $v_{||} = 0$, is denoted by B_T^b. The displacement distance of the particle due to the radial drifts is denoted in (b) by Δr.

must be less than B_T^{max} and therefore, from the constancy of μ, the requirement for trapping can be written as (see Wesson equation 3.11.3 [1])

$$\frac{v_{||0}}{v_{\perp 0}} \quad < \quad \left(\frac{B_T^{max}}{B_T^{min}} - 1\right)^{1/2} = \left(\frac{2\epsilon}{1-\epsilon}\right)^{1/2} \tag{6.19}$$

The 0 subscript denotes the speeds at the point where $B_T = B_T^{min}$ and ϵ denotes the inverse aspect ratio, r/R_0. If the particles have achieved a Maxwellian distribution, then using the expression in 6.19, the fraction of trapped particles can be written as (Wesson equation 3.11.5 [1])

$$f = \left(\frac{v_{||0}}{v_0}\right)_{crit} \quad = \quad \left(\frac{(v_{||0}/v_{\perp 0})^2}{1 + (v_{||0}/v_{\perp 0})^2}\right)^{1/2} \tag{6.20}$$

and therefore $f \propto \sqrt{\epsilon}$.

From the expression for $v_{||}$ in equation 6.19, the transit frequency for the trapped particles, often referred to as the bounce frequency, can be written as

$$\Omega_t^b \quad \approx \quad \frac{v_{th}\sqrt{2\epsilon}}{qR}. \tag{6.21}$$

Furthermore, the effective collision frequency in the Banana regime is given by $\nu_{eff} = \nu/\epsilon$. The trapped particle guiding-centre orbits therefore only exist for

$\nu_* << \epsilon^{3/2}$. In the collisionality space between the Banana and PS regimes, the trapped particle guiding-centre orbits are regularly interrupted, whereas the passing particle guiding-centre orbits are collisionless; this regime is known as the Plateau regime. The He^{2+} ions are well within the Banana regime, whereas the C^{6+} ions span all three regimes.

As the trapped particles traverse around their orbits, a radial drift is induced due to the vertical curvature and centrifugal effects, similar to the PS case. When incorporating these drifts into the trapped particle orbit, a so called 'banana orbit' is traced out in the poloidal plane, as shown in figure 6.2b. The radial distance travelled by the trapped particles, Δr, can be approximated by dividing v_d by Ω_t^b, as

$$\Delta r \approx \frac{\rho_a v_{th}}{R} \frac{Rq}{v_{th}\sqrt{\epsilon}} = \rho_a \frac{q}{\sqrt{\epsilon}} \tag{6.22}$$

The collision mean free path of the particles is now larger than the classical value (ρ_a) by a factor of $q/\sqrt{\epsilon}$.

Using the random walk estimation, with Δr and ν/ϵ, the Banana diffusivity coefficient is approximately $q^2/\epsilon^{3/2}$ times greater than $D_{\mathrm{I},z}^{\mathrm{CL}}$. The complete calculation of the particle flux in the Banana regime takes into account the parallel friction force induced by the viscosity anisotropy. Equation 27 and 28 from Fussman [119] give $D_{\mathrm{I},z}^{\mathrm{B}}$ and $v_{\mathrm{I},z}^{\mathrm{B}}$ in the Banana regime (explicitly for the He^{2+} ions) as

$$D_{\mathrm{I},z}^{\mathrm{B}} \approx 1.52 \cdot 10^{-23} \ln\Lambda \frac{n_i}{\sqrt{T}B^2} \frac{q^2}{\epsilon^{3/2}} \quad [\mathrm{m^2 s^{-1}}] \tag{6.23}$$

$$v_{\mathrm{I},z}^{\mathrm{B}} = 2D_{\mathrm{I},z}^{\mathrm{B}} \left(\frac{\partial \ln n_i}{\partial r} - 0.12 \frac{\partial \ln T}{\partial r} \right) \quad [\mathrm{ms^{-1}}] \tag{6.24}$$

where T is in keV, B in T and n_i in 10^{19} $\mathrm{m^{-3}}$. The convection is independent of impurity charge with a moderately reduced temperature screening.

The transport of C^{6+} ions in the Plateau regime is now briefly discussed. The effective collision frequency is defined as $\nu_* \equiv (v/v_{||})^2\nu$, since it is the small angle scattering which plays the important role in the Plateau regime. This means that the particle flux is essentially due to particles with $v_{||} \approx 0$. The fraction of particles in this regime is given by the ratio $f_p \sim v_{||}/v_{th}$ [116]. Furthermore, the particle flux is greatest when a resonance occurs between the effective collision frequency and Ω_t (Helander and Sigmar equation 10.5 [116]). A particle with this resonant velocity therefore drifts a radial distance, $\Delta r \sim v_d/\Omega_t \sim q\rho_a$, which allows the random walk estimate to be written as $D \sim f_p \Delta r^2 \Omega_t \sim q v_{th} \rho_a^2 / R$. Equations 25 and 26 from

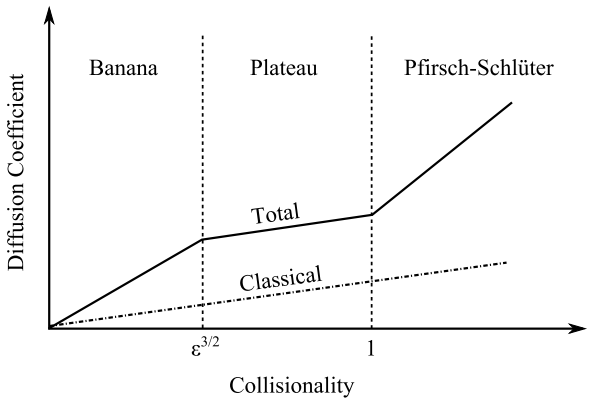

Figure 6.3: A cartoon of the total neoclassical diffusion coefficient as a function of collisionality (solid line), with the three distinct collisionality regimes, known as the Banana, Plateau and Pfirsch-Schlüter regimes, indicated by the vertical dashed lines. The classical contribution is also shown by the dashed-dot line.

Fussman [119] give $D^{\mathrm{P}}_{\mathrm{I},z}$ and $v^{\mathrm{P}}_{\mathrm{I},z}$ in the Plateau regime as

$$D^{\mathrm{P}}_{\mathrm{I},z} \approx 4.04 \frac{q}{R} \frac{\sqrt{A_{\mathrm{I},z}} T^{3/2}}{z^2_{\mathrm{I}} B^2} \quad [\mathrm{m^2 s^{-1}}] \tag{6.25}$$

$$v^{\mathrm{P}}_{\mathrm{I},z} = D^{\mathrm{P}}_{\mathrm{I},z} z_{\mathrm{I}} \left(\frac{\partial \ln n_i}{\partial r} + \frac{3(z_{\mathrm{I}} - 1)}{2 z_{\mathrm{I}}} \frac{\partial \ln T}{\partial r} \right) \quad [\mathrm{ms^{-1}}] \tag{6.26}$$

where T is in keV, $A_{\mathrm{I},z}$ is the unit mass and B in T. Note that $D^{\mathrm{P}}_{\mathrm{I},z}$ is now charge dependent and the temperature gradient now causes an inward pinch of impurities into the plasma.

The total radial particle flux is calculated by summing the radial fluxes in each regime $\Gamma^{\mathrm{T}}_a = \Gamma^{\mathrm{CL}}_a + \Gamma^{\mathrm{PS}}_a + \Gamma^{\mathrm{BP}}_a$. An illustration of the total diffusivity is shown by the schematic in figure 6.3. The definitions described above are only estimates because they describe a simplified transport regime with a high aspect ratio and a circular poloidal cross-section. MAST operates in a regime of high triangularity and elongation, meaning that the diffusion and convection coefficients must be multiplied by a geometrical factor related to the flux surface average; this factor has been shown to reduce the transport coefficients by up to a factor of two in D-shaped plasmas [120].

6.2.3 Neoclassical Simulations

The neoclassical transport properties of a multi-species axisymmetric plasma of arbitrary aspect ratio, geometry and collisionality is implemented in a FORTRAN module called NCLASS [35]. This code is integrated into the JETTO code suite described in section 5.6. However, in order to run NCLASS, JETTO requires the q profile as well as the T_e, T_i, n_e and Z_{eff} profiles. Values of n_i are calculated in an interpretative manner within JETTO using n_e and Z_{eff}. Helium and carbon are assumed as the only two impurities in the simulations.

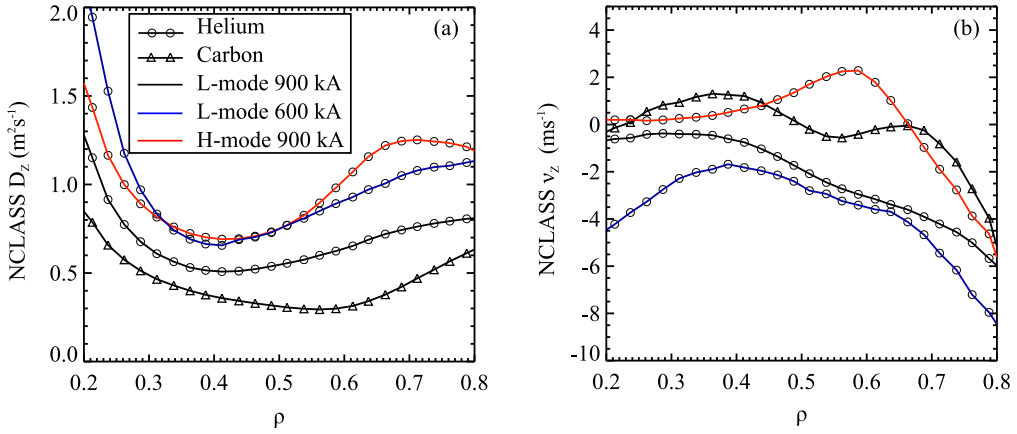

Figure 6.4: A comparison of the neoclassical transport coefficients, calculated using the NCLASS code, for the z scan between He^{2+} and C^{6+} in the L-mode, the I_p scan in L-mode and the confinement scan at constant I_p.

The neoclassical diffusion, $D^{\mathrm{NC}}_{\mathrm{I},z}$, and convection, $v^{\mathrm{NC}}_{\mathrm{I},z}$, coefficients, calculated by NCLASS for each plasma, are shown in figure 6.4 and demonstrate the neoclassical parameter trends. In general, $D^{\mathrm{NC}}_{\mathrm{I},z}$ is largest in the inner core and decreases rapidly until $\rho \sim 0.3$, where it then increases with radius towards the plasma edge. Increasing z, from $z = 2$ (helium) to $z = 6$ (carbon), acts to decrease the magnitude of $D^{\mathrm{NC}}_{\mathrm{I},z}$ and $v^{\mathrm{NC}}_{\mathrm{I},z}$ most significantly in the region of $0.4 < \rho < 0.8$, while a change of direction is found in v^{NC}_{C}, from inwards to outwards, within $\rho < 0.4$. Decreasing I_p in L-mode acts to increase moderately D^{NC}_{He} and v^{NC}_{He} by a factor of ~ 1.3. Moving from L-mode to H-mode causes an increase in D^{NC}_{He} mainly in the region $0.5 < \rho < 0.8$ and a decrease in the magnitude of v^{NC}_{He} in the region $\rho > 0.6$ as well as a change in direction in the region $0.4 < \rho \leq 0.6$.

The large rates of $D^{\mathrm{NC}}_{\mathrm{I},z}$ found within $\rho \leq 0.3$ are mainly due to the dependence of $D^{\mathrm{B}}_{\mathrm{I},z} \propto \epsilon^{-3/2}$, as shown in equation 6.23. An increase in the magnitude of D^{NC}_{C}, compared to D^{NC}_{He}, could be due to Plateau C^{6+} ions following equation 6.25, which is dependent on z^{-2}. The difference between v^{NC}_{He} and v^{NC}_{C} is most probably due to the dependence $v^{\mathrm{NC}}_{\mathrm{I},z} \propto z$ in all collisionality regimes. For $\rho < 0.5$, an increase in n_e at low I_p is observed experimentally which, from equation 6.23, could explain the increase in D^{NC}_{He} compared to the high I_p case. Towards the edge of the plasma, although n_e is marginally lower at low I_p, the larger values of q at low I_p will act to increase D^{NC}_{He}. The n_e profile is predominantly causing the difference in transport in the confinement scan since n_e increases near the plasma edge in H-mode compared to L-mode plasmas, which will increase $D^{\mathrm{NC}}_{\mathrm{I},z}$ and decrease $v^{\mathrm{NC}}_{\mathrm{I},z}$ due to the lower density gradient.

For the z scan, the trend of $D^{\mathrm{NC}}_{\mathrm{I},z}$ and $v^{\mathrm{NC}}_{\mathrm{I},z}$ is mainly in disagreement with the experimental findings. In figure 5.5, it is shown that $D_{\mathrm{I},z}$ and $v_{\mathrm{I},z}$ increase with z in the range $\rho > 0.4$. This increase therefore cannot be a neoclassical effect. The small increase in both D^{NC}_{He} and v^{NC}_{He} found at low I_p, compared to the high I_p plasma, is in reasonable agreement with the experimental trends shown in figure 5.8. The

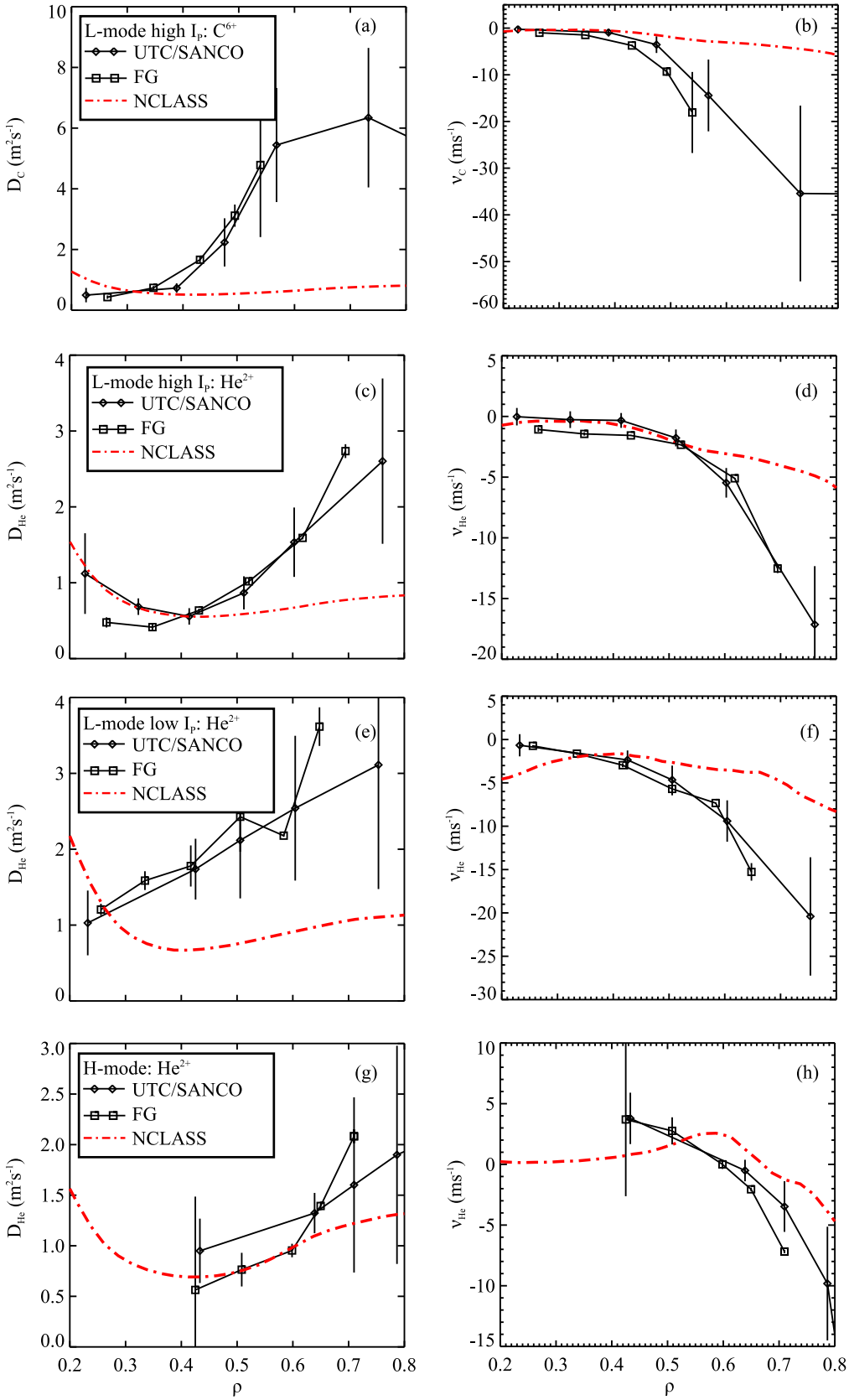

Figure 6.5: Comparisons of the radial neoclassical (red dashed line) and experimental (solid black lines) diffusion and convection coefficients, calculated in each plasma scenario, are shown on the left and right respectively.

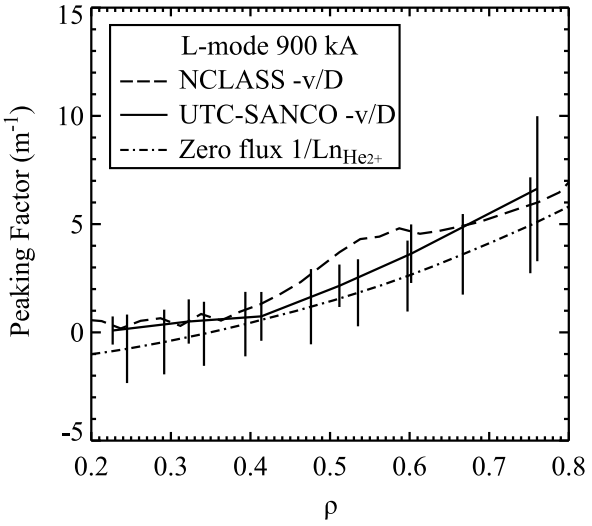

Figure 6.6: Peaking factor calculated using the D_{He} and v_{He} profiles from the UTC-SANCO analysis (solid line), the zero flux peaking factor from the plasma without a gas puff (dash-dot line) and the neoclassical D^{NC}_{He2+} and v^{NC}_{He2+} coefficients from NCLASS.

confinement scan does highlight a significant difference with the experimental trend in D_{He}, but agrees reasonably well for v_{He}, as shown in figure 5.11. Experimentally, moving from L-mode to H-mode causes a moderate decrease in D_{He}, whereas the neoclassical results would suggest the opposite.

So far the neoclassical and experimental parameter trends of the impurity transport have been compared. It is also necessary to evaluate whether the absolute magnitudes correspond to determine whether the impurity transport is responding predominantly to the neoclassical physics or to the background plasma turbulence. A comparison of the magnitudes of the transport coefficients for each scenario are illustrated in figure 6.5. For the L-mode high I_p plasma, the experimental $D_{He,C}$ and $v_{He,C}$ coefficients are both similar in magnitude to the neoclassical predictions within $\rho \leq 0.4$. Towards the edge of the plasma, the experimental $D_{He,C}$ and inward pinch are larger in magnitude than neoclassical predictions, more so for carbon than helium. At low I_p, the experimental values of D_{He} are higher than neoclassical predictions over the range $\rho > 0.3$, whereas v_{He} is larger in magnitude in the range $\rho > 0.4$. Therefore, it can be concluded that in both L-mode discharges (high and low I_p), the impurity transport is neoclassical up to $\rho = 0.4$, and the rates found between $0.4 < \rho < 0.8$ are anomalous. In the H-mode plasma, the picture is different and the neoclassical predictions, within the range $0.4 < \rho < 0.8$, agree within the error bars of the experimental results.

The helium zero flux peaking factor and the UTC-SANCO and neoclassical $-v_{He}/D_{He}$ ratio is shown for the L-mode 900 kA plasma in figure 6.6. There is good agreement between the $-v_{He}/D_{He}$ determined from UTC-SANCO and the zero flux peaking factor, which suggests the gas puff is not significantly changing the transport properties of the plasma. The UTC-SANCO and neoclassical $-v_{He}/D_{He}$ are very similar over the range of $0.2 \leq \rho \leq 0.8$. The behaviour is also similar for the L-mode

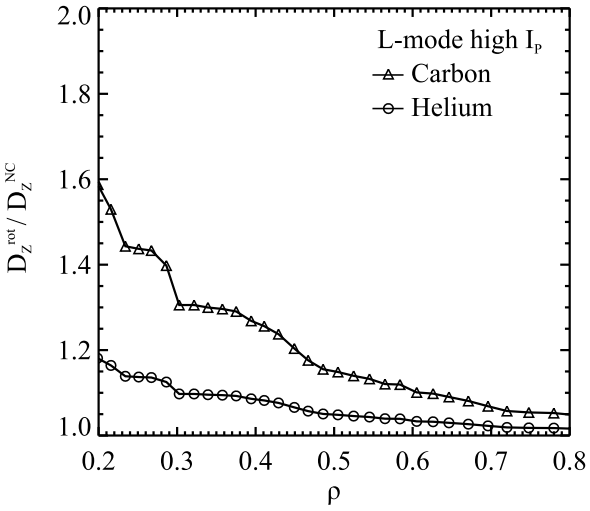

Figure 6.7: The magnitude of the approximate estimate of the radial neoclassical diffusion coefficient enhanced by rotation and value calculated by NCLASS is shown for carbon and helium during the L-mode high I_p plasma.

and H-mode plasmas. This shows that neoclassical theory can be used to predict where the impurities accumulate in the plasma after the impurity flux becomes zero. However the separate magnitudes of D_{He} and v_{He} suggest that neoclassical theory does not predict the time scales in which the impurities dynamically evolve near the plasma edge in L-mode. In other words, the peaking factor analysis would lead to the (incorrect) conclusion that the plasma is neoclassical over the entire plasma radius in L-mode, whereas the gas puff experiments show that anomalous transport is dominant near the L-mode plasma edge. This demonstrates one of the main motivations for carrying out gas puff experiments.

One limitation of NCLASS is that it does not include rotational effects. In a strongly rotating plasma, such as those generated in MAST, this limitation must be addressed. More specifically, one can no longer assume that $d/dt \approx 0$ in equation 6.2 since the Coriolis and centrifugal forces cause a significant perpendicular drift. The contribution of the rotation to the transport is summarised in equations 6.27−6.29 (Delgado-Aparicio equations 3−6 [121]):

$$D_{\mathrm{I},z}^{Rot} = D_{\mathrm{I},z}^{\mathrm{BP,PS}} \left(1 + \Gamma_{\mathrm{I},z}^{A} M_D^2 \frac{R_0^2}{R^2}\right)^2 \tag{6.27}$$

$$\Gamma_{\mathrm{I},z}^{A} = \frac{A_{\mathrm{I},z}}{2}\left(1 - \frac{2z_{\mathrm{I}}}{A_{\mathrm{I},z}}\left[\frac{T_e}{T_e + T_i}\right]\right) \tag{6.28}$$

$$M_D^2 = \frac{v_\phi^2}{v_{th}^2} \approx 1.05 \cdot 10^{-5} \frac{v_\phi^2}{T_i} \tag{6.29}$$

T_i is in keV and v_ϕ is in km/s. The ratio of $D_{\mathrm{I},z}^{rot}/D_{\mathrm{I},z}^{\mathrm{NC}}$ has been plotted as a function of ρ in figure 6.7 for the L-mode high I_p plasma. It can be seen that the correction from the rotation will act to increase the neoclassical rates for helium by ~ 20 % in the plasma core and by ~ 1 % near the plasma edge. This correction is amplified

for higher charge elements like carbon, where an increase of ~ 60 % is found in the plasma core and ~ 5 % in the plasma edge. This enhancement to $D_{\mathrm{I},z}^{\mathrm{NC}}$ decreases during the low I_p and H-mode plasmas and therefore has not been shown. The conclusions given previously from the NCLASS simulations stated that the transport is mainly anomalous in the region of $\rho > 0.4$ and the minor correction from the rotation does not change this conclusion.

6.3 Anomalous Transport

If the fluctuations in electrostatic potential, ϕ, and electromagnetic potential, $A_{||}$, are out of phase with the density fluctuations, then a radial flux is induced due to the net $\nabla\phi \times \mathbf{B}$ drift and the parallel motion along the perturbed field line. It is this fluctuation-driven radial flux that is thought to be responsible for the anomalous transport. The electrostatic potential fluctuations, ϕ, have a wave like character and are generally represented in Fourier form as

$$\phi = \sum_k f_k \exp\left(i[\mathbf{k}\cdot\mathbf{r}] - i\Omega_k t\right) \tag{6.30}$$

where each Fourier component has a unique wavenumber, $\mathbf{k}$, an associated complex frequency, $\Omega_k = \omega_k + i\gamma_k$, and an amplitude f_k. Gyrokinetic codes are typically used to show the growth-rate, $\gamma_k = \mathrm{Im}\left(\Omega_k\right)$, and real frequency, $\omega_k = \mathrm{Re}\left(\Omega_k\right)$, of the turbulent modes as a function of the wavenumbers parallel and perpendicular to $\mathbf{B}$, denoted as $k_{||}$ and $k_\perp$ respectively.

There are a number of different microinstabilities that can occur in tokamak plasmas [122]. The fundamental source of most instabilities is the temperature and density gradients. In CTs, the dominant electrostatic instabilities are the Ion Temperature Gradient (ITG) mode, the Trapped Electron Mode (TEM) and the Electron Temperature Gradient mode (ETG) [123]. The ITG instability, often called the η_i instability [124], rotates in the ion diamagnetic direction at long wavelength scales in the range of $k_\perp \rho_i < 1$, whereas the TEM and ETG rotate in the electron diamagnetic direction at medium wavelength scales ($1 < k_\perp \rho_L < \rho_i/\rho_e$) and short wavelength scales ($k_\perp \rho_i > 3$) respectively. When a particles gyroradius is much larger than the mode's correlation length, the effect of the mode is averaged out, hence ETG modes are not expected to affect significantly the ion motion and ITG modes are not expected to affect significantly the electron motion.

ITGs are destabilised when $\eta_i = d(\ln T_i)/d(\ln n) > 1$ [125]; therefore the ion temperature gradient drives the ITG unstable whereas the density gradient stabilises the ITGs. At low collisionality, the (collisionless) TEMs are driven primarily by the electron temperature gradient and/or the electron density gradient [126]. As the collisionality increases, the trapped particles become detrapped and hence the (dissipative) TEMs become stabilised [127, 128]. TEMs (and ETGs) are thought to

be responsible for the observed anomalous electron heat transport on MAST [12]. Electromagnetic effects must also be considered for high β tokamaks like MAST, as they can produce longer wavelength modes, such as tearing modes (TM) and Kinetic Ballooning Modes (KBM) [12, 129].

6.3.1 Microstability Analysis

To model γ_k and ω_k of the dominant microinstabilities, it is necessary to investigate the stability of a particular plasma equilibrium to small field perturbations of the form shown in equation 6.30. Gyrokinetic codes are used to study the evolution of ϕ, following an initial perturbation, by linearising the Vlasov equation in the following limits:

$$\frac{\omega_k}{\Omega_c} \approx \frac{C_a}{\Omega_c} \approx \frac{k_{||}}{k_\perp} \approx \frac{\rho_i}{L_p} << 1 \tag{6.31}$$

These orderings simply state that the gyromotion, Ω_c, is rapid compared to the fluctuating mode frequency, ω_k, and the model collision frequency, C_a. The instability is predominantly elongated in the parallel direction due to the rapid parallel motion of the particles and the pressure scale length is large compared to the Larmor radius.

Within the limits of equation 6.31, the kinetic equation can be averaged over the small and rapidly gyrating Larmor orbits to give the linearised electromagnetic gyrokinetic equation [12]:

$$\begin{aligned}\left[\frac{\partial}{\partial t} + (v_d + v_{||}\mathbf{b})\cdot\nabla + C_a\right] g_a \quad &= \left[z_a \tfrac{\partial f_{0a}}{\partial E}\tfrac{\partial}{\partial t} + \tfrac{1}{B}k_\perp \times \mathbf{b}\cdot\nabla f_{0a}\right] \\ &\times \left[\left(\phi - v_{||}A_{||}\right) J_0(d) + \tfrac{v_\perp}{k_\perp} B_{||} J_1(d)\right]\end{aligned} \tag{6.32}$$

where g_a is the perturbed distribution function for species a, f_{0a} is the Maxwellian particle distribution function, C_a is the model collision operator and E is the particle kinetic energy per unit mass. The perpendicular drift velocity term, v_d, contains the drifts due to the inhomogeneous magnetic field, such as the grad-B and curvature drift, the $\mathbf{E}\times\mathbf{B}$ drift, and the inertial drifts due to the Coriolis and centrifugal force. The parallel motion along the unperturbed field is contained in $v_{||}\mathbf{b}$. Lastly, the terms J_0 and J_1 are first and second Bessel functions representing the gyroaverage of the perturbations with argument $d = k_\perp \rho_i$.

Two local flux-tube electromagnetic gyrokinetic codes, GS2 [36,37] and GKW [38], are used to solve the linear gyrokinetic equation to yield the properties of the unstable microinstabilities as a function of $k_y\rho_i$. Here, k_y is the in-magnetic-surface perpendicular wavenumber. The flux-tube codes follow the field lines around the plasma from the outboard mid-plane to the inboard mid-plane and assume that the densities and temperatures and their gradient scale lengths are constant during the simulation. A proper account of the transport should include the non-linear saturation of the modes, however non-linear gyrokinetic simulations demand large

computing resources and therefore only the linear gyrokinetic equation is analysed in this thesis. A quasilinear approach is adopted, where the properties of the dominant linear modes are used to model the saturated turbulence. Knowledge of γ allows an approximation for the thermal diffusivity, called the mixing length thermal diffusivity:

$$\chi^{mix} \approx \gamma / k_y^2 \tag{6.33}$$

The dominant modes are inferred in the wavelength region where χ^{mix} is maximised.

The flux surface $\rho = 0.7$ is analysed for each plasma, since this surface provides reliable experimental transport coefficients thought to be dominated by turbulence in the L-mode plasmas. The magnetic equilibrium in GS2 and GKW is set up using the Miller parameters described in chapter 2. The magnetic flux reconstruction in each plasma has been calculated using the EFIT++ code described in chapter 2, constrained by the MSE diagnostic pitch angle and the D_α emission. Profile information for both GS2 and GKW input files were extracted from TRANSP [130] analysis to ensure consistency of the data. TRANSP provides information for six different plasma species (e, D, H, C and fast H, D) but, to reduce the complexity of the simulation, only electrons and (bulk) plasma ions were considered. Therefore the pressure profile and density of the plasma ions were modified to match the electron pressure profile density with Z_{eff} forced to unity in the input file.

Table 6.1 lists the relevant plasma equilibrium parameters of each plasma at $\rho = 0.7$, normalised by the sound speed, $c_s = \sqrt{T_i/m_i}$, and the minor radius, a. These parameters include the safety factor, q, the magnetic shear, $\hat{s} = (r/q)\mathrm{d}q\mathrm{d}r$, electron collisionality, $\nu^* = \nu_e a/c_s$, plasma beta, β, plasma triangularity, δ, plasma elongation, κ, the normalised gradients a/L_{T_i}, a/L_{T_e}, a/L_{n_e} and a/L_{u_i}, and the equilibrium flow shear, $\gamma_E \propto u'/q$, where u' is the spatial gradient of the toroidal ion rotation velocity normalised by $-a/c_s$. The largest difference between the input values occur for the L- and H- mode plasmas where the H-mode plasma experiences a significant reduction in a/L_{n_e} as well as an increase in β. Only minor differences are found between the two L-mode plasmas at different I_p.

On a spherical tokamak like MAST, the stabilising perpendicular component of the sheared toroidal flow, induced by strong neutral beam heating, dominates over the destabilising parallel component, and is thought to stabilise the long wavelength ITG instabilities [12]. This can be written quantitatively in terms of the sheared flow stabilisation criterion $\gamma_E > \gamma_{max}$ [131], where γ_{max} is the maximum linear growth-rate. growth-rates of the dominant instabilities have been computed in the absence of sheared flow with both codes. Effective linear growth-rates that account for the stabilising influence of flow shear have been calculated with GS2 using the method described in [113]. In this method, firstly a pre-set amplification factor, f_{NL}, determines the amount by which the initial value of ϕ must grow by to be considered unstable. This amplification factor is chosen to represent the non-linear saturation level. An estimate of this value, based on previous literature

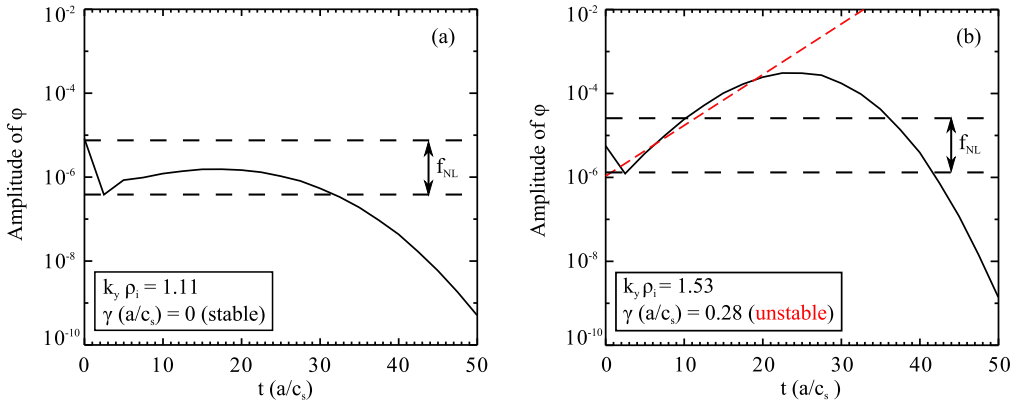

Figure 6.8: ϕ amplitude versus t in linear electromagnetic calculations for the $\rho = 0.7$ surface in the L-mode high I_p plasma for a stable and unstable mode, following the inclusion of flow shear, at (a) $k_y\rho_i = 1.11$ and (b) $k_y\rho_i = 1.53$. Horizontal grey lines indicate the amplitude range, denoted by f_{NL}, used to obtain the effective growth-rate γ. The red dashed line indicates the linear fit of the unstable mode in (b).

[113], suggests $f_{NL} = 100$, however a smaller value of $f_{NL} = 20$ seems to be needed in the simulations described above to preserve unstable linear modes at wavelengths greater than $k_y\rho_i > 1$. Once the mode has grown by this factor, any subsequent linear evolution of ϕ is disregarded. The effective growth-rate of the mode is then determined by fitting ϕ over the range of t that achieved the required mode amplification. An example of the temporal evolution of ϕ including the fitted function is illustrated at two different wavenumbers in figure 6.8 for the GS2 simulation of the L-mode high I_p plasma.

The parallel component of the sheared toroidal flow, as mentioned above, can act to destabilise certain modes due to the Coriolis drift and centrifugal force [132,133]. The derivation of the Coriolis drift [134] and centrifugal force [135,136] is included in GKW by writing the gyrokinetic equations in the co-moving frame [137]. GS2 also has the ability to include these terms, however the derivations have not been

Table 6.1: GS2 input parameters for $\rho = 0.7$

	L-mode high I_p	Low I_p	H-mode
c_s (m/s)	$1.3{\cdot}10^5$	$1.1{\cdot}10^5$	$1.6{\cdot}10^5$
a (m)	0.47	0.46	0.48
κ	1.48	1.37	1.45
$\sin^{-1}\delta$	0.20	0.21	0.21
β	0.006	0.004	0.020
q	2.00	2.40	2.21
$\hat{s}$	3.63	3.82	4.75
ν_e^*	1.45	2.18	1.89
a/L_{T_e}	7.42	6.70	4.74
a/L_{T_i}	4.30	4.01	4.31
a/L_{n_e}	1.89	2.09	0.06
u'	0.75	0.87	0.85
γ_E	0.18	0.19	0.09

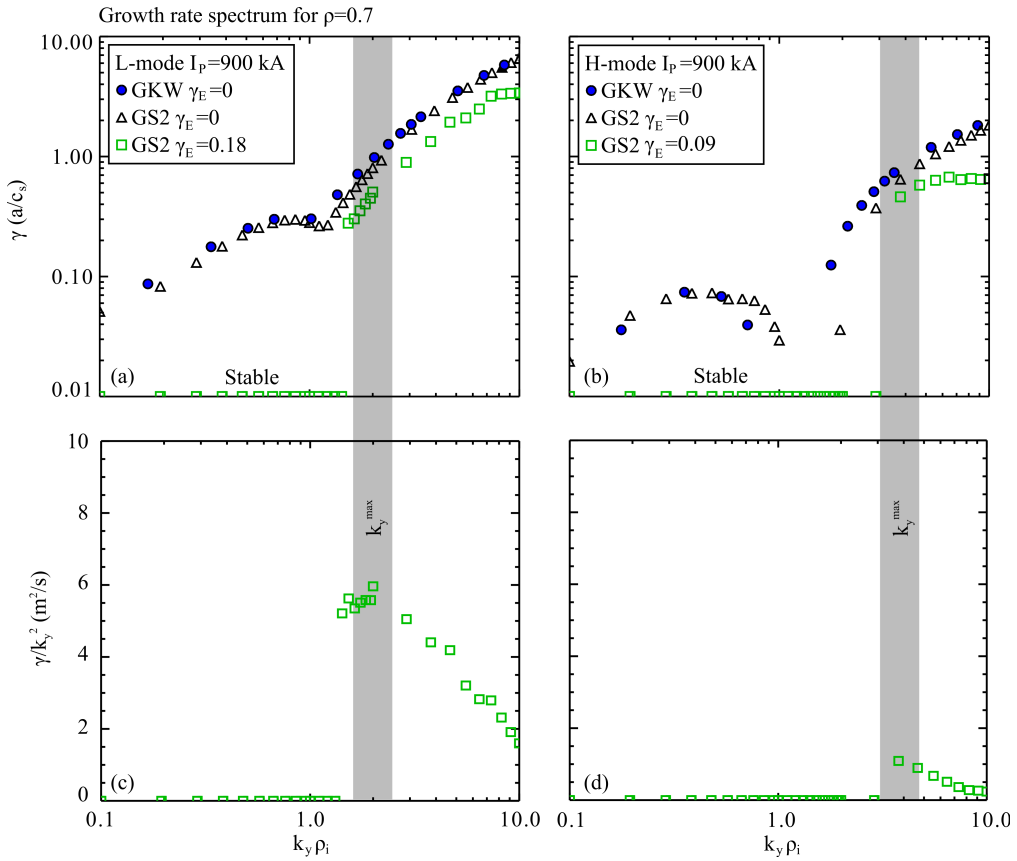

Figure 6.9: Linear growth-rate spectrum for the flux surface $\rho = 0.7$ in the L-mode (a) and H-mode (b) plasmas at high I_p. Calculations performed with and without flow shear using the GKW (circles) and GS2 (squares,triangles) codes respectively. The dashed lines represent the dominant linear mode in each case. Symbols along the x-axis represent the stable modes found. The mixing length estimates for the simulations with flow shear included is shown respectively for each case in (c) and (d).

benchmarked and therefore this feature is switched off in the GS2 input file.

The growth-rate spectrum from the microstability analysis of the L-mode and H-mode high I_p plasmas using GS2 and GKW are shown in figures 6.9a and 6.9b respectively for the range $0.1 < k_y\rho_i < 10$. Due to the similarity of input parameters for the low I_p and high I_p plasmas, the growth-rate spectrum for the low I_p plasma is not shown. For the L-mode high I_p plasma, both codes show unstable modes across the k_y spectrum with $\gamma_E = 0$. A similar growth-rate spectrum is observed in the H-mode plasma with $\gamma_E = 0$, however modes in the region $1 < k_y\rho_i < 2$ are stable. A similar stable region was reported for an earlier MAST H-mode discharge in [113]. The main difference between the local equilibria in L- and H-mode is that a/L_{n_e} is lower in H-mode. The sensitivity of TEM stability to the density gradient was also recently demonstrated in the microstability analysis of MAST discharges with pellet injection [138].

With γ_E set to the experimental value in the simulation, the plots in figures 6.9a and 6.9b suggest that unstable long wavelength ITG modes become stabilised in L- and H-mode at $\rho = 0.7$. The mixing length estimation, $\sim \gamma/k_y^2$, is shown in figures

6.9c and 6.9d with a maximum corresponding to $k_y\rho_i \sim 2$ and ~ 4 for L- and H-mode respectively. The BES electron density fluctuation signal, $\delta n_e/n_e$, averaged over 4 poloidal channels at each radius and time averaged over 2 ms ($\pm$ 1 ms either side of 0.24s), is plotted in figure 6.10a. The values of $k_y\rho_i$ observed by the BES diagnostic correspond to ITG turbulence. For $\rho = 0.7$, the electron density fluctuation signal is approximately 0.4 %, very close to the detection threshold. This suggests that ITG modes are indeed stable for this flux surface, but does not prove or disprove the existence of TEMs. The BES measurements are consistent with ITG modes being stable on this equilibrium surface of the 900 kA L-mode discharge. Towards the edge of the plasma the BES signal increases indicating a rising amplitude of ITG turbulence. This could be explained by the fact that the equilibrium flow shear decreases with radius as shown in figure 6.10b.

Another point is that the carbon transport is larger than neoclassical predictions by a greater amount than the helium transport. This is possibly because the Larmor radius of a C^{6+} ion is smaller than a He^{2+} ion by an amount $\sqrt{m_{He}/m_C} \sim 0.6$. Carbon ions are therefore affected by shorter wavelength fluctuations than the helium ions. This is significant because the long wavelength modes are stabilised by the toroidal flow shear, leaving only the shorter wavelength modes.

6.3.2 Quasilinear Peaking Factor

Quasilinear theory is now exploited to analyse the helium particle flux from GKW in terms of the transport coefficients associated with the dominant modes. From gyrokinetic theory, the helium particle flux can be written, assuming that $T_{He2+} = T_i$ as (Angioni equation 4 [29])

$$\frac{a\Gamma^{\mathrm{GKW}}_{He2+}}{n_{He2+}} = D^{\mathrm{GKW}}_{He}\left(\frac{a}{L_{n_{He2+}}} + C_T\frac{a}{L_{T_i}} + C_u u' + C_p\right) \tag{6.34}$$

where a negative impurity flux again represents an inward motion of impurities. The multiplier outside the brackets on the RHS of equation 6.34 represents the diffusivity, which is mainly dominated by the $\mathbf{E}\times\mathbf{B}$ advection, while the combination of the latter three dimensionless terms represent the convection coefficient. The trace impurity transport thermodiffusive (C_T) [139,140], rotodiffusive (C_u) [132,133] and convective (C_p) [141] dimensionless coefficients are functions of the impurity mass, charge, temperature, and the growth-rate and real frequency of the background turbulence. The latter dependence means that the direction of each term is dependent mainly on the modes direction of rotation, which for TEMs and ITG are different in sign (TEM is negative and ITG is positive). Summarising figure 2 of Ref. [142] for the impurities, the C_T term, which scales as $1/z$, and the C_u term are directed inwards for TEMs and outwards for ITG modes, while the C_p term has a term proportional to the magnetic shear which is always inwards and a term proportional to $1/q^2$ which is outwards for TEMs and inwards for ITG modes.

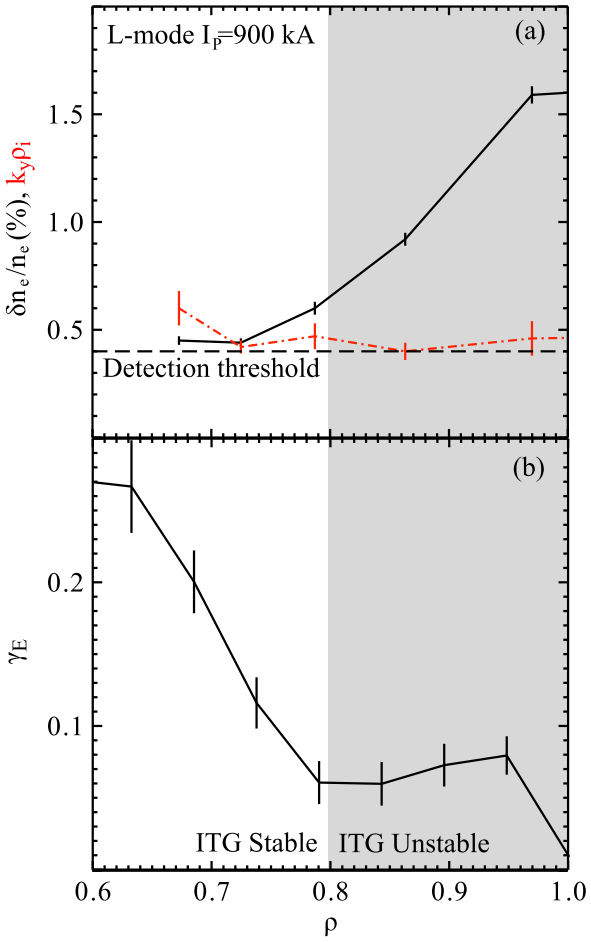

Figure 6.10: The BES electron density fluctuation signal with the corresponding $k_y\rho_i$ (dashed dot line) (a) and the time averaged equilibrium flow shear (b) are shown for the L-mode high I_p plasma.

Gyrokinetic simulations using GS2 and GKW, assuming $n_e = n_i$ and with helium set as a trace species (i.e. not affecting the background turbulence), can be used to determine quasilinear estimates of the particle flux described in equation 6.34. In this case, since the toroidal rotation may play a significant role in MAST plasmas, the particle flux will be investigated using GKW only in order to include the C_u term in equation 6.34. Since GKW simulations have not included the stabilising effect of the toroidal flow shear, the particle flux contribution from wavenumbers that are associated with stable modes found using GS2 after the inclusion of the sheared toroidal flow are shown but not considered in the discussion.

The dimensionless coefficients C_T, C_u and C_p are determined as a function of $k_y\rho_i$ using GKW by calculating the gyrokinetic particle flux of four trace amounts of helium with a pre-determined orthogonal set of equilibrium gradients [31]. This is demonstrated more clearly in table 6.2. Figure 6.11a illustrates the direction and relative magnitude of each term as a function of $k_y\rho_i$ for the unstable and stable modes in the L-mode high I_p plasma at $\rho = 0.7$. Note that, in this graph, the negative value of the transport coefficients are shown and therefore a positive value

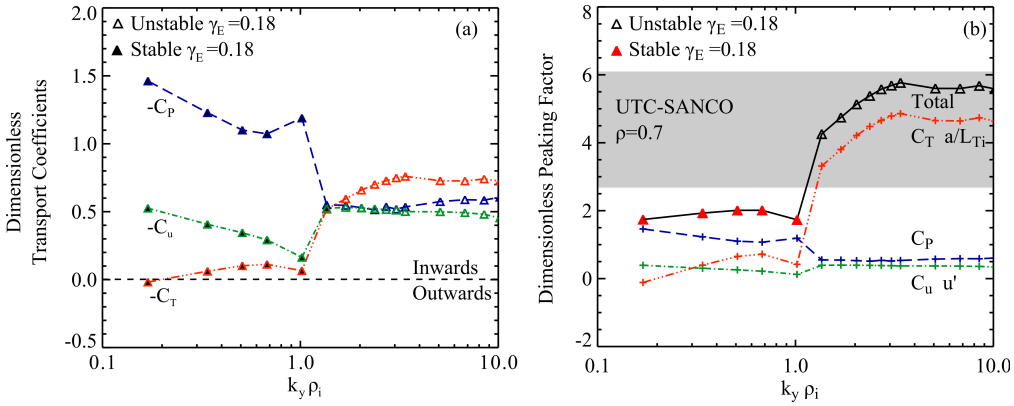

Figure 6.11: Gyrokinetic analysis of (a) the dimensionless transport coefficients and (b) the peaking factor are shown as a function of $k_y\rho_i$ for $\rho = 0.7$ during the L-mode high I_p plasma assuming $\gamma_E = 0$. Contributions from each transport coefficient are shown by the dashed lines (thermodiffusion in red, rotodiffusion in green and convection in blue) in (b). The shaded area corresponds to the error bars associated with the experimental value.

corresponds to an inward direction. This has been done because of the definition of the peaking factor, as will be discussed next. It can be seen from the graph in figure 6.11a that in the region of $k_y\rho_i \sim 2$, C_T is largest and directed inwards while the C_u and C_p terms are comparably less and also directed inwards.

These dimensionless impurity transport coefficients (C_T, C_u and C_p), combined with the experimental values of a/L_{T_i} and a/L_{u_i} (measured by CX), allow an estimate of the zero flux steady state peaking factor to be made as

$$\frac{a}{L_{n_{He2+}}} = -(C_T \frac{a}{L_{T_i}} + C_u u' + C_p) \tag{6.35}$$

The quasilinear impurity peaking factor is finally obtained by assuming that impurity transport is dominated by modes at $k_y = k_y^{\max}$ where the mixing length diffusivity is maximised. Figure 6.11b illustrates the peaking factor for the L-mode high I_p plasma calculated with $\gamma_E = 0$. The filled triangles represent the points that can be assumed to be zero if flow shear is included. Encouraging agreement with experiment is found in both direction and amplitude of the peaking factor around $k_y\rho_i = 2$. The contribution from each of the different linear components of the flux are shown by the dashed lines. The major contribution to the peaking factor comes

Table 6.2: GKW trace impurity gradients

	$a/L_{n_{He}}$	$a/L_{T_{He}}$	$a/L_{u_{He}}$	Flux Output
He Trace 1	0	0	0	C_p
He Trace 2	1	0	0	$D_{He} - C_p$
He Trace 3	0	1	0	$C_T - C_p$
He Trace 4	0	0	1	$C_u - C_p$

from the ion temperature gradient, with the C_T term essentially determining only the direction. The C_u and C_P terms are also directed inwards but contribute weakly to the overall peaking factor.

Quasilinear estimates of the diffusion and convection coefficients, for the 900 kA L-mode discharge at $\rho = 0.7$, can be made using

$$\Gamma^{\mathrm{QL}}_{He2+} = \Gamma^{\mathrm{GKW}}_{He2+} \frac{\chi_e^{eff}}{\chi_e^{\mathrm{GKW}}} \tag{6.36}$$

where $\chi_e^{\mathrm{GKW}} = Q_e^{\mathrm{GKW}} T_e/(a/L_{T_e})$. The value of χ_e^{eff} is interpolated from figure 5.12a at $\rho = 0.7$ and the value of χ_e^{GKW} is chosen around k_y^{max}. This gives values of D_{He}^{GKW} of the order of $1 - 10$ m^2/s, similar to the experimental diffusivity. Furthermore, a previous study by Casson et al. [31] showed that this quasilinear method of obtaining of the peaking factor gives good agreement with full non-linear gyrokinetic simulations.

There are a number of points that must be considered when comparing these results to ITER helium transport predictions. One major difference is that the sheared toroidal flow will not be sufficient on ITER to stabilise the ITG modes. This also indicates a more subtle difference namely that $C_u \sim 0$. Consider the modes associated with $k_y\rho_i < 1$, as shown in figure 6.11a. The C_p term has the larger impact on the overall peaking factor, while the C_T term is less significant. This result has also been demonstrated in a previous study which provides a polynomial fit for the C_P and C_T terms as a function of ρ expected for ITER (see Angioni equations 8 and 9 [142]).

Although the toroidal shear is not expected to stabilise the ITG modes, it has been shown in an experiment on ASDEX-U that the TEMs may be excited in ITER plasmas by applying strong electron cyclotron heating (ECH) [143]. The findings from ASDEX-U were that, when ECH heating was applied to the central region of the plasma, the convection direction of Si impurities reversed direction from inwards to outwards. This may seem contradictory to the results from this thesis, which suggest that the TEMs are driving an inward pinch, but the results can be explained by considering the dependencies of the two terms that make up C_P; that is the curvature and parallel compression terms. The curvature term is proportional to $\hat{s}$ and is directed inwards for both TEMs and ITG modes, whereas the compression term is proportional to $1/q^2$ and is outwards for TEMs and inwards for ITG modes. In the central region of the plasma $1/q^2 >> \hat{s}$ therefore, when the ECH is used to excite the TEMs, the outward compression term dominates over the inward curvature term. Analysis in this thesis has focused on the region close to the plasma edge, where $\hat{s} > 1/q^2$, and therefore the inwards C_P term only enhances the inwards C_U term. An experimental conclusion regarding the inner core from an ST point of view is not possible, since the impurity transport is dominated by neoclassical physics in this region of the plasma.

6.4 Summary

Neoclassical radial profiles of D^{NC} and v^{NC}, calculated using the NCLASS code, are found in every scenario to be comparable in magnitude to the experimental transport coefficients up to a certain radius. In the L-mode plasmas, this region incorporates the plasma core up to $\rho = 0.5$ at high I_p and $\rho = 0.3$ at low I_p. From the plasma mid-radius to the edge, the experimental diffusivity and absolute magnitude of the inward pinch in the L-mode plasmas is greater than neoclassical predictions. For the H-mode plasma, the anomalous inward pinch near the edge of the plasma decreases to a magnitude comparable with neoclassical predictions suggesting that the turbulence has been suppressed.

A microstability analysis has been performed using the GS2 and GKW codes on $\rho = 0.7$ using the L-mode and H-mode high I_p plasma parameters to determine the dominant modes in L-mode. A quasilinear approach has been adopted where the properties of the dominant modes are used to model the saturated turbulence. Without including flow shear, the growth-rate spectrum from both codes indicate unstable modes in the ITG and TEM wavelength region. There are a number of results that suggest that the toroidal flow shear stabilises the ITG modes. An effective growth-rate calculation that includes the stabilising effects of the toroidal flow shear has been performed using GS2. These results indicate that unstable ITG modes in the region $k_y\rho_i < 1$ are suppressed. The BES diagnostic records n_e fluctuations at the wavelength scale equal to $k_y\rho_i \sim 0.5$ representative of ITG modes. At $\rho = 0.7$, the signal is close to the detection threshold indicating that ITG modes are minimal. The main difference between the growth-rate spectrum of the L- and H- mode plasmas is the stabilisation of modes in the region $1 < k_y\rho_i < 3$ due to the shallow electron density gradient. This would suggest that the modes responsible for the anomalous transport in L-mode are found in this wavelength region associated with TEMs. Gyrokinetic quasilinear calculations of the peaking factor in L-mode agree best with the experimental peaking factor, in the region $k_y\rho_i \sim 2$. This also highlighted that the anomalous L-mode pinch is mainly driven by the thermodiffusion term, with smaller contributions from the rotodiffusion and convective term.

In conclusion, the electron density gradient plays a crucial role in the transport of light impurities in spherical tokamaks; a steep electron density gradient causes an inward pinch of helium directly from neoclassical transport and from turbulence associated with collisionless TEMs. Generally the helium pinch caused by turbulence dominates over the neoclassical pinch in L-mode. To avoid a significant accumulation of helium in the plasma core, it is recommended to keep the electron density gradient low; a condition that is met in the ELMy H-mode plasmas on MAST.

Chapter 7

Conclusions and Future Work

7.1 Thesis Objectives and Review

The work presented in this thesis has focused on characterising the helium and carbon transport in three MAST plasma scenarios: two L-mode plasmas with a current of 900 kA and 600 kA and an H-mode plasma with a current of 900 kA. The plasma temperature and magnetic field have been matched in each scenario in an attempt to create essentially one dimensional scans of the safety factor (from the current scan) and the spatial electron density gradient (from the confinement mode scan). Carbon and helium are both intrinsic impurities, the latter introduced from helium glow discharge cleaning and the former from the carbon wall components. Although plasma pulses in MAST are short (< 0.5 s) compared to most conventional tokamaks (> 10 s), the energy confinement time is of the order of 10 ms allowing sufficient time to measure the evolution of the impurity flux in the plasma following a short (< 30 ms) gas puff of helium or methane. A transport analysis of helium was performed in all three plasmas, while an analysis of the carbon transport was only performed for the L-mode 900 kA plasma. For the 600 kA and H-mode plasmas, the perturbation to the intrinsic carbon density profile from the methane gas puff was not sufficient to allow a transport analysis. An impurity charge scan was therefore carried out during the 900 kA L-mode plasma.

An elaborated collisional-radiative model, implemented within the ADAS framework, was used in the analysis to determine the fractional abundances of the impurities across the temperature gradient. Helium and carbon are both fully ionised over the majority of the plasma radius, except for the cold plasma edge region where lower ionisation stages may exist. Excited He^{+} and C^{5+} ions are formed along the neutral beam injection path following active charge exchange between the hydrogen beam atoms and the He^{2+} and C^{6+} ions. The spectral line radiance from these excited ions was measured by the RGB diagnostic, which was built, calibrated and installed on the MAST vessel prior to the start of this work.

RGB Diagnostic

RGB has the ability to measure simultaneously six pre-selected spectral bandpasses in the visible. Incident emission from all wavelengths passes through a single iris. Image splitting and spectral filtering using several interference filters occurs in the telecentric region of the optics. The filtered emission along each channel is collected using two identical camera chips with 640x480 pixel resolution and frame rates of up to 210 Hz. The pixels are coloured to allow the emission to be separated into red, green and blue channels. The selected emissions are beam D_α emission, non-beam D_α emission, two Bremsstrahlung emissions and the He II ($n = 4 \rightarrow 3$) and C VI ($n = 8 \rightarrow 7$) spectral lines at $\lambda = 468.5$ nm $\lambda = 529.1$ nm respectively induced by active charge exchange with the neutral beam atoms. The transport analysis focuses on the latter two measurements of helium and carbon.

Impurity Density Model

Three pieces of information were required to convert the 2D pixel frames of emission measured by RGB into radial profiles of the He^{2+} and C^{6+} density: an estimate of the passive emission contributing the total emission measured within the beam volume, the charge exchange effective emission coefficients and the line-of-sight integrated neutral beam density. The emission from a narrow horizontal range of pixels above and below the beam volume was averaged (top and bottom) along each pixel column and used to estimate the passive charge exchange emission. Each pixel was mapped to R and Z, with respect to the beam line, to determine the experimental background plasma parameters in the centre of the beam volume for each line-of-sight. These plasma parameters were used to interpolate values from the ADAS data set containing the charge exchange effective emission coefficients. The line-integrated neutral beam density was determined using a model, designed specifically for the work in this thesis, which combined the attenuation from the beam divergence and the atomic ionisation processes occurring between the neutral beam atoms and the plasma particles.

The neutral beam model was benchmarked by producing a forward model of the neutral beam emission measured by RGB. Good agreement between the model and experiment was found for the shape of the beam emission profile, however the experimental measurements were dimmer than the model by ~ 40 %. The cause of this discrepancy is currently unknown and is the subject of further work. However this was not an immediate issue for the impurity transport analysis, which relied primarily on the impurity density shape rather than the absolute concentration. The concentrations are more important when deducing the effective charge of the plasma, which was used as input to the theoretical transport models. Using the most recent calibrations of RGB, the helium and carbon concentrations in MAST were ~ 5 % and ~ 0.5 % respectively. This agreed broadly with the effective charge inferred from the Bremsstrahlung measurements from the ZEBRA diagnostic.

Emission induced by excited plume ions and thermal charge exchange between the impurity ions and the beam halo atoms may cause an over-estimation in magnitude of the impurity density profiles; these contributions are not taken into account using only the passive charge exchange subtraction technique. A basic model of these two processes suggested that the beam halo contribution could increase the helium and carbon signal by ~ 5 % and ~ 20 % respectively, while plume emission in the diagnostic sight-lines viewing the plasma core could be similar in magnitude to the active charge exchange signal. Impurity density profiles were only considered outside the range in which plume emission was significant, which is $\rho > 0.2$.

Transport Models

A predictive and an interpretative method was used to determine the diffusion and convection coefficients for both impurities. The predictive technique used the 1.5D SANCO transport code to solve the particle continuity equation with a given set of boundary conditions and a parametrised radial diffusion and convection profile. SANCO was combined with ADAS to allow deduction of the atomic source terms (ionisation, recombination and charge exchange) in the continuity equation. The modelled and experimental impurity density evolutions were matched by setting the diffusion and convection coefficients as free parameters in the least squares fitting algorithm implemented in the UTC code. The interpretative approach extracted the D_i and v_i coefficients from a linear fit to the temporal evolution of the measured impurity flux as a function of the impurity density gradient. This model is insensitive to the impurity influx into the plasma but breaks down in regions of non-negligible atomic source rates. SANCO and UTC have been used in previous studies, but a new a code was designed for this thesis to implement the interpretative method, called the Flux Gradient method, which required benchmarking. This was done by determining the diffusion and convections coefficients from a helium density profile modelled by SANCO. The diffusion and convection coefficients deduced using the Flux Gradient method matched the values used by SANCO in the region $\rho < 0.7$ for helium and $\rho < 0.6$ for carbon; towards the plasma edge the source terms become significant.

For each plasma scenario, an analysis of the neoclassical transport coefficients was carried out using the NCLASS code, while two local flux-tube electromagnetic gyrokinetic codes, GS2 and GKW, were used to simulate the linear growth rate spectrum of the turbulent modes at $\rho = 0.7$ for the L-mode and H-mode plasmas at 900 kA. A summary of the experimental and theoretical findings is given in the next section.

7.2 Results Summary

A general feature of all three plasma scenarios was a region in the plasma core where the convection was mostly insignificant while the diffusivity was $\sim 0.5 - 1$ m^2/s. From $0.4 < \rho < 0.8$, both impurities experienced an inward convection of $5 - 30$ m/s and a diffusivity of $1 - 5$ m^2/s. The results suggest that this outer region of plasma is most susceptible to the impurity charge and confinement mode scan: the diffusion and convection coefficients increased with impurity charge and decreased in H-mode compared to L-mode. There was also evidence from the intrinsic impurity profiles that an outward convection occurs in the inner core of the H-mode plasmas. The current scan found little difference in transport near the plasma edge, however lowering the plasma current produced a higher diffusion and inward convection at mid-radius. These trends are in broad agreement with the findings of impurity transport studies carried out on NSTX and C-Mod.

In previous helium transport studies on conventional tokamaks, the ratio of the helium diffusivity and the effective total heat diffusivity, denoted by η, was often examined to indicate whether a certain plasma scenario would be viable for plasma producing helium from fusion burn. Profiles of the effective heat diffusivity were inferred from the total power balance of the plasma calculated by the predictive JETTO code. The results suggested that $\eta \sim 0.1 - 0.3$, and is due to the anomalous heat diffusivity driven by the electrons. The helium and effective ion heat diffusivity were similar in magnitude. For the plasma current and confinement scans, a similar trend in helium diffusivity was found compared to the effective total heat diffusivity, however the opposite trend in helium diffusivity compared to the effective ion heat diffusivity was found during the confinement scan.

Neoclassical Analysis

Over the plasma radius, the He^{2+} ions are mainly in the Banana collisionality regime, while the C^{6+} ions span the Banana, Plateau and Pfirsch-Schlüter collisionality regimes. The neoclassical simulations did not reproduce the impurity charge and confinement mode trends, but did show the moderate increase in diffusion and convection found at low current. The experimental diffusivity and convection in each scenario were similar in magnitude to the neoclassical predictions up to a certain radius. In the L-mode plasmas, the transport was anomalous in the range $0.5 < \rho \leq 0.8$ and $0.3 < \rho \leq 0.8$ for the 900 kA and 600 kA plasmas respectively. For the H-mode plasma, the magnitude of the inward pinch near the plasma edge was similar to the neoclassical predictions suggesting that the turbulence had been suppressed. The outward flux of impurities observed at mid-radius is a neoclassical effect caused by the region of positive main ion density gradient.

Gyrokinetic Analysis

Linear gyrokinetic simulations of the L-mode plasma at $\rho = 0.7$ showed unstable modes across the wavenumber spectrum when flow shear was not taken into account. A similar growth rate spectrum was observed in the H-mode plasma, however modes in the trapped electron mode (TEM) region in H-mode were stable, presumably because the electron density gradient is lower in H-mode. Including flow shear in the simulations stabilised the ion temperature gradient (ITG) modes in both the L-mode and H-mode plasmas. The (ion scale) density fluctuations measured by the BES diagnostic at $\rho = 0.7$ were close to the detection threshold, which agreed with the theoretical conclusion that the ITG modes were stabilised. It was noted that the BES signal increased nearer the plasma edge indicating unstable ITG modes, which was probably due to the lower flow shearing rate near the edge. Considering that short wavelength electron temperature gradient modes are unlikely to affect the impurity flux, the simulations therefore suggested that TEMs were responsible for the anomalous transport. A quasilinear estimate of the (dimensionless) helium peaking factor calculated by GKW agreed in both magnitude and in direction in the TEM region. The main contribution to the magnitude and direction of the peaking factor came from the ion temperature gradient and the thermodiffusion coefficient respectively, with smaller contributions from the rotodiffusion, parallel compression and curvature terms.

In summary, the electron density gradient plays a crucial role in the transport of light impurities in spherical tokamaks; a steep electron density gradient causes an inward pinch of helium and carbon from the turbulence associated with collisionless TEMs in L-mode.

7.3 Further Research

Gas Puff Timing

The timing of the gas puff was tailored during the experiments to maximise the contrast between the injected and intrinsic impurity density without significantly disturbing the background plasma. Durations of 24 ms and 14 ms were used for helium and 34 ms and 24 ms for methane however, in hindsight, a 30 ms helium gas puff is recommended for all plasmas. An alternative method of injection is probably needed to introduce carbon more effectively into the 600 kA and H-mode plasmas. Reference plasmas (with no gas puff) should be carried out immediately before the gas puff plasmas to obtain a better measurement of the intrinsic impurity profiles.

Expand the MAST Impurity Transport Database

With more machine time, the impurity transport would also have been studied during a collisionality scan and with nitrogen impurity. An initial design of the plasmas

required for the collisionality scan has been made but needs further tailoring to allow for a transport analysis. Nitrogen is adjacent in charge to carbon and therefore fully ionised over the majority of the plasma, however it is an extrinsic impurity and so the gas puff would not have to compete with an intrinsic concentration. Nitrogen was injected into the 900 kA L-mode and H-mode plasmas and measured using 10 chords (5 active and 5 passive) attached to a spectrometer. Calibrations of the measured nitrogen active charge emission were not obtained before the end of this work and therefore the results have not been considered in this thesis.

Poloidal Asymmetries

The effect of the toroidal rotation on the poloidal symmetry of impurities has not been mentioned in this thesis. A flux surface average of the impurity density in the presence of a poloidal asymmetry may lead to a different solution of impurity transport coefficients and therefore requires attention in future work. Charge exchange spectroscopy cannot be used to study the inboard-outboard distribution of impurities because the active charge exchange emission is weaker than the passive emission on the inboard side of the plasma due to the exponential decay of the hydrogen beam atoms. Inversion codes were designed during this work to study the emission measured from the tangential soft x-ray (SXR) camera. There was little evidence from this study to suggest any significant poloidal asymmetries. However the results were inconclusive because of inaccuracies in the relative chord-chord calibrations. This is probably because the SXR diagnostic was not shuttered during boronisation causing an uneven deposition of particles on the camera sensors. The SXR camera port window on MAST-U will be shuttered to protect the camera sensors, which may allow for a better description of the poloidal distribution of impurities in the future.

Publications

- S.S. Henderson, L. Garzotti, F.J. Casson, D. Dickinson, M.F.J. Fox, M. O'Mullane, A. Patel, C.M. Roach, H.P. Summers and M. Valovič, *Neoclassical and gyrokinetic analysis of time-dependent helium transport experiments on MAST*, Nuclear Fusion 54, 093013 (2014)

- S.S. Henderson, L. Garzotti, F.J. Casson, D. Dickinson, M. O'Mullane, A. Patel, C.M. Roach, H.P. Summers and M. Valovič, *Low-Z perturbative impurity transport and microstability analysis on MAST*, 40th EPS Conference on Plasma Physics (Espoo, Finland), P4.146 (2013)

- S.S. Henderson, L. Garzotti, H. Meyer, M. O'Mullane, A. Patel, H.P. Summers and M. Valovič, *Low-Z Impurity Transport Analysis by Transient Gas Puff Experiments*, 54th Annual Meeting of the APS Division of Plasma Physics (Providence, Rhode Island), **57**, 12, GO6.00005 (2012)

Bibliography

[1] J. Wesson, *Tokamaks*, 2nd ed. (Clarendon Press, Oxford, 1997).

[2] M. Edwards *et al.*, Phys. Plasmas **20**, 070501 (2013).

[3] J. Geiger *et al.*, Plasma Phys. Control. Fusion **55**, 014006 (2013).

[4] V. Shafranov and E. Yurchenko, Proc. 4th IAEA Int. Conf. on Plasma Phys. Control. Fusion (Madison, Vienna) **2**, 519 (1971).

[5] C. Smith and S. Cowley, Phil. Trans. R. Soc. **368**, 1091 (2010).

[6] M. Peng and D. Strickler, Nucl. Fusion **26**, 769 (1986).

[7] A. Sykes *et al.*, Proc. 11th Eur. Conf. on Control. Fusion and Plasma Physics (Aachen, W.Germany) 363 (1983).

[8] F. Troyon *et al.*, Plasma Phys. Control. Fusion **26**, 209 (1984).

[9] V. Gusev, F. Alladio, and A. Morris, Plasma Phys. Control. Fusion **45**, A59 (2003).

[10] G. Rewoldt, W. Tang, S. Kaye, and J. Menard, Phys. Plasmas **3**, 1667 (1996).

[11] M. Kotschenreuther *et al.*, Nucl. Fusion **40**, 677 (2000).

[12] C. Roach *et al.*, Plasma Phys. Control. Fusion **47**, B323 (2005).

[13] C. Bourdelle *et al.*, Phys. Plasmas **10**, 2881 (2003).

[14] A. Sykes *et al.*, Nucl. Fusion **32**, 694 (1992).

[15] M. Gryaznevich *et al.*, Phys. Rev. Lett. **80**, 3972 (1998).

[16] M. Ono *et al.*, Nucl. Fusion **40**, 557 (2000).

[17] S. Kaye *et al.*, Phys. Plasmas **8**, 1977 (2001).

[18] M. Cox, Fusion Eng. Des **46**, 397 (1999).

[19] A. Morris, IEEE Trans. Plasma Sci. **40**, 682 (2012).

[20] D. Reiter, G. Wolf, and H. Kever, Nucl. Fusion **30**, 2141 (1990).

[21] T. Loarer *et al.*, Nucl. Fusion **47**, 1112 (2007).

[22] R. Pitts *et al.*, J. Nucl. Mater. **438**, S48 (2013).

[23] M. Von Hellermann *et al.*, Phys. Scripta **T120**, 19 (2005).

[24] A. Patel *et al.*, Rev. Sci. Instrum. **75**, 4145 (2004).

[25] A. Patel, N. Conway, and P. Carolan, in preparation for Rev. Sci. Instrum. (2014).

[26] H. Summers, The ADAS User Manual **V2.6**, www.adas.ac.uk (2004).

[27] F. Hinton and R. Hazeltine, Rev. Mod. Phys. **48**, 239 (1976).

[28] C. Angioni and A. Peeters, Phys. Rev. Lett. **96**, 1 (2006).

[29] C. Angioni *et al.*, Nucl. Fusion **49**, 055013 (2009).

[30] N. Howard *et al.*, Phys. Plasmas **19**, 056110 (2012).

[31] F. Casson *et al.*, Nucl. Fusion **53**, 063026 (2013).

[32] X. Garbet *et al.*, Plasma Phys. Control. Fusion **46**, B557 (2004).

[33] R. Dux, Habilitationsschrift IPP **10**, 27 (2004).

[34] R. Guirlet *et al.*, Plasma Phys. Control. Fusion **48**, B63 (2006).

[35] W. Houlberg, K. Shaing, S. Hirshman, and M. Zarnstorff, Phys. Plasmas **4**, 3230 (1997).

[36] M. Kotschenreuther, G. Rewoldt, and W. Tang, Comput. Phys. Commun. **88**, 128 (1995).

[37] W. Dorland, F. Jenko, M. Kotschenreuther, and B. Rogers, Phys. Rev. Lett **85**, 5579 (2000).

[38] A. Peeters *et al.*, Comput. Phys. Commun. **180**, 2650 (2009).

[39] L. Delgado-Aparicio *et al.*, Nucl. Fusion **49**, 085028 (2009).

[40] F. Scotti *et al.*, Nucl. Fusion **53**, 083001 (2013).

[41] D. Stutman *et al.*, Phys. Plasmas **10**, 4387 (2003).

[42] A. Foster, G. Counsell, and H. Summers, J. Nucl. Mater. **363-365**, 152 (2007).

[43] J. McCone *et al.*, Proceedings of the 37th EPS Conference on Plasma Physics **34A**, 1061 (2010).

[44] E. Marmar, Fusion Sci. Technol. **51**, 261 (2007).

[45] G. Duesing *et al.*, Fusion Technol. **11**, 163 (1987).

[46] S. Gee *et al.*, Fusion Eng. Des. **74**, 403 (2005).

[47] I. Brown, *The Physics and Technology of Ion Sources*, 2nd ed. (John Wiley and Sons, Germany, 2006).

[48] D. Godden, Ph.D. thesis, Dublin City University, 2000.

[49] H. Falter, D. Ciric, S. Cox, and D. Godden, JET-R **10**, (1998).

[50] B. Crowley *et al.*, EFDA-JET-CP(02) **05/16**, .

[51] E. Surrey *et al.*, EFDA-JET-PR(04) **51**, .

[52] A. Patel, P. Carolan, N. Conway, and R. Akers, Rev. Sci. Instrum. **75**, 4944 (2004).

[53] H. Meyer *et al.*, J. Phys. Conf. Ser. **123**, 012005 (2008).

[54] R. Pitts *et al.*, Nucl. Fusion **47**, B303 (2005).

[55] G. Federici *et al.*, Nucl. Fusion **41**, 1967 (2001).

[56] A. Darke, R. Hayward, G. Counsell, and K. Hawkins, Fusion Eng. Des. **75-79**, 285 (2005).

[57] M. Wade *et al.*, Phys. Plasmas **2**, 2357 (1995).

[58] C. Giroud *et al.*, Nucl. Fusion **47**, 313 (2007).

[59] I. Lehane *et al.*, Annual Meeting of the APS Division of Plasma Physics **43**, RP1.056 (2001).

[60] R. Fonck, A. Ramsey, and R. Yelle, Appl. Opt **12**, 2115 (1982).

[61] A. Thornton *et al.*, Plasma Phys. Control. Fusion **54**, 125007 (2012).

[62] G. Pautasso *et al.*, Plasma Phys. Control. Fusion **51**, 124056 (2009).

[63] I. Hutchinson, *Principles of Plasma Diagnostics*, 2nd ed. (Cambridge University Press, Cambridge, 2002).

[64] A. Selden, Phys. Lett. A **79**, 405 (1980).

[65] O. Naito, H. Yoshida, and M. T, Phys. Fluids B **5**, 4256 (1993).

[66] M. Walsh *et al.*, Rev. Sci. Instrum. **74**, 1663 (2003).

[67] R. Scannell *et al.*, Rev. Sci. Instrum. **79**, 10E730 (2008).

[68] N. Conway *et al.*, Rev. Sci. Instrum. **77**, 10F131 (2006).

[69] W. Finkelnburg and T. Peters, Handbüch der Physik **28**, 79 (1957).

[70] A. Burgess and H. Summers, Mon. Not. R. Astron. Soc **226**, 257 (1987).

[71] D. Dunai, S. Zoletnik, J. Sárközi., and A. R. Field, Rev. Sci. Instrum **81**, 103503 (2010).

[72] Y.-C. Ghim, A. R. Field, S. Zoletnik, and D. Dunai, Rev. Sci. Instrum. **81**, 10D713 (2010).

[73] L. Lao *et al.*, Nucl. Fusion **25**, 1611 (1985).

[74] L. Appel *et al.*, 33rd EPS Conference on Plasma Physics **01**, (2006).

[75] N. Conway *et al.*, Rev. Sci. Instrum. **81**, 10D738 (2010).

[76] J. Storrs, J. Dowling, G. Counsell, and G. McArdle, Fusion Eng. Des. **81**, 1841 (2006).

[77] R. Miller *et al.*, Phys. Plasmas **5**, 973 (1998).

[78] D. Bates, A. Kingston, and R. McWhirter, Proc. R. Soc. A. **267**, 297 (1962).

[79] H. Summers *et al.*, Plasma Phys. Control. Fusion **48**, 263 (2006).

[80] H. Summers, Mon. Non. R. astr. Soc. **178**, 101 (1977).

[81] L. Lauro-Taroni *et al.*, EPS Conference on Controlled Fusion and Plasma Physics **21**, 102 (1994).

[82] J. Spence and H. Summers, J. Phys. B: At. Mol. Phys. **19**, 3749 (1986).

[83] R. Fonck, D. Darrow, and K. Jaehnig, Phys. Rev. A **29**, 3288 (1984).

[84] R. Bell, Rev. Sci. Instrum. **77**, 10E902 (2006).

[85] H. Anderson *et al.*, Plasma Phys. Control. Fusion **42**, 781 (2000).

[86] E. Synakowski *et al.*, Phys. Rev. Lett. **65**, 2255 (1990).

[87] E. Synakowski *et al.*, Phys. Fluids B **5**, 2215 (1993).

[88] ITER Physics Basis: Nucl. Fusion **39**, 2175 (1999).

[89] M. Valovič *et al.*, Nucl. Fusion **49**, 075016 (2009).

[90] M. Valovič *et al.*, Nucl. Fusion **45**, 942 (2005).

[91] M. Valovič *et al.*, Nucl. Fusion **51**, 073045 (2011).

[92] A. Kirk *et al.*, Plasma Phys. Control. Fusion **47**, 315 (2005).

[93] I. Chapman *et al.*, Nucl. Fusion **50**, 045007 (2010).

[94] W. Heidbrink and G. Sager, Nucl. Fusion **30**, 1015 (1990).

[95] T. O'Gorman *et al.*, 39th EPS Conference on Plasma Physics 2012 **3**, 1710 (2012).

[96] J. Snape, K. Gibson, T. O'Gorman, and N. Barratt, Plasma Phys. Control. Fusion **54**, 085001 (2012).

[97] M. Tournianski, Ph.D. thesis, The University of Essex, 1999.

[98] P. Stubberfield and M. Watkins, JET-DPA **06**, (1987).

[99] Y. Feng, B. Wolle, and K. Hubner, Comp. Phys. Commun. **88**, 161 (1995).

[100] M. Schneider, L. Eriksson, and I. Jenkins, Nucl. Fusion **51**, 063019 (2011).

[101] E. Delabie *et al.*, Plasma Phys. Control. Fusion **52**, 125008 (2010).

[102] J. McCone, Ph.D. thesis, University College Cork, 2011.

[103] A. Whiteford, Ph.D. thesis, University of Strathclyde, 2004.

[104] S. Tamor, J. Comput. Phys. **40**, 104 (1981).

[105] E. Synakowski *et al.*, Phys. Rev. Lett. **75**, 3689 (1995).

[106] K.-D. Zastrow *et al.*, Nucl. Fusion **45**, 163 (2005).

[107] D. Reiter *et al.*, Plasma Phys. Control. Fusion **33**, 1579 (1991).

[108] L. Garzotti *et al.*, Nucl. Fusion **46**, 994 (2006).

[109] G. Cenacchi and A. Taroni, Report JET-IR **88**, 03 (1988).

[110] G. Cenacchi and A. Taroni, Rapporto ENEA RT/TIB **88**, 5 (1988).

[111] A. Field *et al.*, Proc. 20th IAEA Fusion Energy Conf. **EX/P2-11**, (Vilamoura, Portugal (2004).

[112] S. Kaye *et al.*, Nucl. Fusion **47**, 499 (2007).

[113] C. Roach *et al.*, Plasma Phys. Control. Fusion **51**, 124020 (2009).

[114] M. Valovič *et al.*, Plasma Phys. Control. Fusion **44**, 1911 (2002).

[115] S. Braginskii, *Reviews of plasma physics*, m.a. leontovich ed. (Consultants Bureau, New York., 1965), Vol. 1, p. 205.

[116] P. Helander and D. Sigmar, *Collisional Transport in Magnetized Plasmas*, 1st ed. (Cambridge University Press, Cambridge, 2002).

[117] J. Connor and H. Wilson, Plasma Phys. Control. Fusion **36**, 719 (1994).

[118] S. Hirshman and D. Sigmar, Nucl. Fusion **21**, 1079 (1981).

[119] G. Fussman *et al.*, Plasma Phys. Control. Fusion **33**, 1677 (1991).

[120] C. Chang and S. Kaye, Phys. Fluids B **3**, 395 (1991).

[121] L. Delgado-Aparicio *et al.*, Nucl. Fusion **51**, 083047 (2011).

[122] W. Tang, Nucl. Fusion **18**, 1089 (1978).

[123] W. Horton, *Turbulent Transport in Magnetised Plasmas*, 1st ed. (World Scientific Publishing Co. Pte. Ltd., Singapore, 2012).

[124] C. Horton and R. Varma, Phys. Fluids **15**, 620 (1972).

[125] J. Connor, Nucl. Fusion **26**, 193 (1986).

[126] T. Dannert and F. Jenko, Phys. Plasmas **12**, 072309 (2005).

[127] M. Romanelli, C. Bourdelle, and W. Dorland, Phys. Plasmas **11**, 3845 (2004).

[128] M. Romanelli, G. Regnoli, and C. Bourdelle, Phys. Plasmas **14**, 082305 (2007).

[129] D. Applegate *et al.*, Phys. Plasmas **11**, 5085 (2004).

[130] R. Budny, M. Bell, and H. Biglari, Nucl. Fusion **429**, 32 (1992).

[131] R. Waltz, G. Kerbel, and J. Milovich, Phys. Plasmas **2229**, 1 (1994).

[132] Y. Camenen *et al.*, Phys. Plasmas **16**, 012503 (2009).

[133] F. Casson *et al.*, Phys. Plasmas **17**, 102305 (2010).

[134] A. Peeters, C. Angioni, and D. Strintzi, Phys. Rev. Lett. **98**, 265003 (2007).

[135] A. Peeters, D. Strintzi, C. Angioni, and a. et, Phys. Plasmas **16**, 042310 (2009).

[136] F. Casson, Ph.D. thesis, University of Warwick, 2011.

[137] A. Brizard, Phys. Plasmas **2**, 459 (1995).

[138] L. Garzotti *et al.*, Plasma Phys. Control. Fusion **56**, 035004 (2014).

[139] J. Weiland, A. Jarmen, and H. Nordman, Nucl. Fusion **29**, 1810 (1989).

[140] B. Coppi and C. Spight, Phys. Rev. Lett. **41**, 551 (1978).

[141] X. Garbet *et al.*, Phys. Rev. Lett. **91**, 035001 (2003).

[142] C. Angioni *et al.*, Nucl. Fusion **52**, 114003 (2012).

[143] C. Angioni, R. Dux, E. Fable, and A. Peeters, Plasma Phys. Control. Fusion **49**, 2027 (2007).